Remote Powering of Wireless IoT Nodes

John Nicot

université de BORDEAUX

THÈSE PRÉSENTÉE

POUR OBTENIR LE GRADE DE

DOCTEUR DE

L'UNIVERSITÉ DE BORDEAUX

ÉCOLE DOCTORALE DES SCIENCES PHYSIQUES ET DE L'INGENIEUR (SPI)

SPÉCIALITÉ : ÉLECTRONIQUE

John NICOT

REMOTE POWERING OF WIRELESS IOT NODES

Sous la direction de : Prof. Thierry TARIS
(co-encadrante : Dr. Ludivine TARIS-FADEL)

Soutenue le 4 Mars 2021

Membres du jury :

M. JEGO, Christophe	Professeur, Bordeaux INP	Examinateur (Président)
M. FRICK, Vincent	Professeur Associé, Université de Strasbourg	Rapporteur
M. MIRABBASI, Shahriar	Professeur, University of British Columbia	Rapporteur
M. MENEKEN, Jan	Ingénieur, Uwinloc, Toulouse	Examinateur
Mme. TARIS-FADEL, Ludivine	Professeur Associé, Université de Bordeaux	Examinateur (Co-encadrante)
M. TARIS, Thierry	Professeur, Bordeaux INP	Examinateur (Directeur de Thèse)

This page intentionally left blank.

Alimentation de Nœuds sans fils IoT

Résumé

Le monde connaît un intérêt croissant pour l'IoT (Internet des Objets) et de l'écosystème qui y est rattaché. Afin de minimiser l'impact environnemental et les coûts de maintenance rattachés à ces nœuds, il est nécessaire de les alimenter en excluant l'usage de piles et des batteries, pour des coûts environnementaux et de maintenance. Cette thèse a pour vocation d'étudier la faisabilité architecturale de tels nœuds et leur robustesse, afin d'en tirer des conclusions sur d'éventuelles techniques et méthodes d'implémentation qui seront nécessaires à leur mise en œuvre dans le monde réel. Elle étudiera aussi leurs limitations ou des optimisations pour des situations particulières (différents débits de données, type de données à capter, fréquence d'émission...).

Mots clés

IoT; Récupération d'Energie; Rectifiers; Réseaux de Capteurs Sans-fil.

Remote Powering of Wireless IoT Nodes

Abstract

The world is becoming increasingly interested in the IoT (Internet of Things) and the associated ecosystem. In order to minimize the environmental impact and the maintenance costs associated with such nodes, it is necessary to minimize the use of batteries for both environmental and maintenance costs. This thesis aims to study the architectural feasibility of such nodes and their robustness, in order to draw conclusions about techniques and implementation methods that will be necessary for real-world applications. It will also study their limits or possible optimizations for certain situations (data rate, types of data to be captured, frequency of transmission, etc.).

Keywords

IoT; Power Harvesting; Rectifiers; Wireless Sensor Networks.

This page intentionally left blank.

Laboratoire de l’Intégration, du Matériau au Système (IMS)

UMR 5218

Bâtiment A31, 351 Cours de la Libération, F-33405 TALENCE CEDEX

This page intentionally left blank.

Acknowledgements

The writing of this dissertation, and the work done for it herein, would not have been possible without a great deal of support and dialogue.

First, I would like to thank my thesis director, Prof. Thierry TARIS. Without your never-ending patience, guidance and assistance, my thesis would have not been possible.

I would also like to thank my colleagues, both at the IMS Laboratory and the ENSEIRB-MATMECA engineering school, who have been a pillar of support and provided me with invaluable insight with my work.

Finally, let me express my gratitude to my parents, my brother, my extended family (French and American), and countless other people who have given me great emotional support, endless amounts of encouragement, and managed to keep me on track during my thesis.

Dedicated to my grandfather, the late Roger NICOT (1926 – 2020).

This page intentionally left blank.

Table of Contents

Table of Figures

Table of Tables

This page intentionally left blank.

Glossary

2G	2nd Generation GSM
3G	3rd Generation GSM
4G	4th Generation GSM
AC	Alternative Current
ADC	Analog to Digital Converter
AES	Advanced Encryption Standard
ANFR	Agence Nationale des Fréquences
ARCEP	Autorité de Régulation des Communications Electroniques et des Postes
ASIC	Application-Specific Integrated Circuit
ASK	Amplitude Shift Keying
CMOS	Complementary Metal Oxide Semiconductor
COTS	Component Off The Shelf
CRC	Cyclic Redundancy Check
CS	Cold-Start
CSMA	Carrier Sense Multiple Access
CW	Continuous Wave
DC	Direct Current
DUT	Device Under Test
DTV	Digital Television
EM	ElectroMagnetic
ESR	Equivalent Series Resistance
FCC	Federal Communications Commission
FRAM	Ferroelectric RAM
FS	Full-Start
FSK	Frequency Shift Keying
GFSK	Gaussian Frequency Shift Keying
GSM	Global System for Mobile Communication
GUI	Graphical User Interface
I2C	Inter-Integrated Circuit
IC	Integrated Circuit
IoT	Internet of Things
ISM	Industrial, Scientific and Medical
LED	Light Emitting Diode
LF	Low Frequency
MPPT	Maximum Power Point Tracking
NFC	Near-Field Contact
OOK	On-Off Keying
PCB	Printed Circuit Board
PLL	Phased Locked Loop
PMU	Power Management Unit
RF	Radio Frequency
RFID	Radio Frequency IDentification
RX	Reception
SDR	Software Defined Radio
SPI	Serial Peripheral Interface
SPICE	Simulation Program with Integrated Circuit Emphasis
TX	Transmission
VCO	Voltage Controlled Oscillator
UHF	Ultra-High Frequency band
VLSI	Very Large Scale Integration
WPH	Wireless Power Harvesting
WPN	Wirelessly Powered Nodes
WPT	Wireless Power Transfer/Transmission
WS	Warm-Start
WSN	Wireless Sensor Node
µC	Microcontroller

This page intentionally left blank.

General Introduction

There has been tremendous growth in the demand for applications requiring large scale deployment of IoT (Internet of Things) nodes and WPT (Wireless Power Transfer). With this in mind, in order to satisfy the required demand, the need for low power, long life, low maintenance and inexpensive WSNs (Wireless Sensor Nodes) has become a key factor in order to make the IoT possible. This thesis has been organized as follows:

Chapter I will give an overview of power harvesting, including a brief history of WPT, the most recent advancements in the field, and solutions currently available on the commercial market today.

Chapter II describes a modular COTS system, composed of interchangeable blocks that were developed during this work, discussing why the architecture for each block was chosen, while detailing the different aspects of each block, and measuring their technical characteristics. Notably, the blocks are as follows:

- Rectifier (for WPT and data reception), operating in the 900 MHz ISM band,
- Comparator (data demodulation and wake-up generation),
- Power Management (for energy management, buck/boost operations for power delivery),
- Power Storage (for storing received energy),
- Data Processing and Intelligence (for interpreting received data and acting on it),
- Data Storage (to store data collected by the node),
- Sensors (for environmental data collection).

Chapter III analyses the assembled system that was developed using the aforementioned blocks in Chapter II, as each of them were optimized. It furthermore analyzes the power consumption of the node as a whole system. It also presents a simulator that can be used to theoretically calculate power consumption and autonomy of the node under various scenarios of operation. Finally, it determines the performance of the assembled systems with

related metrics, in regards to their aptitude of working in several different applicative scenarios.

Chapter IV will provide a synthesis of this work, showing the results that have been achieved by the design of a modular WSN, operating in the 900 MHz ISM band, and compare it against other work in the domain. It will also present several perspectives on future possible work.

Introduction Générale

La demande d'applications nécessitant un déploiement à grande échelle de nœuds IoT (Internet of Things) et de WPT (Wireless Power Transfer) a considérablement augmenté. Dans cet esprit, afin de satisfaire la demande requise, le besoin de WSNs (Wireless Sensor Nodes) à faible consommation d'énergie, d'une longue durée de vie, ayant peu besoin d'entretien, et étant peu coûteux est devenu un facteur clé pour rendre l'IoT possible. Cette thèse a été organisée comme suit :

Le chapitre I donnera un aperçu de la récupération d'énergie, y compris un bref historique du WPT, les progrès les plus récents dans le domaine et les solutions actuellement disponibles sur le marché commercial aujourd'hui.

Le chapitre II décrit un système COTS modulaire, composé de blocs interchangeables qui ont été développés au cours de ce travail, expliquant pourquoi l'architecture de chaque bloc a été choisie, tout en détaillant les différents aspects de chaque bloc et en mesurant leurs caractéristiques techniques. Notamment, les blocs sont les suivants :

- Redresseur (pour WPT et réception de données), fonctionnant dans la bande ISM 900 MHz,
- Comparateur (démodulation des données et génération de réveil),
- Gestion de l'énergie (pour la gestion de l'énergie, les opérations buck/boost pour la fourniture d'énergie),
- Power Storage (pour stocker l'énergie reçue),
- Traitement et renseignement des données (pour interpréter les données reçues et agir sur celles-ci),
- Stockage de données (pour stocker les données collectées par le nœud),
- Capteurs (pour la collecte de données environnementales).

Le chapitre III analyse le système assemblé qui a été développé, en utilisant les blocs susmentionnés au chapitre II, chacun d'eux ayant étés optimisés. Il analyse, en outre, la consommation électrique du nœud dans son ensemble. Il présente également un simulateur qui peut être utilisé pour calculer théoriquement la consommation d'énergie et l'autonomie du

nœud, dans différents scénarios de fonctionnement. Enfin, il détermine les performances des systèmes assemblés avec des métriques associées, en ce qui concerne leur aptitude à travailler dans plusieurs scénarios applicatifs différents.

Le chapitre IV fournira une synthèse de ce travail, montrant les résultats qui ont été obtenus par la conception d'un WSN modulaire, fonctionnant dans la bande ISM 900 MHz, et le comparera à d'autres travaux dans le domaine. Il présentera également plusieurs perspectives sur les travaux futurs possibles.

Chapter I

Introduction to WPT

This page intentionally left blank.

Chapter I Introduction to WPT

Section I.a – What is Wireless Power Transfer?

Wireless Power Transfer (WPT) is becoming an increasingly used technology in modern-day applications. This section presents a brief overview of WPT, as well as a more detailed technical overview of far-field WPT, in order to set up precedents and definitions used in this work. It concludes with a brief overview of other power harvesting energy sources, in order to compare Wireless Power Harvesting (WPH) to other types of ambient energy recuperation.

Subsection I.a.1 – Introduction

The increasing need for more efficiency, increased autonomy, less energy consumption, and more interoperability of all these different systems has created a large demand for systems and devices that require little maintenance, need to be portable, contain a rich feature set and can be manufactured on a large scale. Notably, the ever increasing need to be environmentally conscious has become a major factor in determining the viability of maintaining such systems operable, especially in regards to energy storage, recycling, reuse and longevity.

Energy storage is one of the more pressing aspects in terms of environmental respect, because currently there is no efficient, carbon neutral method that properly stores large amounts of energy. This makes it extremely difficult to efficiently power devices that either need to be portable or be highly efficient.

In addition, significant overheads exist, in terms of cost and resource consumption, for energy and information transported by conventional means, such as by electrical cables. The complexity of the situation is further increased as the current trend for many new systems and technologies is that they are becoming increasingly dense, in terms of the sheer number of devices, and more ubiquitous.

The IoT is a concept which involves using many computing devices in a multitude of different domains, including healthcare, transportation, agriculture, consumer appliances and energy management. The purpose of this is to facilitate automated information exchange, as a method for meeting today's challenges. A brief, non-exhaustive overview of domains the IoT applies itself to is shown in fig. 1:

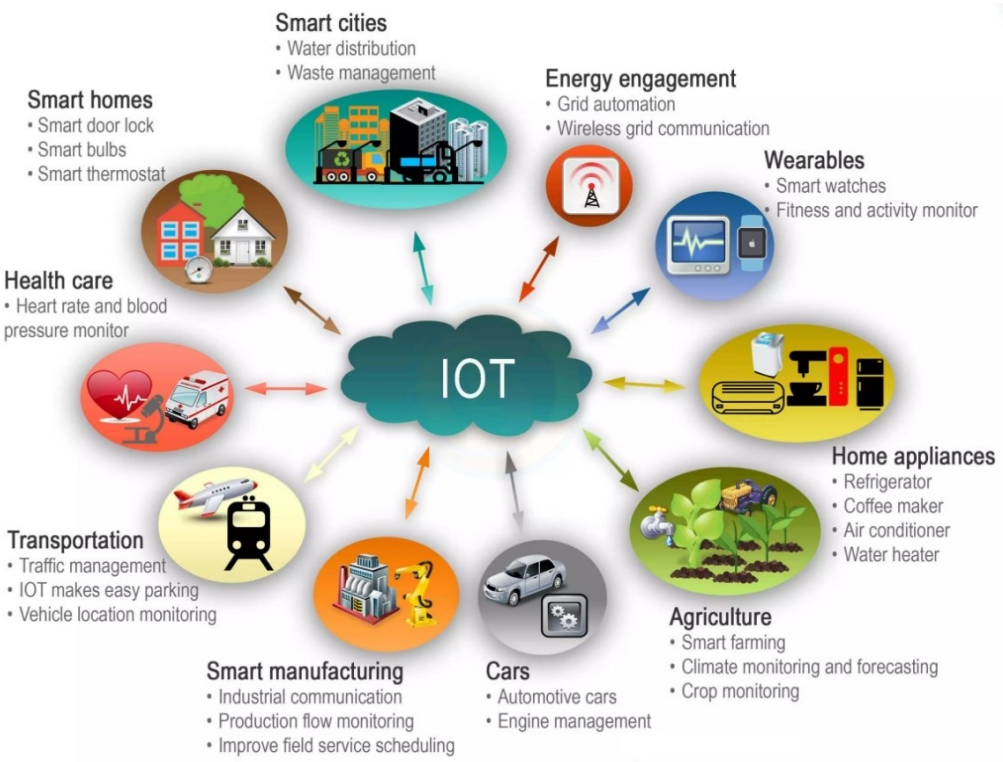

Figure 1 – Domains covered by the IoT [1].

Recent research in technological sustainability of the IoT has led to a large interest in the development of low power, low maintenance, and low environmentally-impacting devices. Therefore, it is of the utmost importance to apply new research and technologies pertaining to the powering and storing of energy for these devices, and to keep them batteryless. One of the more challenging concepts used to power IoT devices is energy harvesting.

Subsection I.a.5 – Energy Harvesting Methods

Several passive energy sources exist that are capable of powering IoT devices. Due to the diversity of these methods, it is interesting to compare the different amounts of energy that different sources can provide, in order to see their aptitude in being able to generate power.

Depending on the amount of energy required by a system, and the cost involved in implementing powering such devices, different power sources may be adapted for different implementations, scenarios or schemes. Analyzing different sources will also permit a comparison of WPH to other sources of energy.

Fig. 2 presents a variety of different energy sources for IoT devices, and their associated harvesting interfaces:

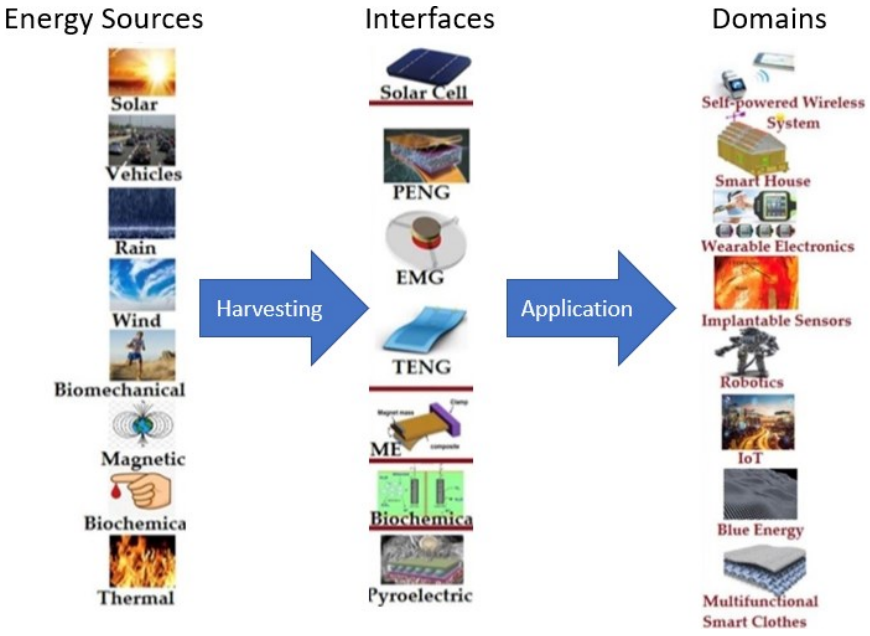

Figure 2 – Different types of harvestable energy sources for low-power IoT nodes, adapted from [2].

Table 1 presents an overview of typical amounts of energy that can be harvested from different types of ambient energy sources:

Energy Type	Cost	Average Power Density	Average Efficiency	Sources
Solar	Medium	0–150 mW/cm^2 (Outside) 0–150 µW/cm^2 (Inside)	20–45% Dependent on cell type	[3]-[4]
Thermoelectric	High	1–3000 µW/cm^2/K^{-1}	1–70% Dependent on ΔT	[3],[5]-[6]
Electromagnetic	Low	10–300 µW	10–40% Dependent on EM field	[3],[7]-[8]
Radiofrequency	Low	50-100 nW/cm^2 – 900 MHz 1-50 nW/cm^2 – 2.4 GHz	5–40% Dependent on P_{IN}, networks	[3],[7],[9]-[12]
Vibrational	Low	4–100 µW/cm^3	1–50% Dependent on environment	[3],[13]-[14]
Acoustic	High	10-30 mW	5–70% Dependent on sound pressure	[3],[12],[15]-[16]
Wind	High	0-200 mW/cm^2	35% - 45% Dependent on wind speed, turbine type	[3],[17]-[18]

Table 1 – Typical power levels from different harvestable sources.

It can be seen that of all the different harvestable types of energy available, generally wind and solar energies provide the most power per unit area. Thermoelectric, electromagnetic and vibrational energy sources also provide interesting energy densities. It should be noted that, for the most part, these technologies for energy harvesting are quite costly to implement, in terms of overhead costs, infrastructure size and maintenance. It should also be noted that certain types of harvesting can be combined together [3], [12], [16], [18].

Harvesting energy from electromagnetic sources, whether low-frequency or radiofrequency, provide lower power densities, but are relatively easy to implement and require little maintenance. However, it should be noted that one of the higher power density energy sources in the radiofrequency band, 2G GSM, will eventually be phased out as mobile networks are upgraded [19].

Wireless energy is used in many different ways, but the two main scenarios of exploitation for it are radio communications (which includes any passive form of communication used to infer data), and Wireless Power Transfer (WPT). Surprisingly, WPT is a relatively old concept by modern technological standards and timeframes, with research in the domain being initiated as early as the late 18th century. However, until very recently, its ubiquity was limited by the lack of scalability, the high cost of implementation, the lack of proper energy storage and management, as well the size of devices. Recent technological trends have made WPT a more accessible technology, which can now be considered in modern day applications.

Subsection I.a.2 – Near-field and far-field

WPT is not a single type of physical phenomena. There are several different physical laws that regulate how energy can be exchanged wirelessly. These can be mainly categorized as energy exchange in the near-field, which primarily includes inductive forms of energy transfer, and far-field energy exchange, which is mainly radiative. These different forms of energy transfer are illustrated in fig. 3 below:

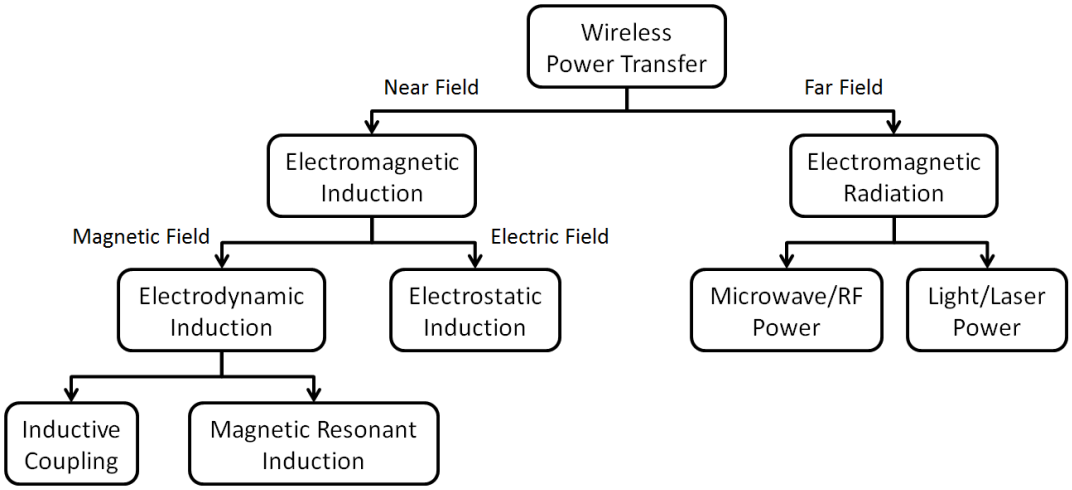

Figure 3 – The different implementations of WPT.

The determination of distance at which wireless power transfer is either near- or far-field is done on the basis of antenna size D, and wavelength λ at which the energy transfer occurs.

The near-field can further be subdivided into two regions: the reactive near-field region, and the radiative, or Fresnel, region. In the reactive region, the electric and magnetic fields are 90° out of phase with each other and therefore defined as reactive. In the Fresnel region, EM fields transition from being reactive to radiative (in phase). Radiation patterns are highly difficult to predict in the near-field.

The far-field region is when the electromagnetic (EM) fields are dominantly radiative, as opposed to reactive. In this region, the electric and magnetic fields are orthogonal to each other, and propagate as waves; possibly polarized, depending on the antenna type they were transmitted from. Figure 4, below, illustrates the subdivisions of these different regions:

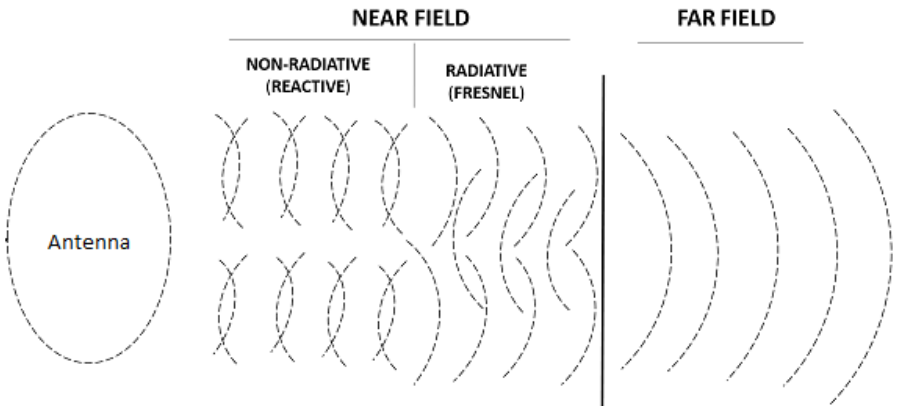

Figure 4 – Iluustraton of near-field and far-field regions [20].

The distances determining the different regions can be summarized as follows:

- When the distance d is smaller than $0.62 \cdot \sqrt[2]{\frac{D^3}{\lambda}}$, the operation of the RF system happens in the reactive near-field.
- When the distance d is situated between $0.62 \cdot \sqrt[2]{\frac{D^3}{\lambda}}$ and $\frac{2D^2}{\lambda}$, the operation of the RF system happens in the Fresnel near-field.
- When the distance d exceeds $\frac{2D^2}{\lambda}$, the operation of the RF system happens in the far-field.

Subsection I.a.3 – Far-field Propagation

Near-field WPT is generally used for applications such as radiofrequency identification (RFID), inductive coupling or near-field communications (NFC). This work studies IoT nodes that are autonomous over a distance of several meters or more, and operating in the ISM band at approximatively 900 MHz. Therefore, far-field propagation will be the method with which wireless energy will be transmitted in this work.

EM waves radiating in the far-field are made of two components: the electrical field $\vec{E}$, and the magnetic field $\vec{H}$. $\vec{E}$ and $\vec{H}$ are orthogonal to each other , and are also orthogonal to the direction of propagation, described by the unity vector $\vec{k}$. If isolated in a region with no external charges or currents, of permeability μ_r and permittivity ε_r, $\vec{E}$ and $\vec{H}$ obey the following equations:

$$\nabla^2 \vec{E} = \mu\varepsilon \frac{\partial^2 \vec{E}}{\partial t^2}$$

$$\nabla^2 \vec{B} = \mu\varepsilon \frac{\partial^2 \vec{B}}{\partial t^2}$$

$$\mu = \mu_r \mu_0, \varepsilon = \varepsilon_r \varepsilon_0$$

Fig. 5 below illustrates far-field propagation for a linearly polarized EM wave:

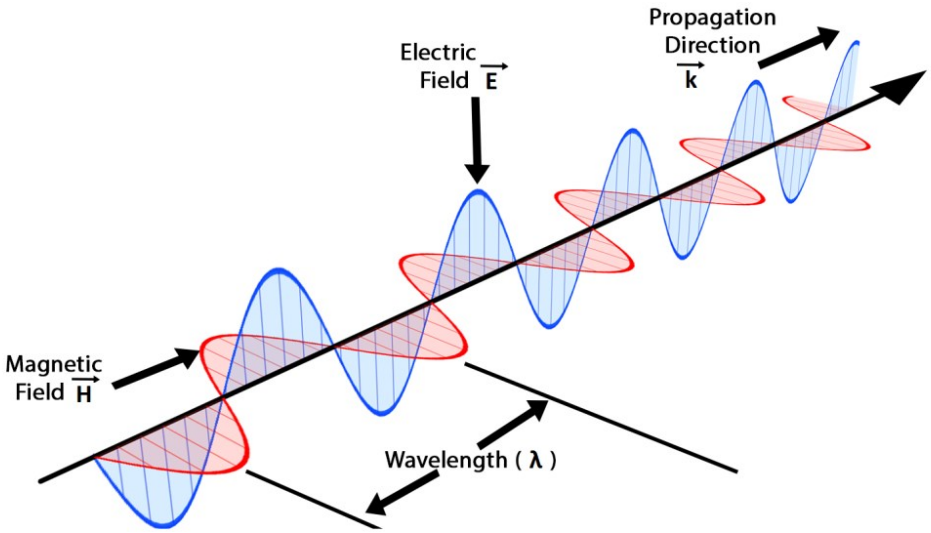

Figure 5 - Propagation of an EM wave [21].

Subsection I.a.4 – Far-field Energy Measurement

Of interest is also the ability to determine and measure the received amount of energy from a source transmitter, as well as associated metrics. Antennae possess many different metrics, however, for the purposes of this work, we will simply select those in regards to their size or how they radiate energy, in terms of power density.

It should be noted that, for a perfectly isotropic antenna, energy is radiated evenly in all directions. Therefore, it should come as no surprise that the average power density P_d, measured as the distance d from the antenna, decreases rapidly. This is because all the power P emitted by the antenna is spread over a surface that will depend on d, as an inverse square law. As it is impossible for any antennae to be perfectly isotropic, most usually have a privileged direction of radiation, to which a gain, G is associated. With this, we are able to define an effective antenna area A_e, defined by the following equation:

$$A_e = \frac{\lambda^2}{4\pi} G$$

Therefore, the power density at a distance d from an antenna can be described by the following equation:

$$P_d = \frac{P \cdot G}{4\pi d^2}$$

Generally, $P \cdot G$ is known as the effective isotropically radiated power (EIRP) of the emitting antenna, for regulatory purposes. Combining these equations with both a reception and transmission antenna, called TX and RX, respectively, makes it possible to derive the Friis transmission formula:

$$P_{RX} = P_{d,RX} A_{e,RX} = P_{TX} G_{TX} G_{RX} \left(\frac{\lambda}{4\pi d}\right)^2$$

This formula is illustrated by figure 6 below:

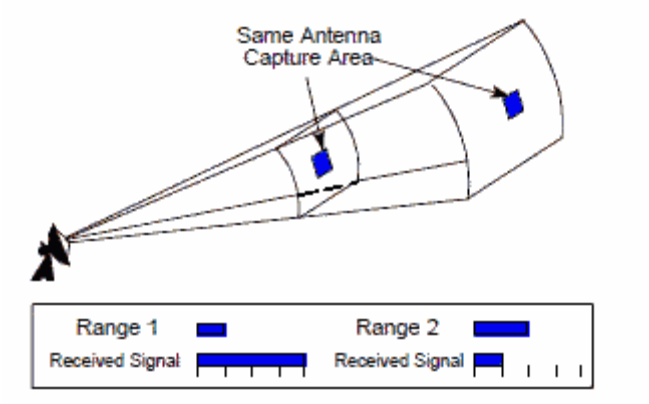

Figure 6 – Decreasing power density for a reception antenna of equal effective area [22].

Additionally, it is possible to derive the free space path loss (FSPL) from the Friis transmission formula, or the amount of energy a freely propagating wave loses over its transmission distance d, defined by the following equation:

$$FSPL = \left(\frac{4\pi d}{\lambda}\right)^2$$

As the wavelength of the frequency used to transmit energy or data increases, the energy loss will also increase. However, with increasing wavelength, the size of antenna required to capture an equivalent amount of energy at the same distance decreases. This obliges a good consideration of a size/transmission efficiency trade-off in order to reach desired specification parameters.

In the ISM bands, power is regulated by authorities. Generally, in the 433, 900, 2400 and 5000 MHz bands, power is limited to levels of around 1, 500, 10 and 25 mW, respectively, in France [23]. This does impose a certain “maximum distance” from which a node can operate, antenna gain (directive radiation) notwithstanding.

Section I.b – History of Wireless Power Transfer

Electromagnetism is a ubiquitous part of our everyday lives, and appears in many different formats. It is a very present, if not a predominating force, in most modern economic sectors, whether they be primary, secondary or tertiary in nature.

In this section, in order to understand how, and subsequently, why WPT has become a driving factor behind recent technological trends, a brief history of electromagnetism will be presented. This will be further expanded upon with the history of WPT, as well as current and future trends in the domain.

Subsection I.b.1 – A brief history of electromagnetism

Although electricity and magnetism were phenomena that were observed early in human history, thorough, preliminary research on the nature of electromagnetism can be traced back to the 17th century, where electricity and magnetism were both described as separate phenomena by William Gilbert in 1600 [24] . The first experiments on conductivity were performed by Stephen Gray in 1729, who created the field of electrostatics [25].

Further developments in the late 18th and early 19th century led to the establishment of many basic laws and units that serve as the framework for electricity and magnetism. These include, amongst many others, the discovery of magnetic fields induced by electric currents by Hans Ørsted in 1820, with subsequent analysis by André-Marie Ampère, and the discovery of electromagnetic induction in 1831 by Michael Faraday [26], [27]. These discoveries laid the foundations for James Clerk Maxwell's work on electromagnetism, which culminated with the development of Maxwell's equations, which were experimentally verified by Heinrich Hertz [28].

Subsection I.b.2 – The Development of WPT

Maxwell's postulation of a mathematical description of electromagnetism permitted further research to be done in a multitude of domains, one of which is WPT. Work in this domain began shortly after Hertz proved it was possible to scientifically create radio-waves. It should be noted that most research in WPT was done using far-field apparatuses from the late 1890s to the late 1970s.

It was Nikola Tesla who first envisioned using EM waves to wirelessly transfer energy. In the 1890s, he first demonstrated energy transfer through inductive and capacitive coupling at 10 kHz, as shown in fig. 7.a [29].

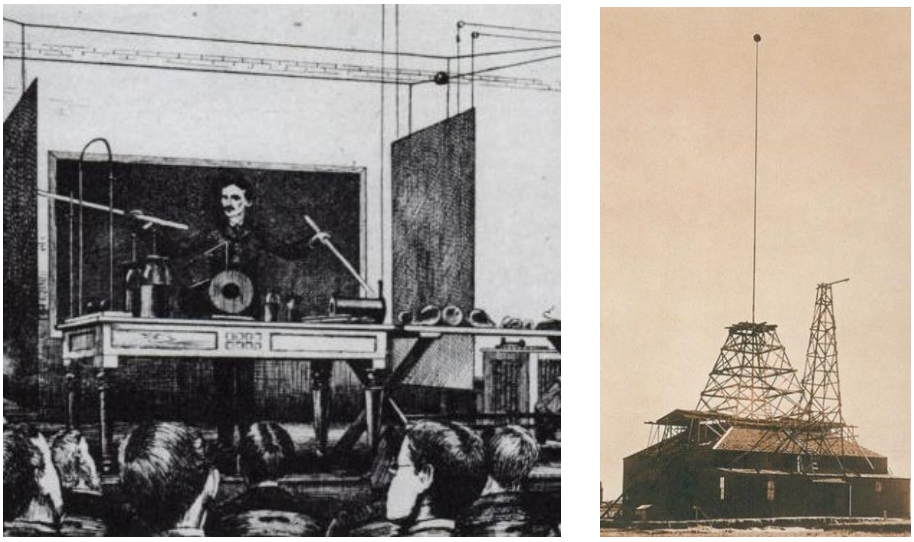

(a) **(b)**

Figure 7 - Nikola Tesla's WPT experiments, (a) shows powering via inductive coupling at Columbia University in 1891 [29], and (b) shows his attempt as long-distance remote powering at 150 kHz [30].

In 1899, Tesla carried out the first experiments in long distance WPT, by feeding 300 kW of energy into a coil resonating at 150 kHz, on top of a 60-meter tower in Colorado, displayed in fig. 7.b. Reportedly, a lightbulb was turned on at a distance of 20 meters from the base of the tower.

Advancements in WPT were unforthcoming during the next half-century. Efforts during this time period focused mainly on improving existing technology with the creation of devices capable of generating radio-waves, increasing the frequency of transmission for telecommunications and the development of new modulation techniques [31].

It was only in the 1960s that renewed interest in WPT reappeared, with the appearance of devices capable of generating microwave frequencies (1-10 GHz) at high power and high efficiency. Raytheon developed a mobile, wirelessly powered helicopter platform [32]. Although the project was not completed, a low-flying demonstration module was developed, fig. I.8.a. The system operated at 2450 MHz, with 5 kW sent from the source, (a magnetron fed to a parabola by a feed horn), fig. 8.b. 270 W of power was available at the rectenna, fig. 8.c. The helicopter could be operated 15 meters above the emitter for over 10 hours [32].

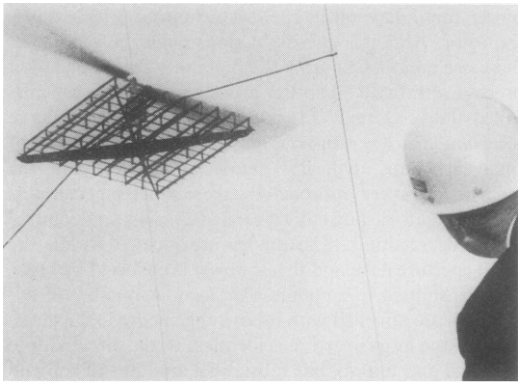

(a)

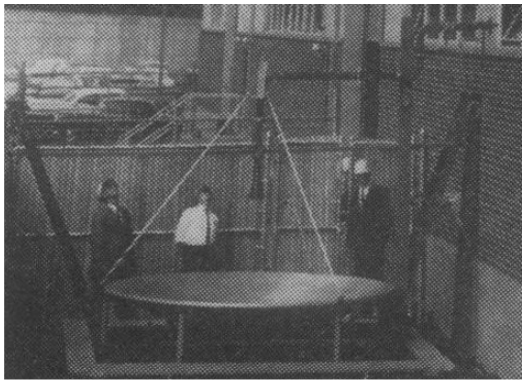

(b)

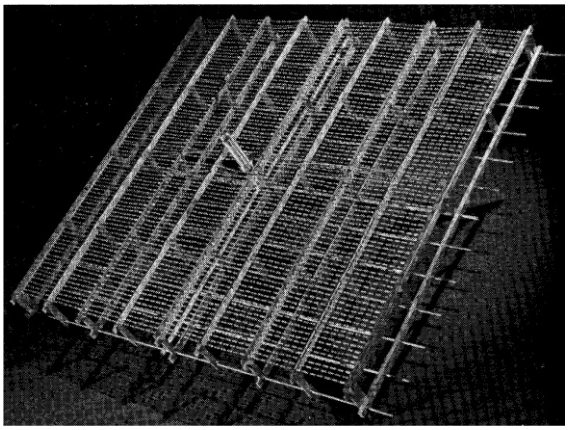

(c)

Figure 8 – Wirelessly powered helicopter. (a) shows the helicopter in operation, maintained stable by visible guide rails. (b) is the source, a magnetron emitting at 2450 MHz with 5 kW of power. (c) is the actual rectenna on the helicopter, made of 4480 1N82G point-contact diodes [32].

Further work involving Brown was also undertaken in the 1970s, with the progressive development of increasingly powerful microwave transmission systems. This culminated in a long-distance WPT experiment at Goldstone, in California, fig. 9.a [33].

(a)

(b)

Figure 9 – The NASA JPL experiment at Goldstone. (a) shows the receiver on the far left, and the emitter on the right. (b) is an up-close view of the receiver array [33].

The emitting device was a klystron, operating at 2.388 GHz, and radiating 450 kW of power through a large parabola. The receiver device was located 1.54 km away, and was made up of 17 rectenna elements, fig. I.9.b. Overall, the system presented an incident rectification efficiency of 81.53%, and outputted up to 30.4 kW of usable DC power, which demonstrated a total system efficiency of 6.8% [33].

Fig. 10 below presents an abridged overview of the history of WPT:

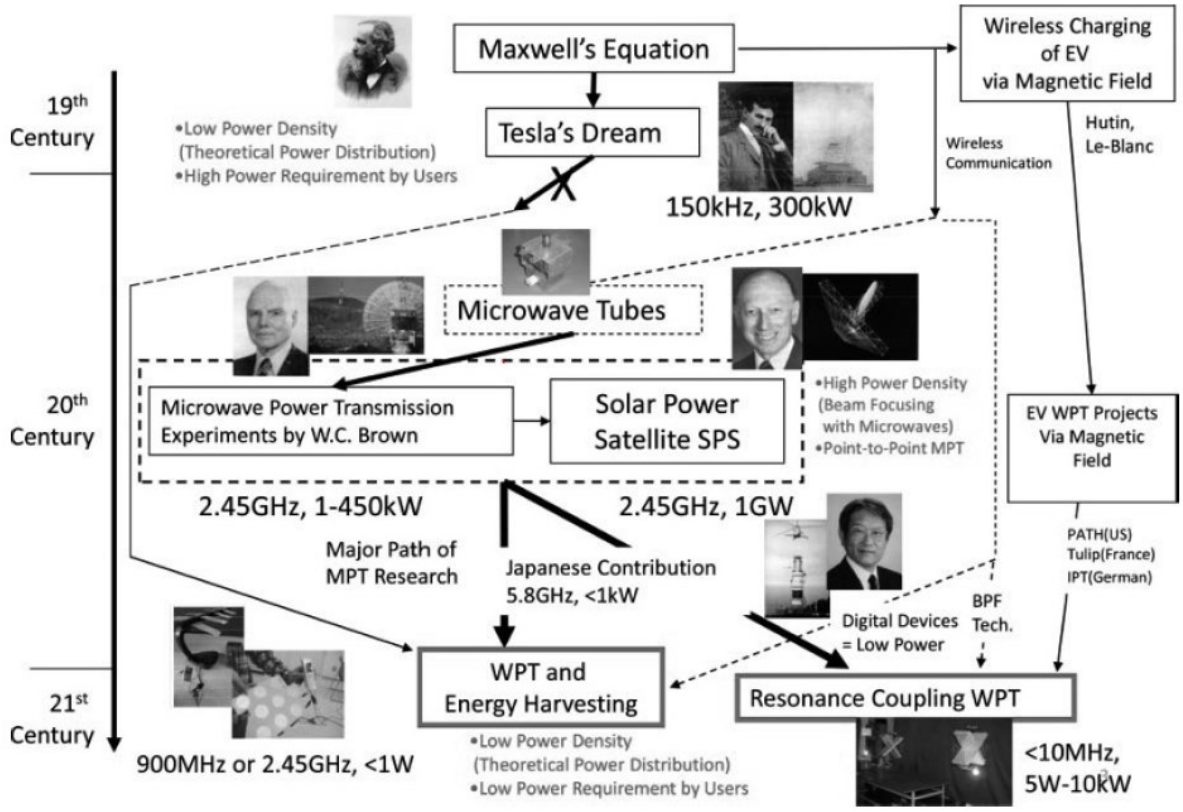

Figure 10 – A brief overview of the histosry of WPT [34].

Section I.c – Current Applications of WPT

WPT is a vast field with many diverse applications, therefore it is impossible to list them all in a synthetic manner. In order to present a brief overview of the diversity of WPT, three examples of the technology currently in use are presented below: RFID tags, Mobile Consumer Appliances and Wireless Vehicle Charging. It should be noted, that currently, many applications of WPT are near-field, due to the high efficiency of energy transfer efficiency that can be obtained by using such methods. However, for certain applications, WPT in the far-field is gaining traction, especially if low-power, lost cost beamforming becomes technologically feasible [35]. This section explores some of the more common applications of WPT.

Subsection I.c.1 – RFID/NFC

A common use for wireless power transfer is in the form of short-range communications. Many different modern-day services depend on wireless methods of communication (and by extension, powering), as they are passive devices without any energy storage capabilities. Many of these devices used are known under the name of Radiofrequency Identification (RFID) or Near-field Contact (NFC).

Such devices include biometric passports, in which a chip containing the same data in the passport, along with other biometric data (such as fingerprints, if necessary), are stored in a chip which can be accessed wirelessly. This scheme makes it harder to falsify passports, as the chips use asymmetric encryption, of which the private key is only known by the issuing authority, such as a government [36].

Another example is for asset tracking. Many objects, packages or items need to be able to be easily located for logistical purposes [37]. Although it is possible to simply affix a serial number and read the information manually, it is easy to simply add a redundant RFID chip within the same label containing equivalent information. This way, it is possible to easily read the information with a wireless scanner type device, or reduce the amount of time interpreting information presented on the object, as it is can be easily obtained in an automated manner from the chip embedded within the asset tracking label. Accessorily, such devices can also be used for theft prevention (such as in shopping establishments), where an alarm can go off if the tag affixed to the object is not de-activated (as would be done during

an authorized purchase) [36], [37]. Fig. 11 shows several examples of these consumer applications.

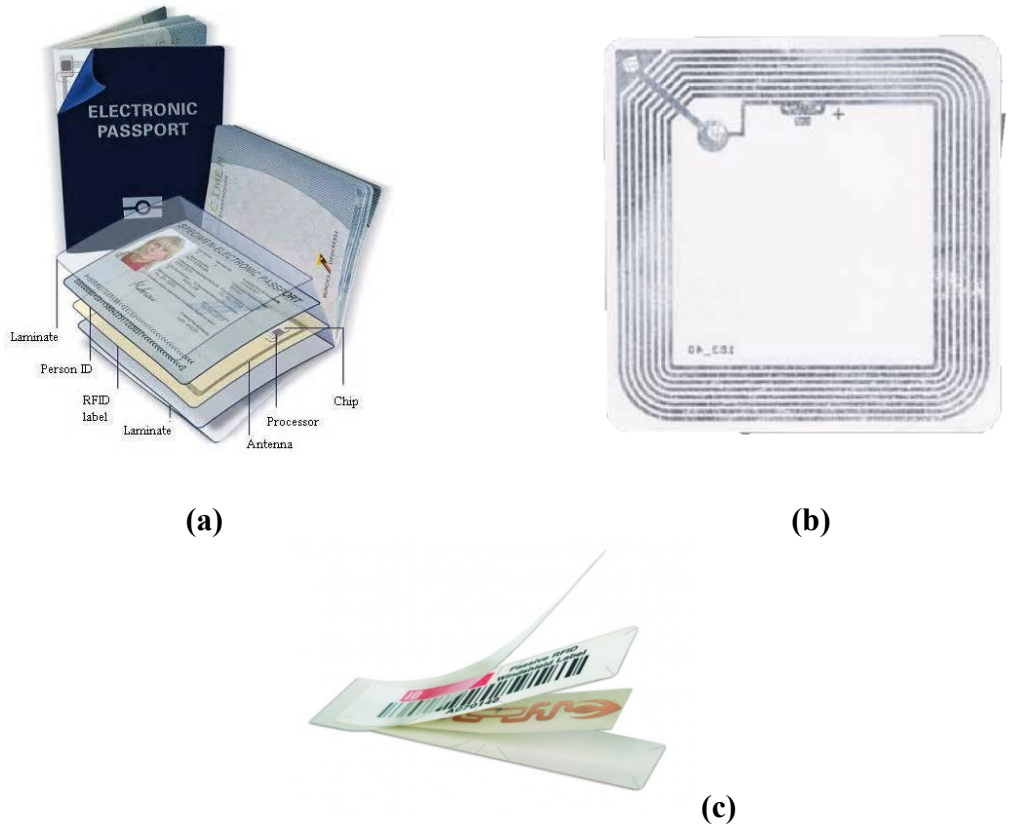

Figure 11 - Examples of consumer applications for RFID tags. (a) is a biometric passport, which contains an RFID system which can provide an electronic duplicate of data on the passport [38], (b) is a common RFID tag, such as those found on consumer appliance packaging in retail stores to prevent theft [39], and (c) shows an RFID tag that can be used for asset tracking within an organization [40].

Subsection I.c.2 – Wireless Sensor Networks

Several important applications for WSNs are, for instance, the development of sensor networks in vehicles, in order to reduce cabling present in such systems [41]. "Smart Home" networks can also be implemented by collecting environmental data in living environments, for instance in order to manage energy consumption in a more efficient manner [42].

Of particular interest is also the medical WSN/IoT domain, which is becoming increasingly relevant due to the presence of an aging population in developed countries. As the demand for skilled medical professionals is projected to increase in the coming years, it would be more efficient to monitor patients and do diagnostics remotely, in order to increase the efficient use of personnel [43].

Subsection I.c.3 – Wireless Vehicle Charging

Increasing environmental constraints have given rise to new, more CO_2 friendly vehicles, operating with batteries and electric motors, in order to meet their energy requirements. In contrast to thermal engines, however, which simply require fuel in a storage tank, electrical vehicles carry less mileage between refills, and need to be charged. Until recently, charging an electrical vehicle required it to be tethered to a cable for several hours in order to fully charge [44].

However, highly efficient (greater than 95%) wireless changing systems, operating at lower frequencies have appeared. These operate through inductive coupling, as shown in fig. 12:

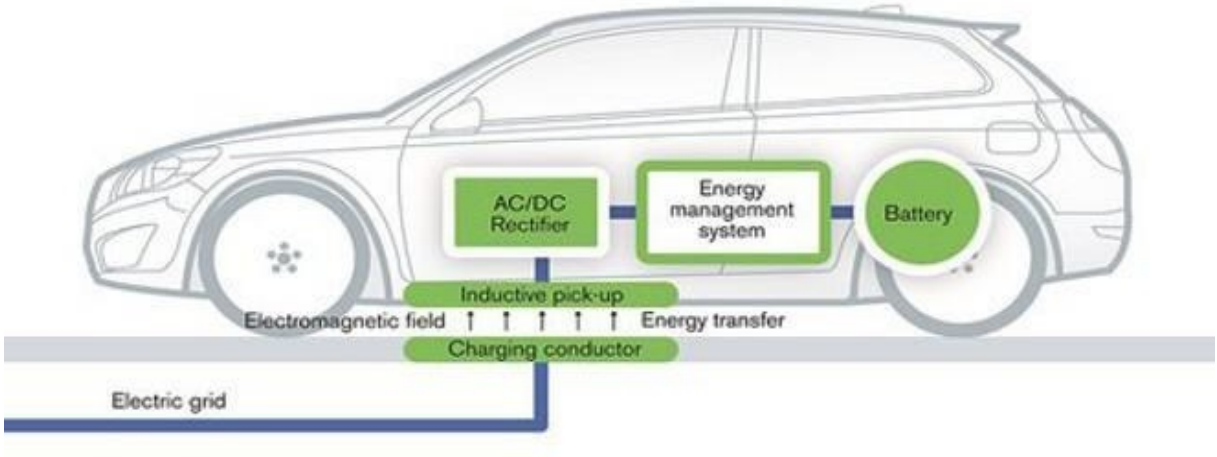

Figure 12 – Schematic overview of wireless vehicle charging [45].

Wireless charging, if used with a unifying standard, presents several advantages over wired charging. Notably, it is not required for the user to plug in a cable every time a charge is required. In case of forgetfulness, this may be useful in order to have a continuously full battery. Another advantage is that of having compatible chargers present in all parking spaces that the user many uses. This would have the advantage of not tethering the user to charging stations, especially if they are not in the parking location. Lastly, wireless charging can be useful to avoid vandalism. Cables can be cut, and charging stations can also be damaged, as they tend to stick out of the ground. Wireless charging stations can be embedded into the ground, which makes them less susceptible to damage.

Section I.d – System Overview

This work will focus on the design, creation, fabrication and measurement of a "proof of concept" low-power WPT system. The receiver is subdivided into modules in order to permit thorough investigation of them. The modules are as follows:

- Antenna module: the antenna is the essential element for turning radio waves (photons) into electrons.
- Rectifier (Rectenna) module: rectifiers serve a dual purpose in this work: turning electrical RF waves into harvestable DC energy and data signals.
- Power Management module: maximizes the throughput of DC energy into the system, manages the storage of energy, and created suitable power rails to power the system.
- Energy Storage module: stores the energy harvested from the rectifiers by the Power Management module.
- Processing module: the heart of the sensor, which processes data received, stores relevant data, and acts on any commands sent to the sensor.
- Demodulation module: turns rectified data signals into signals, and generates a wake-up signal that can be used by the Processing module.
- Sensor module: collects environmental data, and interacts with the Processing module.
- Feedback module (optional): can send data back to any system requesting information for the sensor, via a transmitter.

A diagram of the sensor module is presented below, fig. 13:

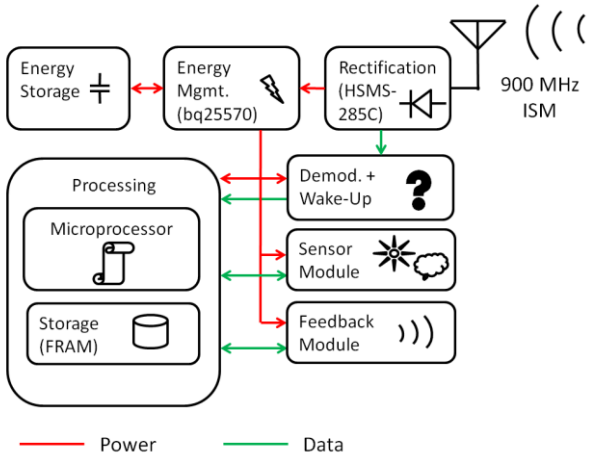

Figure 13 – Receiver overview, decomposed into modular subsystems.

The transmission front-end is a software defined radio (SDR) system, connected to a computer. Protocols, power levels, transmission frequency, modulation schemes, and all associated characteristics are software controlled and can be parametrized. An overview of the transmitter front end is presented in fig. 14 below:

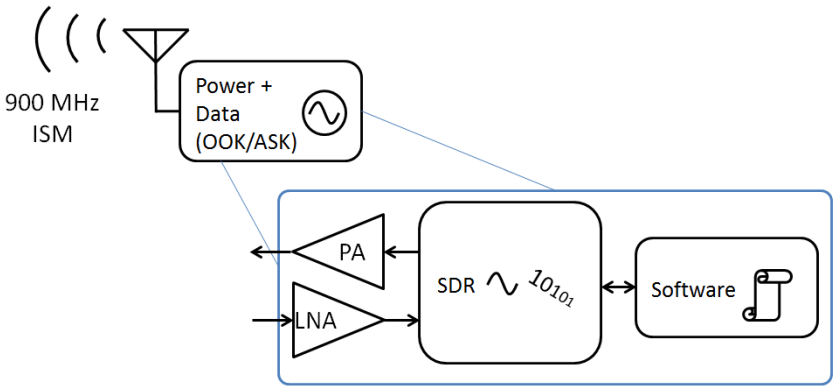

Figure 14 - Transmitter overview.

Details on this system are presented in the rest of this work, which will include the strong and weak points of each different module, as well as a thorough analysis of their metrics and operation.

This page intentionally left blank.

Chapter II

System Modules

This page intentionally left blank.

Chapter II System Modules

Section II.a – Introduction

This work will involve studying the feasibility of a WPT/WPH node, by analyzing its performance for use in possible scenarios of application as a low power, battery-free IoT node. The node is composed of various modules, and the objective of this chapter is to describe the different modules making up the node, define and characterize their associated metrics and performance, and describe any limiting factors.

In order to make the timeframe of this thesis acceptable, COTS components were used to design this system's submodules. The implications of this decision are that the system will generally not be optimized compared to highly specialized Very Large-Scale Integration Application Specific Integrated Circuits (VLSI ASICs); however, it is possible to operate the system at relatively low power levels, and use the design as a proof of concept for further design optimizations.

Section II.b – Rectenna

In this section, the rectifications modules of the node will be described and measured. The position of the rectifier in the node is presented in fig. 15:

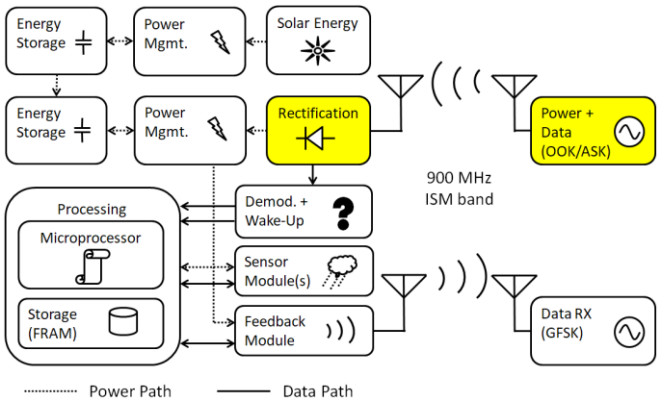

Figure 15 – Position of the rectifier module in the node.

Rectifiers are a staple component in any system that uses wireless energy to power itself. These devices convert Alternating Current (AC) energy into Direct Current (DC) energy, by rectifying the energy presented to them. The most common use for rectifiers in modern devices is to turn AC power present on the electrical grid into DC power, usable by electronic devices that require DC order to operate. In this work, rectifiers will be used for two purposes. The first is to transform RF energy into DC energy for use by Wirelessly Powered Nodes (WPNs) present in Wireless Sensor Networks (WSNs). The second is to receive digital amplitude-modulated data, with Asymmetric Shift Keying (ASK), or On-Off Keying (OOK) modulation schemes. The reception of digitally modulated data can be used in order to perform wake-up or addressing functions for the wireless sensor node as a whole. The use of analog modulation schemes is not recommended, due to the difficulty of accurately reproducing the analog signal, due to the rectifier's non-linearity.

Trends in the use of WPT to power RFID tags, and more recently, WSNs, have made rectifiers a highly studied domain in the past years, in order to maximize their performance and efficiency at various power levels [46], [47]. Different topologies have also been analyzed in order to be implemented depending on the usage scenarios for these devices, and in order to appropriately size matching networks between the rectifier and the antenna [48].

Subsection II.b.1 – Overview and Metrics

Classic topology for a rectenna consists of an antenna, a matching network, a rectifier, and an output filtering capacitor, as shown below in fig. 16:

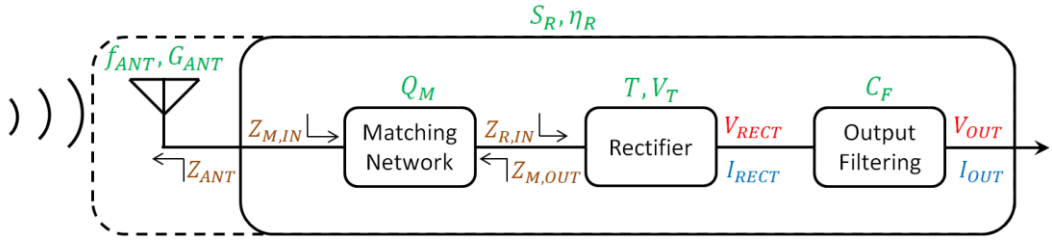

Figure 16 – General rectifier topology for an RF to DC module and associated metrics.

Important metrics of this module include the following:

- For the antenna: output impedance Z_{ANT}, gain of the antenna G_{ANT}, and operating frequency of the antenna f_{ANT} ,
- For the matching network: input impedance $Z_{M,IN}$, output impedance $Z_{M,OUT}$, and quality factor Q_M ,
- For the rectifier: topology type T, diode voltage threshold V_T, input impedance $Z_{RECT,IN}$, as well as the voltage V_{RECT} and current I_{RECT} outputs,
- For the output filter: capacitance size C_F, as well as the voltage V_{RECT} and current I_{RECT} outputs,
- For the overall subsystem: system sensitivity S_R and system efficiency η_R. It should be noted that these two metrics can either include or exclude the antenna, depending on the desired measurements (either as a rectenna, or as a rectifier only).

The sensitivity of a rectifier is defined by:

$$S_R = V_{OUT}(P_{IN})$$

The efficiency of a rectifier depends on the load applied. It is defined by:

$$\eta_R = \frac{P_{OUT}(R_L)}{P_{IN}} = \frac{{V_{OUT}}^2}{R_L \cdot P_{IN}}$$

The different subsections of this module will now be explored in order to determine the importance of the aforementioned metrics in terms of performance.

Subsection II.b.2 – Antennae

The antenna used for the reception of energy is presented in fig. 17. The design is based on a multi-branch folded dipole antenna, it is sourced from [49].

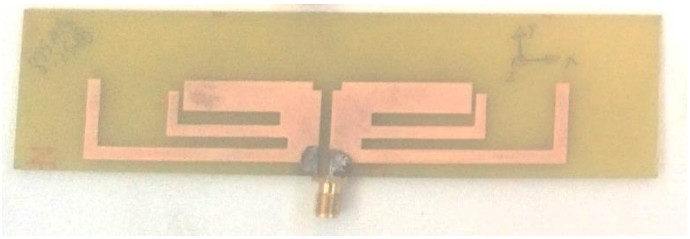

Figure 17 – Folded dipole antenna, operating at 935 MHz.

As can be inferred from figure 18, the antenna presents a gain G_{ANT} = 2 dBi in the direction of radiation. The operating frequency is f_{ANT} = 935 MHz. The -10 dB bandwidth of the antenna is 90 MHz, ranging from 870 MHz to 960 MHz. As the antenna is a dipole, the radiation pattern is quasi-isotropic, and the node can receive energy from any direction. The radiation pattern and the measured S_{11} parameters of the antenna are presented in fig. 18:

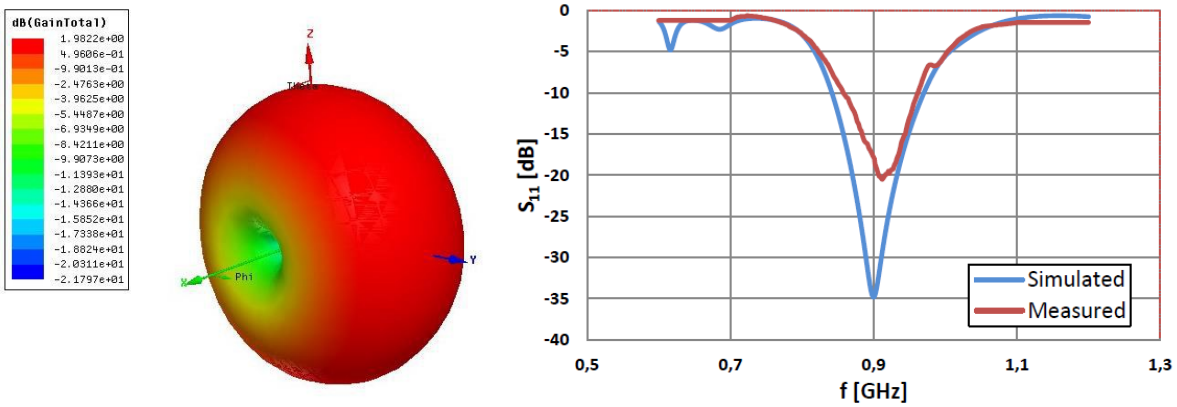

(a) (b)

Figure 18 – Performance of the antenna. The simulated radiation pattern of the antenna is shown in (a), and (b) shows the measured and simulated S-parameters [49].

It can be seen that the antenna's measured results closely match the simulations, for the input return loss S_{11}. The small discrepancy observed, 1% of the input return loss, is inherent to the manufacturing process. The proposed antenna ensures an input return loss lower than -15dB from 885 MHz to 930 MHz. Similarly, the measured gain, at around 1.5 dBi, closely matches the simulated gain, at 1.98 dBi.

Subsection II.b.3 – Rectifier Topologies

Different topologies are available for RF rectifying circuits. The topologies provide different advantages and drawbacks, and must be analyzed in order to determine the most suitable one for the reception of data and the reception of energy by the node. There are three basic approaches to rectification [48]:

- A first passive method involves diodes in order to convert an AC waveform into a DC output. The advantages of this type of topology are that it uses components off the shelf (COTS), and performs well in RF rectification with Schottky diodes. However, it is difficult to obtain repeat performance due to matching difficulties, and is not available on silicon-based technologies, which creates extra development costs.
- A second passive method exploits diode-connected transistor in CMOS ASICs to rectify the AC signal. A part of the rectified energy is dedicated to maintain transistor polarization for higher efficiencies. However they are limited by reverse breakdown voltage which shifts with technology scaling. In order to be reliable, specific transistors with large gate oxides are mandatory [49].
- The third method involves the use of a chopper circuit to convert DC energy to a higher voltage. Although this approach is efficient, rectification process based on active circuits are limited to the MHz range due to the amplifier bandwidth.

The most fundamental rectifier topology is the half-wave rectifier (also known as the Villard rectifier), fig. 19. Although this circuit is simple to implement, it has the drawback of only rectifying positive parts of the incoming AC waveform, whilst clamping negative parts of the AC cycle to ground. As a result, approximatively 50% of incoming AC energy, that could be converted to DC energy, is wasted. The operation of this circuit is assured by charging C_1 to V_{peak} through D_1.

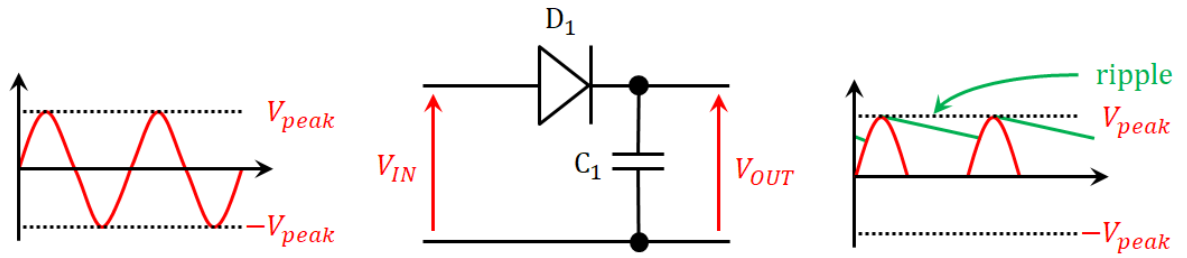

Figure 19 – Half-wave (Villard) rectifier topology.

A more efficient topology is the full-wave rectifier, fig. 20. This circuit is capable of rectifying both the positive and negative parts of an AC signal into DC output, with output amplitude which is double the input amplitude. This is done through the use of capacitors. When the AC waveform, at the input of the rectifier, decreases, then capacitor C_1 is charged to the amplitude of the input waveform through D_1. As the input increases, then capacitor C_2 is charged to the same amplitude through D_2. The result in an output which is around twice the input amplitude at its peak, as both capacitors, charged to V_{peak}, are seen in series by the output.

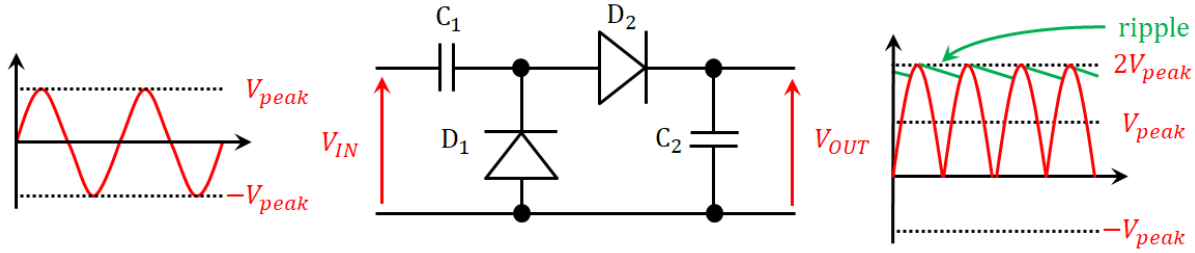

Figure 20 – Full-wave (Greinhacher) rectifier topology.

Another popular full-wave topology is the bridge rectifier, fig. 21. This rectifier is similar to the previous one, however it delivers an output voltage that is of the same amplitude as the input voltage. When the AC waveform is positive, D_2 and D_3 conduct, and let the current pass, and inversely, when the waveform is negative, then D_1 and D_4 conduct, letting the current pass. The output is smoothed by capacitor C_1.

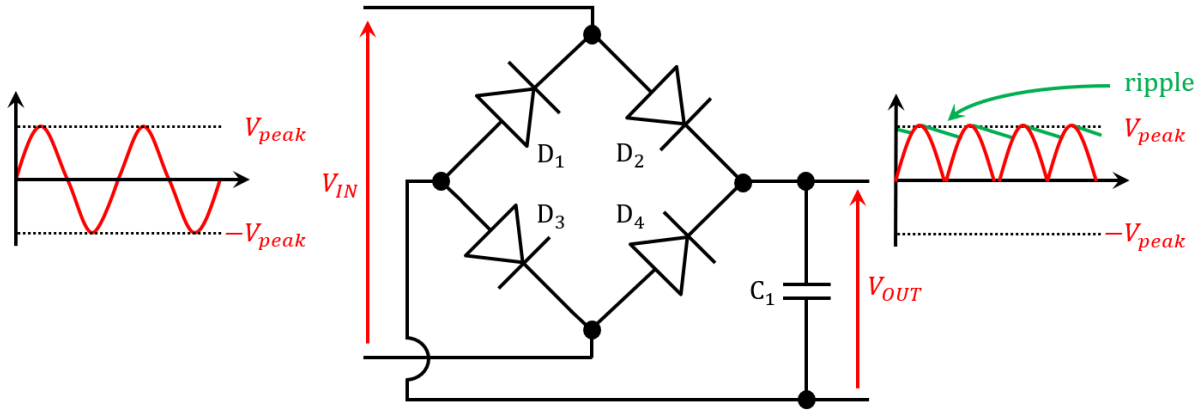

Figure 21 – Bridge (Delon) rectifier topology.

It is possible to create differential topologies from the basic rectifiers explored above, in order to increase the output voltage. This can be done by either creating differential forms of the half-wave or full-wave rectifier (the bridge rectifier is already in a differential configuration), as illustrated in fig. 22.

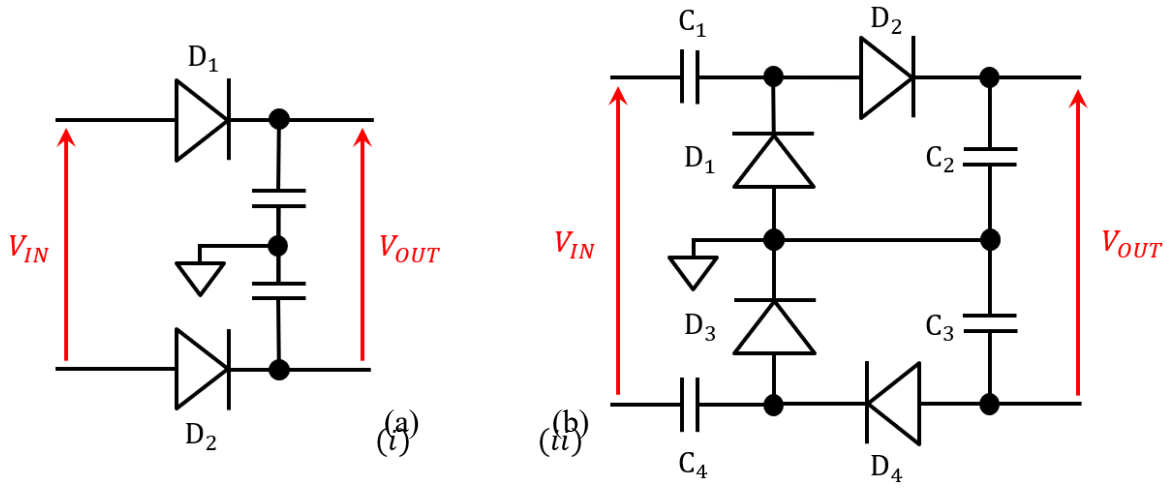

Figure 22 – Differential half-wave (a) and full-wave (b) rectifiers.

However, these topologies have grounding problems when used as rectifiers of RF signals, as the input signal is required to be fully differential, which would imply the use of a floating ground plane for rectification, or a dual-input RF source.

Single-ended configurations can be cascaded in series, which can provide increased sensitivity, albeit potentially at the cost of decreased efficiency in power output. These are known as voltage multipliers. A voltage multiplier rectifier, known as the Villard Cascade, fig. 23, is a combination of half-wave rectifiers. It is also known as a Cockcroft-Walton

generator. By combining half-wave rectifiers in series, the voltage output can be increased to n times the voltage input.

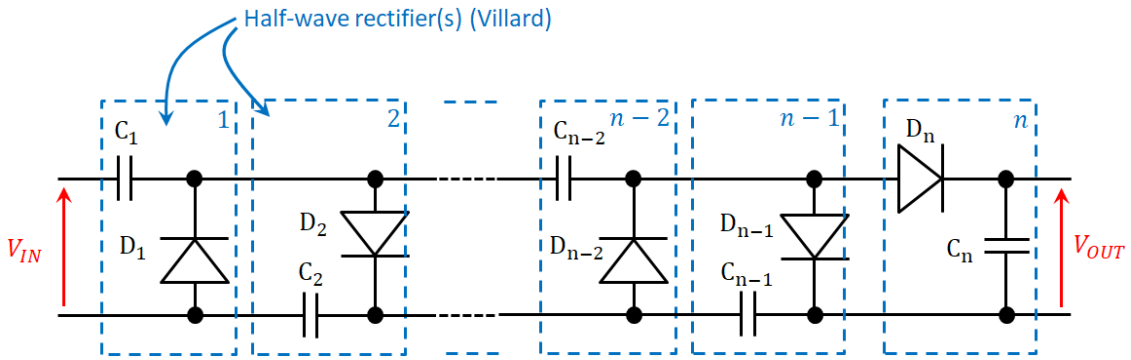

Figure 23 – Villard cascade (Cockroft-Walton) rectifier topology.

Similarly, full-wave rectifiers can be cascaded together, fig. 24. This voltage multiplier is known as a cascade Greinacher rectifier. Compared to the Villard cascade, the voltage output can be increased to $2n$ times the voltage input, using the same number of diodes its half-wave counterpart.

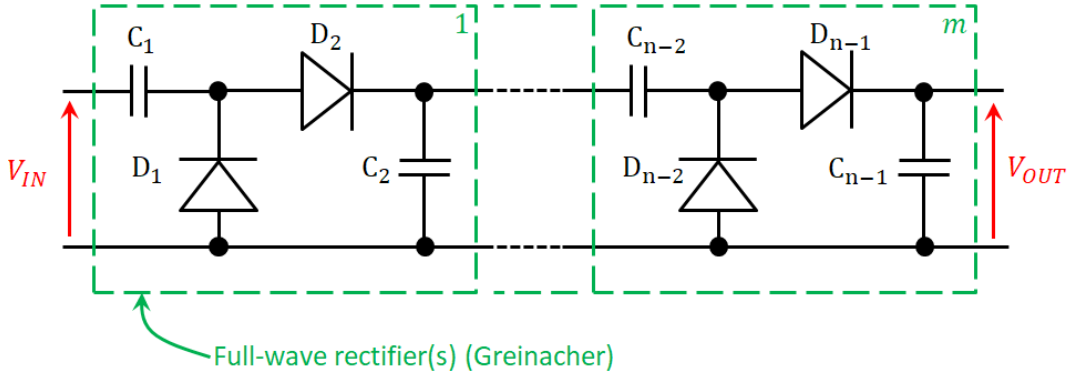

Figure 24 – Greinacher cascade rectifier topology.

Voltage multipliers also exist under the form of charge pumps. A typical charge pump, known as the Dickinson charge pump, fig. 25, is composed of a cascade of half-wave rectifiers, with each Dickinson stages' output capacitor grounds connected to the clock signal CLK and $\overline{CLK}$, respectively. As the clock alternates between high and low levels, the half-wave rectifiers within the Dickinson stage, depending on their connection to CLK or $\overline{CLK}$, are blocked or allowed to conduct. The voltage output can be increased to $2n$ times the input with this topology.

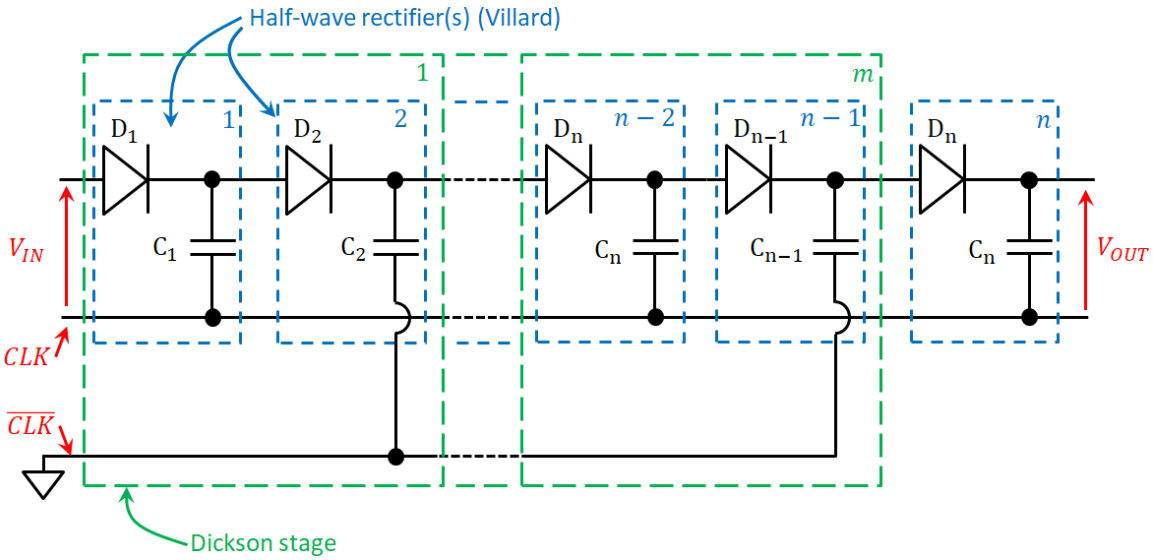

Figure 25 – Dickinson charge pump topology.

However, as an AC RF waveform is the only energy source available for use in the node, the latter topology will not be considered in its current form. This is because the use of chopper-controlled rectifiers would increase the power consumption of the node, as circuits would require the generation of a clock signal, which consumes a significant amount of energy in regards to the amount of energy available [48].

This can be remedied by choosing a different cascading topology. In classic low frequency (LF) rectifiers, the stages of voltage multipliers are generally cascaded in series, however, this can lead to severe losses in RF rectifiers, as the signal propagates through the different stages [48].

It is therefore preferable to adopt a different topology, by cascading the rectifier stages in a pseudo series-parallel manner: the outputs of the rectifiers are daisy-chained in series, but their inputs are in parallel to the RF input, fig. 26. Similarly, this technique can also be applied to the Greinacher rectifier with multiple stages.

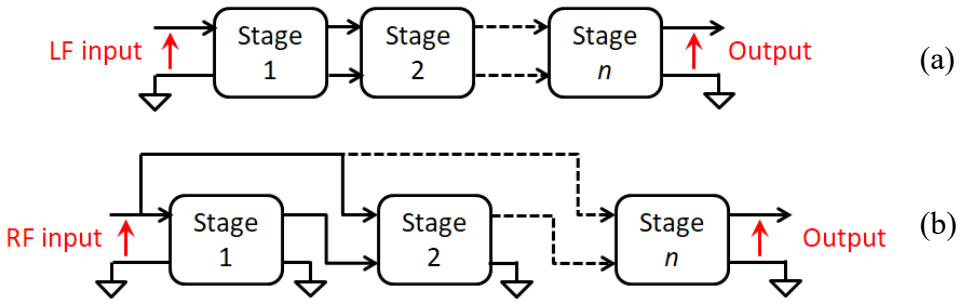

Figure 26 – (a) Classic topology for LF rectification, (b) improved rectification topology for RF rectification.

Three main choices for RF rectifiers using COTS diodes are therefore considered in this work:

- The modified Dickson charge pump,
- The modified Greinacher rectifier,
- The modified Villard Cascade rectifier.

Subsection II.b.4 – Rectifier losses

In order to model rectification loss, and to determine the most efficient topology, it is necessary to analyze the losses present in the rectifier, and compare them to the actual energy output. For half-wave and full-wave rectifiers, fig. 27 illustrates the losses and the actual extracted energy for these topologies from the perspective of the input.

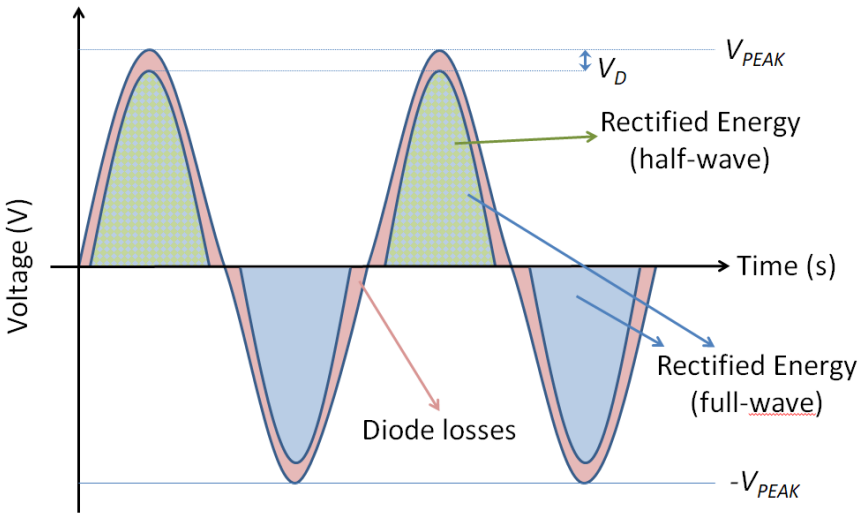

Figure 27 – Losses incurred during the rectification process.

There are a multitude of different types of diodes, used in many different applications, such as creating RF signals with Gunn diodes, creating laser or visible light, using the tunnel effect to create diodes exhibiting a negative resistance in a certain region, or even voltage references with the Zener diode, or rectifying with regular *p-n* junction or Schottky diodes.

The Schottky diode will be used for rectifier topologies in this work, for two main reasons. Contrarily to a *p-n* junction diode, Schottky diodes are made of a metal to *n* type semiconductor junction, giving them very low threshold voltages, generally from 0.15 V to 0.4 V. It also allows for rapid switching frequencies, as there is no recombination in the depletion region. This permits higher efficiencies when rectifying at smaller voltages. However, it should be noted that the reverse leakage current is higher than conventional diodes due to a lower breakdown voltage [50].

A modified form of the Shockley diode equation can be used to model Schottky diodes, called the Richardson equation [51]:

$$I_D = I_S \left[e^{\frac{V_D q}{nkT}} - 1 \right]$$

Where:

- I_D is the current flowing through the diode,
- V_D is the voltage across the diode,
- T is the absolute temperature,
- q is the elementary charge,
- n is the ideality factor,
- k is Boltzman constant,
- I_S is the saturation current.

At radio frequencies below 6 GHz [52], Schottky diodes can be modelled by the following equivalent circuit, shown in fig. 28 below:

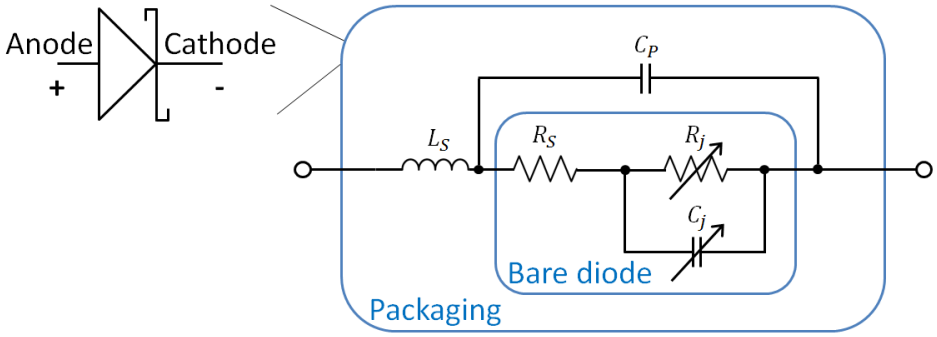

Figure 28 - RF model of the Schottky diode, including packaging parasitics.

The following parameters of the Schottky diode can be inferred from the above model:

- L_S and C_P are, respectively, the series inductive and parallel capacitive packaging parasitics.
- R_S is the series resistance of the diode, generally the summed packaging and die resistivities.
- R_j and C_j are, respectively, the junction resistance and capacitance. They vary depending on the voltage between the terminals of the diode.

  R_j is defined by:

$$R_j = \frac{\mathrm{d}V_D}{\mathrm{d}I_D} = \frac{n}{qkT(I_S + I_D)}$$

And for the Schottky diode, C_j is defined by (C_{j0} being the the zero-voltage junction capacitance, ϕB the barrier height, and M the junction grading coefficient):

$$C_j = C_{j0}\left(1 - \frac{V_D}{\phi B}\right)^M$$

This is, for Schottky diodes in forward conduction, approximately equal to:

$$C_j \approx C_{j0}$$

These parameters are used in order to simulate rectifier performance, and therefore choose the most appropriate topology.

It should be noted that the higher the output filtering capacitor C_F, the lower the data rate the rectifier will be able to receive. This is because the combination of the rectifier

impedance and the filtering capacitor will create a low pass filter. Generally, for data reception, a low capacitance is necessary, depending on the baudrate, while power harvesting can use a larger capacitor. Both capacitors should be low leakage in order to minimize power loss, thus, the use of ceramic capacitors is recommended.

The previously discussed topologies were simulated using perfect matching, in order to determine the most viable one to use in this work. Simulated sensitivity is presented in fig. 29, for 1 and 4-stage unloaded rectifiers.

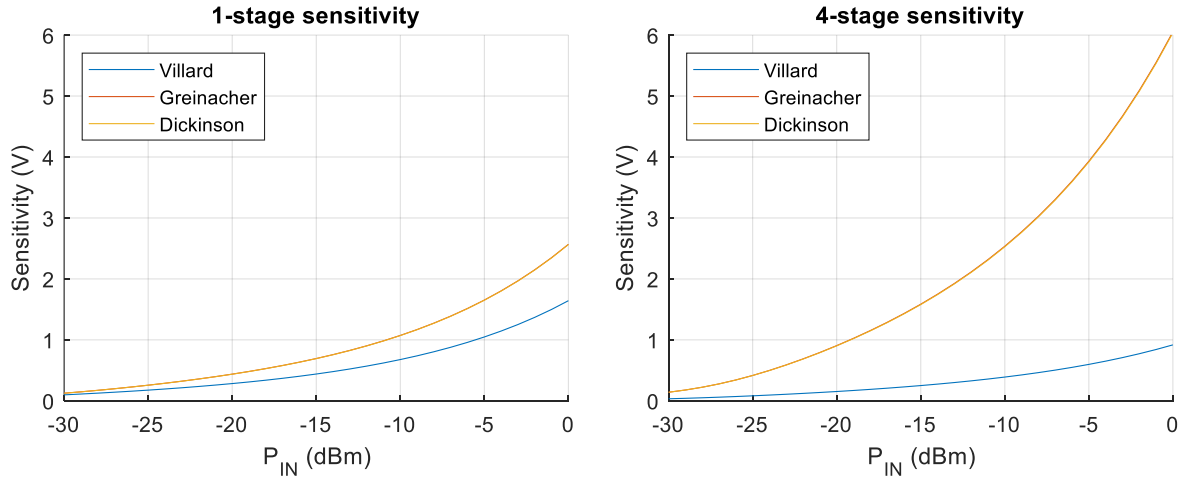

Figure 29 – 1 and 4-stage rectifier sensibilities.

It can be observed for the Greinacher and Dickinson rectifiers, that the sensibility increases as the number of stages increase. Furthermore, the sensitivity of the former rectifiers is quasi-identical. Therefore, for data reception use, either the Greinacher or Dickinson rectifier topologies should be considered.

For the remainder of this chapter, the expression “at optimal loads” will be defined as the best efficiency for a given load R_L for the range of power input P_{IN} specified, in order to present a best-possible scenario of power transfer, which is that of an adaptive load as a function of power input levels. Should the load remain constant, then at worst, efficiencies will be lower than simulated values.

Fig. 30 shows simulated optimal efficiencies for 1 and 4-stage rectifiers.

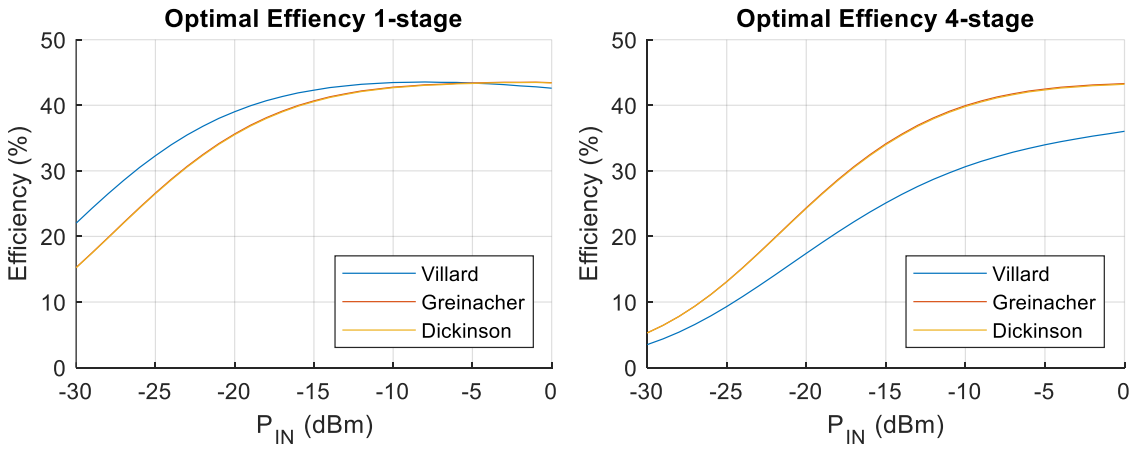

Figure 30 – 1 and 4-stage rectifier efficiencies.

For all rectifiers, efficiency tends to degrade as the number of stages increase, therefore, for powering, only single-stage rectifiers should be considered. It can also be seen that the Villard rectifier provides the highest simulated efficiency at lower power levels, by approximatively 2 to 7 % more than either the Greinacher or Dickinson topologies, when input power levels vary between -25 to -15 dBm. However, practical considerations must be considered in terms of power management, as the circuitry used in this work cannot extract power with voltage input levels below 200 to 300 mV. Fig. 31 shows the observed voltages at the output of the rectifier for the optimal loads of the previous figure at lower power levels.

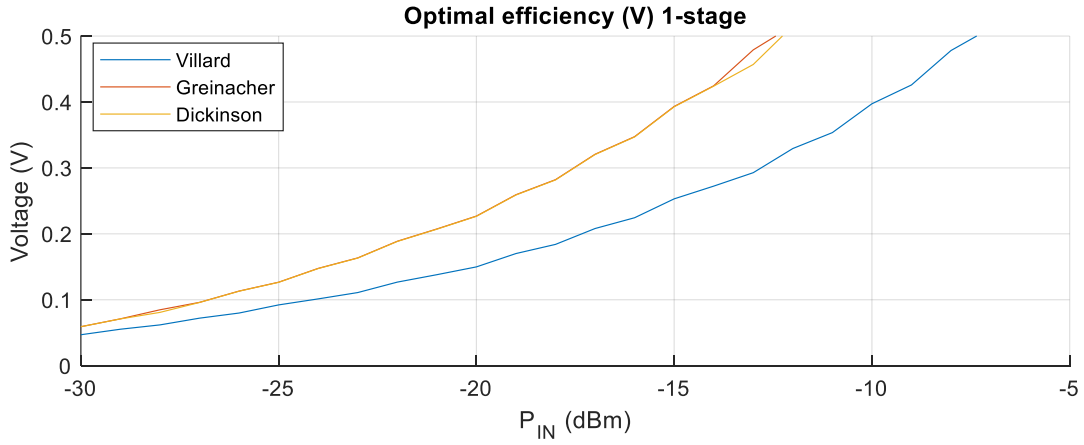

Figure 31 – Rectifier output voltages at optimized efficiency load points.

It can be observed that for the low power levels, particularly below -17 dBm, that the Villard rectifier's output is lower than the required voltage in order to maintain the operation of the power management module of the node. Therefore, it would be more appropriate to select a single stage Greinacher or Dickinson rectifier for powering purposes.

The performance metrics of both Greinacher and Dickinson topologies are similar; therefore either of them can be chosen in order to implement both the powering and data reception of the rectifier module in this work. The 1 and 4-stage Greinacher rectifiers were chosen for powering and data reception, respectively.

Subsection II.b.5 – Matching Network

The S_{11} parameters of the n-stage rectifiers are shown in fig. 32, before matching, from 700 MHz to 1.1 GHz, to emphasize the high capacitance present on the circuit's input.

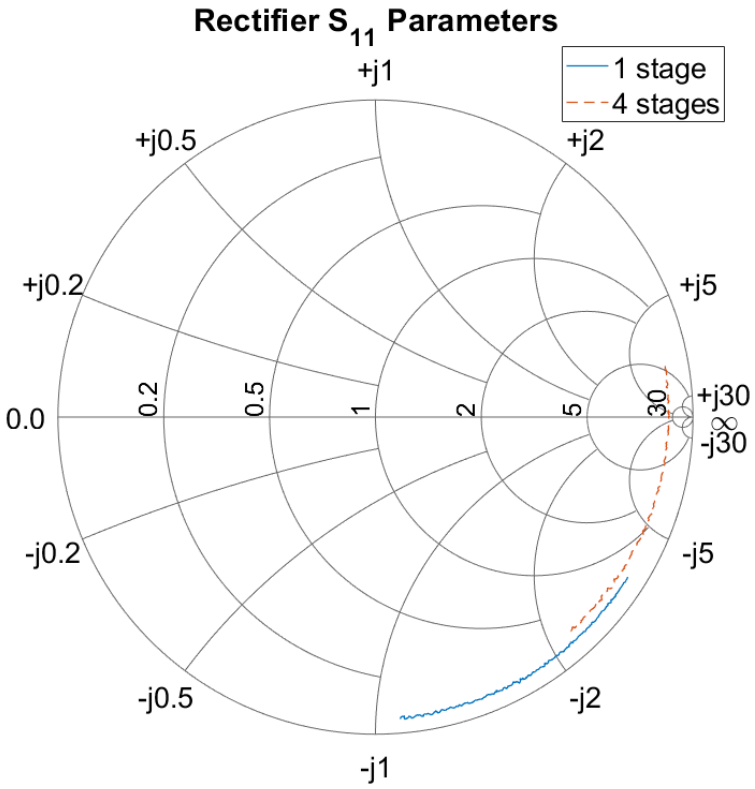

Figure 32 – Input S_{11} parameters for the 1-stage and 4-stage rectifier circuits, from 700 MHz to 1.1 GHz.

The purpose of matching is to bring the input impedance of the rectifying circuits to the antenna's input impedance, 50 Ω. Theoretically, a single stage "L" would offer the best performance. However, due to the difficulty of matching highly capacitive elements because of component tolerance, a double stage "L" network topology, fig. 33, was implemented instead.

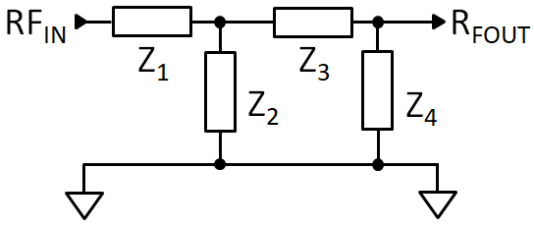

Figure 33 – Double "L" matching topology.

The matching network is designed to ensure an input return loss below -10 dB over more than 30 MHz at 935 MHz for each n-stage rectifier.

Due to varying diode capacitance C_j as a function of power input P_{IN}, the center frequency of the matched rectifiers tends to shift, though not significantly, fig. 34. This variation remains negligible regarding the achievable bandwidth over the considered range of power and targeted application. Indeed, for this node, the broadcasted data is sent at a low bitrate, requiring narrow bandwidth, and powering methods via RF often uses Continuous Wave (CW) carriers.

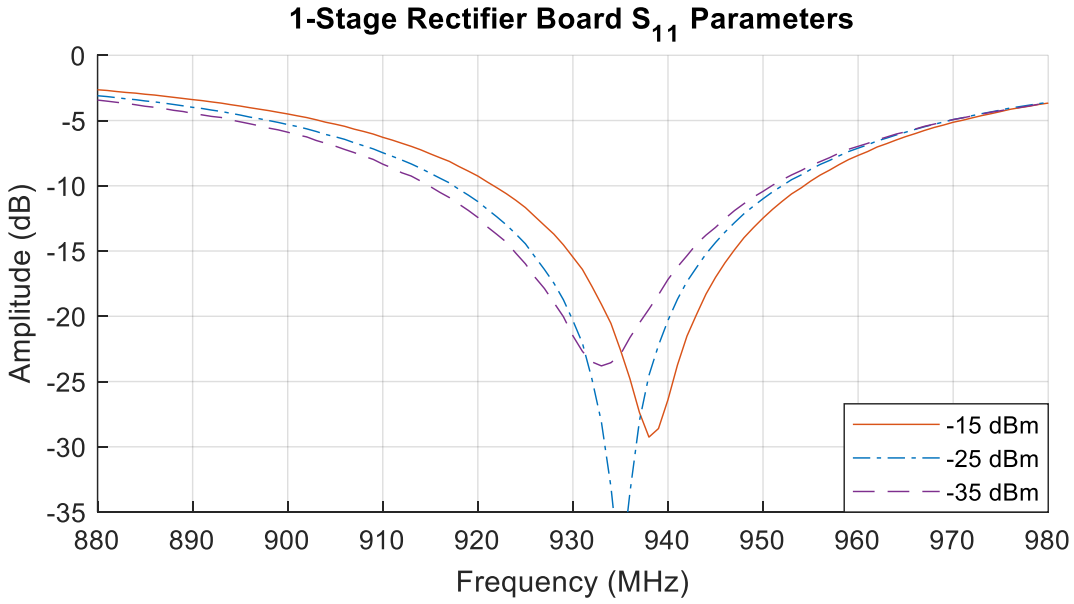

Figure 34 – Frequency shift incurred by the 1-stage rectifier due to varying capacitance as a function of changing input power levels.

Subsection II.b.6 – Implementation

The topology of the manufactured rectifier boards is presented in fig. 35:

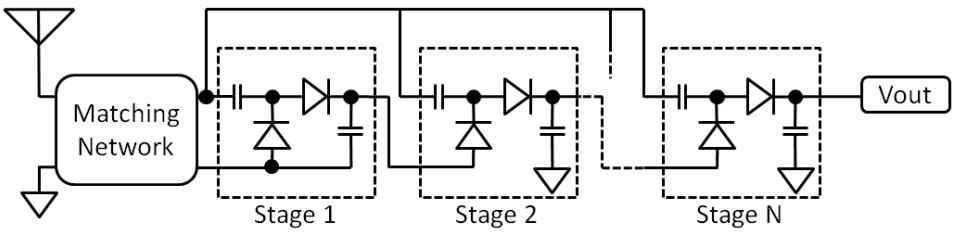

Figure 35 – Rectifier board topology.

The boards were manufactured on a classic, low-frequency, 2-layer FR-4 substrate, in order to minimize fabrication costs to keep the node's implementation cost to a minimum. The diodes used were the HSMS-285C series [52].

Matching network values were determined, and are presented in table 2:

	Stage(s)			
	1	**2**	**3**	**4**
Z_1	13 nH	5 nH	18 nH	short
Z_2	6.2 nH	24 nH	68 nH	open
Z_3	10 nH	24 nH	12 nH	27 nH
Z_4	91 nH	13 nH	9.1 nH	7.5 nH

Table 2 – Actual values of the matching circuit for different rectifier stages.

Due to the varying dielectric constant over frequency, matching posed a challenge, and did not correspond accurately to simulated values, due to limitations on the part of the simulation software, which was unable to implement a complex, frequency dependent dielectric model. Therefore, in order to determine the component values presented above, a two-step process was implemented. For the first part, the board was manufactured and assembled with simulated matching network values. The second part of the process involved dichotomously iterating of component values, in order to approach the desired S-parameter threshold. This was repeated until the S-parameter condition, -10 dBm, in the appropriate frequency range, was met.

The simulated and measured sensitivities for the 4-stage rectifier, which will be used for data reception, are presented in fig. 36:

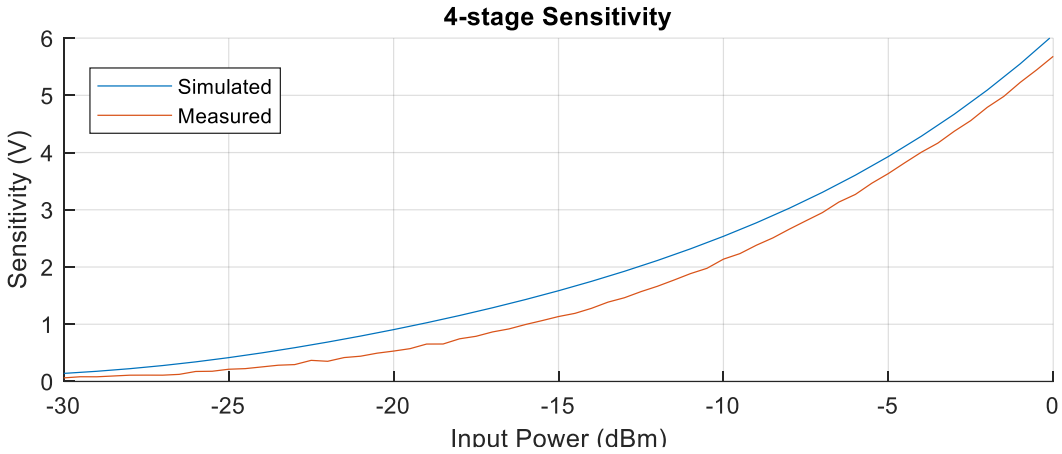

Figure 36 – 4-stage rectifier sensitivity.

It can be observed that the measured results are relatively close to simulated values, although measured values are slightly lower compared to simulation results. This is due to substrate losses and imperfect matching conditions, as simulations assume a perfect matching scenario with no transmission lines present between components. However, generally measurements closely match simulation results. The highest sensitivity is achieved when the power input is 0 dBm, at approximatively 5.5 V. For the range between -25 and -10 dBm, the sensitivity varies between 0.25 V and 2 V.

The simulated and measured efficiency for the 1-stage rectifier is shown in fig. 37:

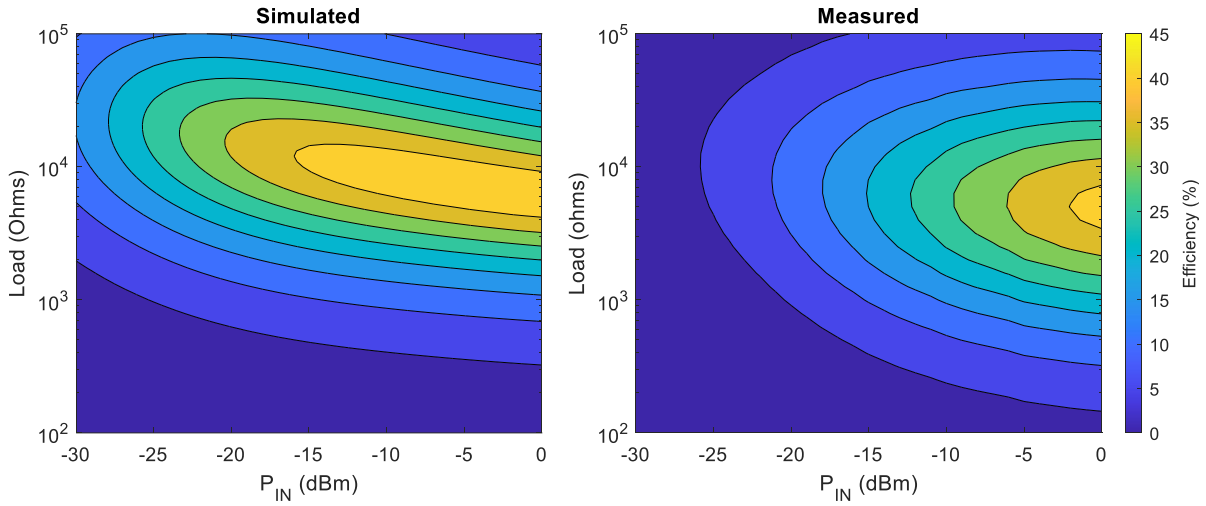

Figure 37 – 1-stage rectifier efficiency.

Similar conclusions can be made for the efficiency, which is to say that measured values are similar. The larger discrepancy in simulated and measured values for the efficiencies can be extrapolated from the different definitions between the sensitivity of the rectifier, and that of efficiency. The power available (and thus, efficiency) is proportional to

the square output of the voltage, increasing the difference at lower power levels, especially in the -25 to -10 dBm zone. Increased efficiency could be achieved by optimizing the matching network further, and changing board layout. Measured and simulated efficiencies at various loads range from around 5 % to 45 %, depending on the power input level.

The above efficiency is then presented at optimal loads in fig. 38:

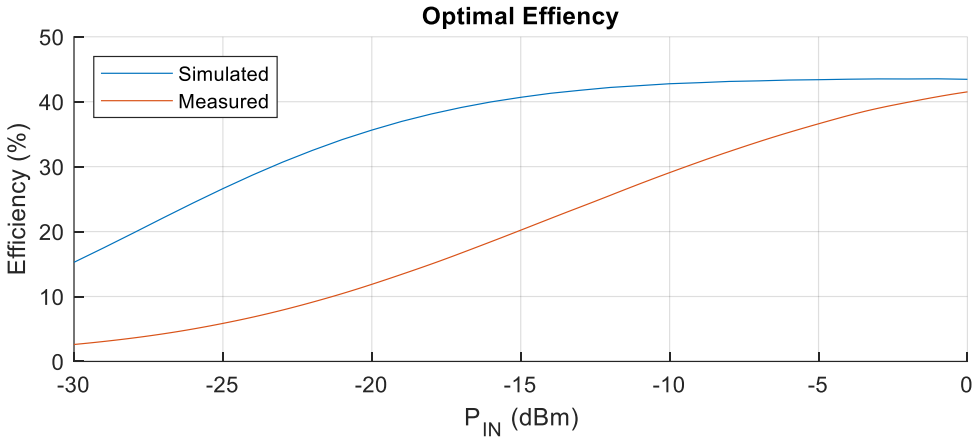

Figure 38 – Efficiency at optimized loads for the 1-stage rectifier.

The power output for the 1-stage rectifier, at optimal loads, is presented in figure 39. It can be observed that the power output of the 1-stage rectifier can reach power levels of up to 400 µW at higher power levels. Generally, in the -25 to -10 dBm power input range, the available power levels range from 2 µW to 32 µW. The simulated power output is also provided for reference. As expected, it is higher than the measured power output.

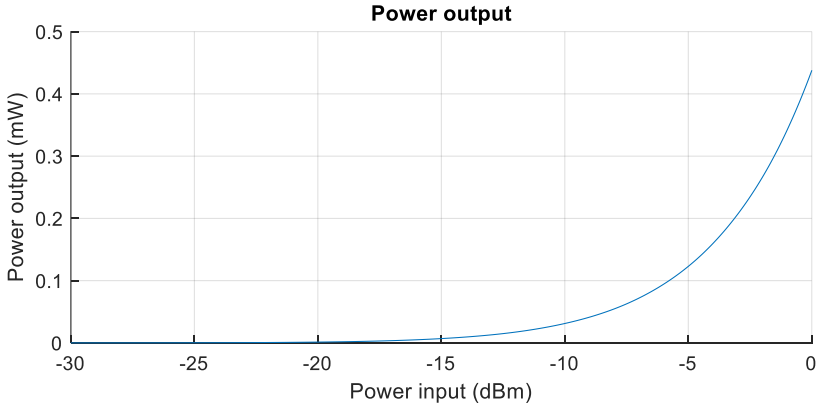

Figure 39 – Power output as a function of RF power input for the 1-stage rectifier.

Fig. 40 shows a photograph of the implemented rectifier board containing both a 4-stage and 1-stage Greinacher rectifier for data reception and powering, respectively. This board is later used in the node when assembled.

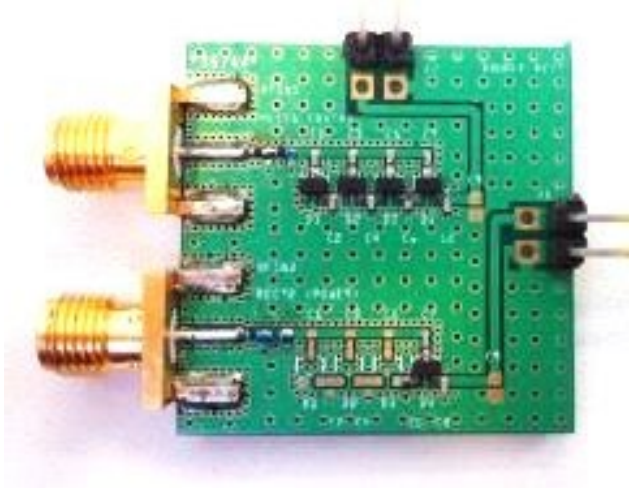

Figure 40 – Physical implementation of a dual-rectifier board. The top portion of the board houses a 4-stage rectifier, used for data reception, and is optimized for high sensitivity. The bottom portion of the board is a 1-stage recitifer, optimized for efficiency.

Section II.c – Solar Panels

In this section, the solar panels used by the node will be described and measured. Their position in the node is shown in fig. 41:

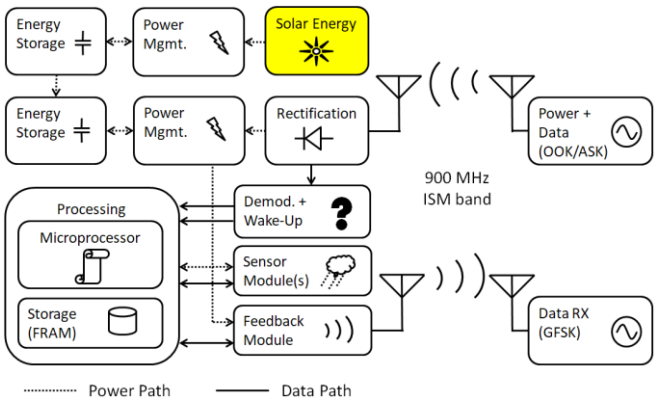

Figure 41 – Position of the solar energy module in the node.

Wireless powering is sufficient in order to power the node, and permits it to perform reliable data collection and processing. However, in order for a node to truly be useful in an IoT scenario, it must be able to transmit back data at regular intervals. Even though transmission is possible using only RF powering, the availability of energy can be an issue, and compliance with regulations of the ISM band may be problematic in order to deliver sufficient power.

Solar energy was used as an alternative source of energy to complement RF harvesting when it is possible, in order to increase the reliability of the node. It is readily available in most environments, whether they are interior or exterior. This powering option significantly increases the amount of energy available to the node, even under poor lighting conditions.

Subsection II.c.1 – Overview and Metrics

Important metrics of this module include the following, shown below in fig. 42:

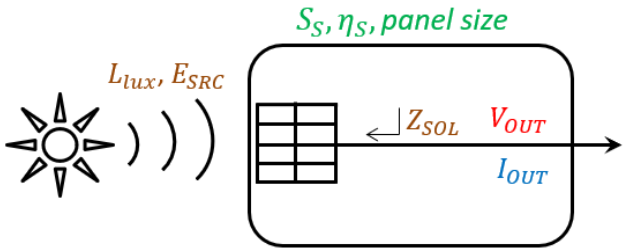

Figure 42 – Solar panel metrics.

Important metrics of this module include the following:

- The luminosity available, L_{LUX},
- The luminous efficiency of the illumination source, E_{SRC},
- The solar panel area A_{SOL} , sensitivity S_S and efficiency η_S,
- The voltage V_{SOL} and current I_{SOL} outputs,
- The output impedance of the solar panel, Z_{SOL}.

Similarly to the rectifier, the sensitivity of a solar panel is defined by:

$$S_S = V_{OUT}(L_{LUX}, E_{SRC}, size, material)$$

Likewise, the efficiency of a solar panel depends on the load applied. The power input may vary depending on the semiconductor type, size and construction material of the solar panel, as well as the luminous efficiency of the light source. It is defined by:

$$\eta_S = \frac{P_{OUT}(R_L)}{P_{IN}(L_{LUX}, E_{SRC}, size, material)} = \frac{{V_{OUT}}^2}{R_L \cdot P_{IN}(L_{LUX}, E_{SRC}, size, material)}$$

Subsection II.c.2 – Solar Panel Modelling

There are various solar cell types, made of different types of materials, with different efficiencies available, fig. 43. Generally, scientific advances over time, as well as improved manufacturing techniques, have led to increases in solar panel efficiency [53].

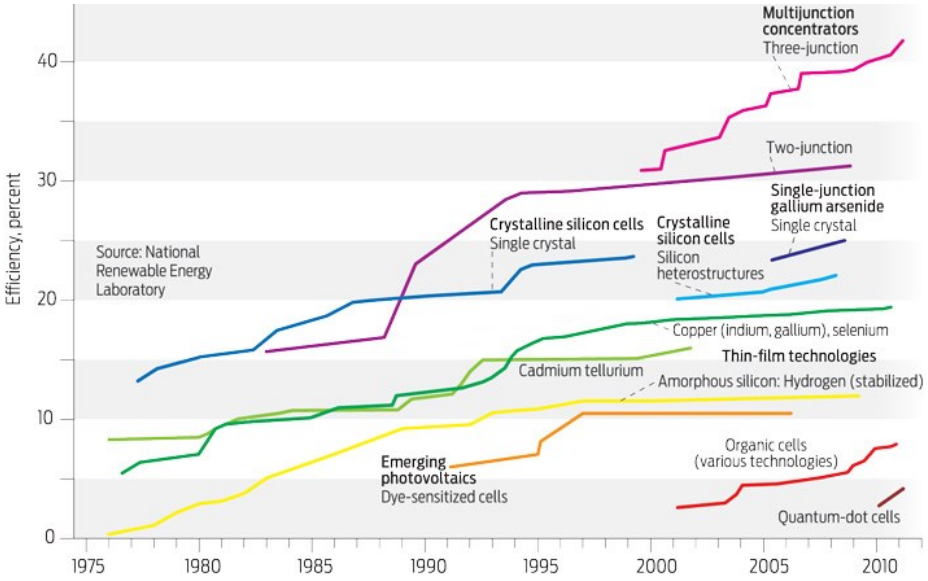

Figure 43 - Solar panel efficiency improvements over time, and by type of panel [53].

Most low-cost solar panels available at reasonable prices for consumer applications are usually monocrystalline, polycrystalline, and thin-film panels. Although monocrystalline solar panels are the most efficient type (around 20-25 %), they are also the most expensive. Thin film panels are the cheapest; however, they are also the least efficient (around 8-12 %). Polycrystalline panels are a good compromise between cost and efficiency (around 13-16 %).

The main unit used for the measure of illumination is the lux. It is generally defined as the number of lumens per unit surface area, $1\ lux = 1\ lm/m^2$. Luminosity, in lux, varies depending on the environment. Typical values for different environments are presented in table 3:

Light Source	Type (Indoor/Outdoor)	Luminosity levels (lux)
Bright Day	O	>10 000
Overcast Day	O	1 000
Supermarkets	I	500 – 750
Office	I	150 – 500
House	I	100 – 150
Dark Day	O	100
Streetlights (LED)	O	15 – 150
Sunset/Sunrise	O	10 – 20
Night (with moonlight)	O	1
Night (without moonlight)	O	< 0.1

Table 3 – Luminosity levels in different environments [54]-[56].

In order to use the lux as a measure of input power, it is necessary to define the luminous efficacy, E_{SRC}, of the illumination source. Luminous efficacy is measured in lumens per watt, and depends on the spectral components of light emitted by sources of light. Typical luminous efficacy values for different illumination sources are presented in table 4:

Light Source	Luminous efficacy (lm/W)
Tungsten Light Bulb	12.5 – 17.5
Halogen Lamp	16 – 24
Fluorescent Lamp	45 – 75
LED Lamp	80 – 100
Metal Halide Lamp	75 – 100
High-pressure Sodium Vapour Lamp	85 – 150
Low-pressure Sodium Vapour Lamp	100 – 200
Mercury Vapour Lamp	35 – 65
Direct Sunlight	90 – 150
Overcast Sunlight	60 – 120

Table 4 – Luminous efficiency for different types of light sources [56]-[58].

Subsection II.c.3 – Implementation

The solar panels used in this work are small, in order to be able to properly fit within the node's size. Two sizes of solar panels were measured. They are presented in fig. 44:

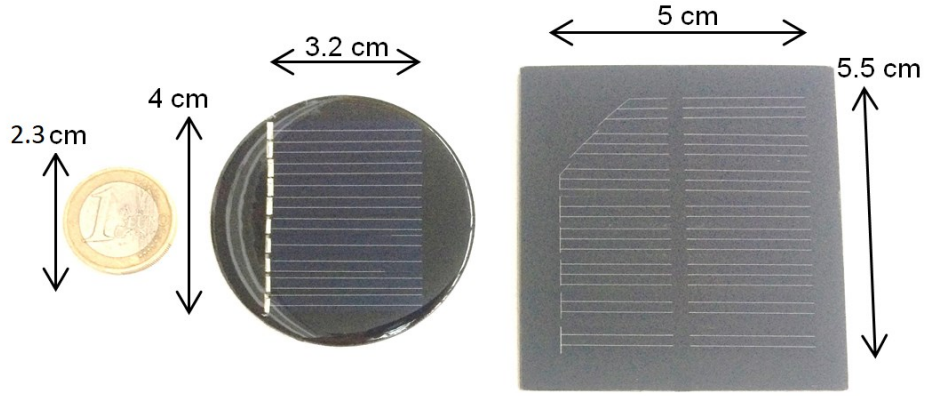

Figure 44 – Solar panels measured in this work, from right to left, the small panel, the large panel, and a 1 euro coin for scale.

Two light sources were used in this work to measure the solar panels, both yellow and white LEDs. The unloaded voltage of the solar panels is presented in fig. 45:

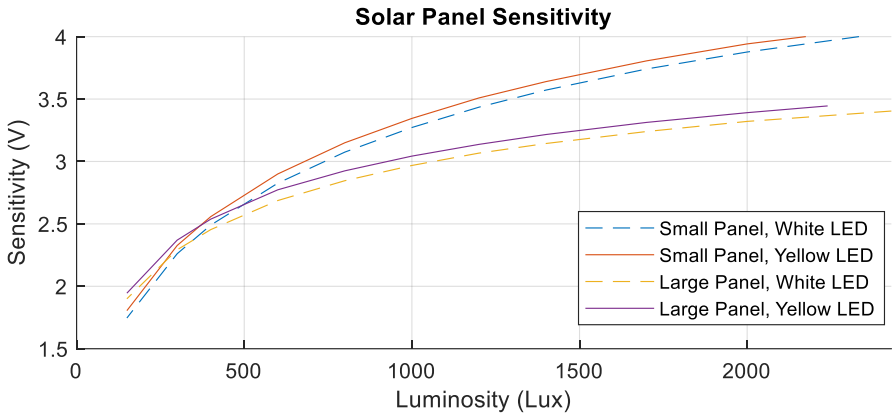

Figure 45 – Open voltage of the solar panels, depending on the light sources and their luminosity.

It can be observed that the maximum sensitivity for both the large and small solar panels are approximatively 4 and 3.5 V for luminosities above 2000 lux, respectively. Sensitivity varies little depending on the light source, with yellow LEDs proving higher voltages.

The efficiency of the solar panels can be determined by analyzing the ratio between the input power of the solar panels over the output power. The input power is determined by both luminosity levels and luminous efficiency, using the following formula:

$$P_{SOL}(L_{LUX}) = (L_{LUX} \cdot A_{SOL}) / E_{SRC}$$

The luminous efficiency for LED lamps was used, and the efficiency of the solar panels is presented in fig. 46:

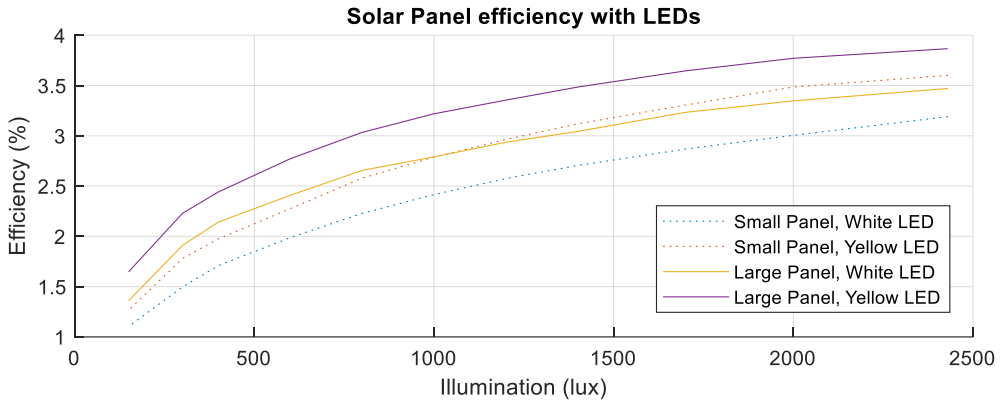

Figure 46 – Efficiencies of the solar panels, using different LED types and illumination levels

It can be observed that the efficiencies for both solar panels are in the range of 1 to 4%, increasing with the illumination levels. White LEDs tend to provide less efficient operation than their yellow counterparts. This is to be expected, as yellow LEDs are more spectrally diverse. The large discrepancy between theoretical efficiencies and the actual efficiency observed is due to the fact that aforementioned efficiencies are given for full sunlight irradiance, which are approximatively one or two orders of magnitude higher than LED illumination.

Fig. 47 shows the power output of the solar panels as a function of luminosity:

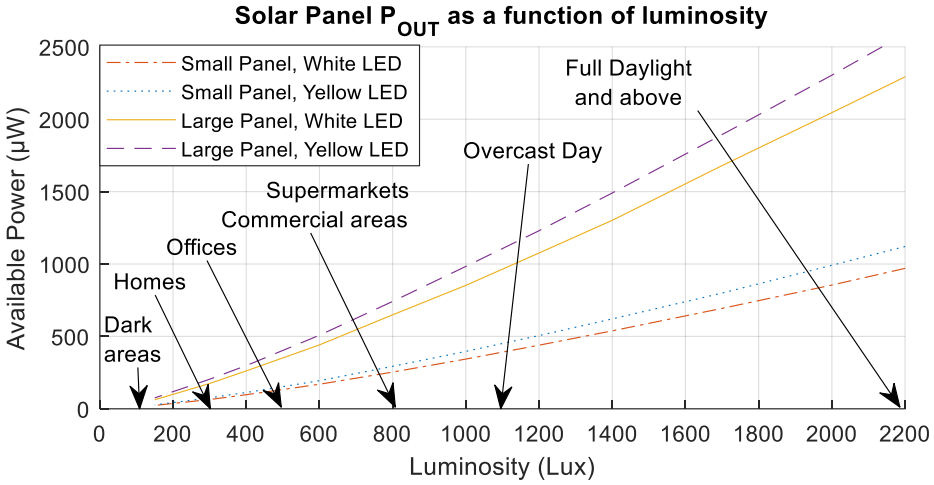

Figure 47 – Power output of the solar panels, using different LED types and illumination levels. Reference illumination levels are provided.

The maximum output DC power (available power) is between 500μW and 1.5mW for the large panel, and between 250μW and 600μW for the small panel. In an office with only artificial light (L_{LUX} < 500 lux) the large panel still yields more than 50μW, with a sensitivity of 2V. As stated above, yellow LEDs provide a larger open voltage, and a higher output power, as they are more spectrally rich than white LEDs [59]; however, the difference is not significant. The available power output of solar energy, however, still remains higher than RF powering, even at these low efficiencies. For the purposes of this work, the large solar panel will be used by the node.

Section II.d – Energy Storage

In this section, the storage elements used by the node will be described and measured. Their position in the node is shown in fig. 48:

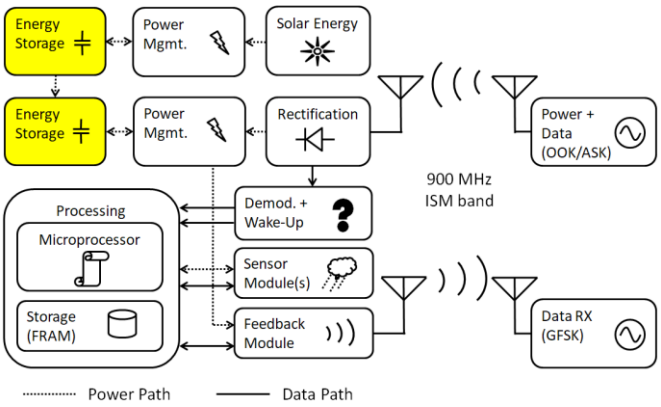

Figure 48 – Position of the energy storage modules in the node.

Of importance for the node is how energy is stored for later use by the system. Current average power densities versus energy densities for different energy storage methods are shown in fig. 49:

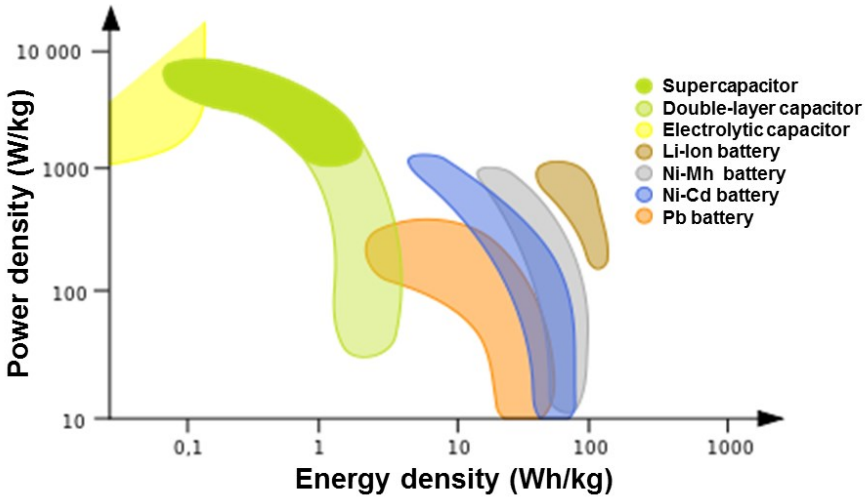

Figure 49 – Average power densities versus energy densities for current storage devices [60].

Currently, two main methods are used, depending on the power consumption profile. For heavy-duty devices (several milliwatts to several hundreds of milliwatts), batteries are commonly used for as their energy density makes them suited to the amount of power used []. However, their performance degrades over time, due to battery chemistry. Generally, for lithium polymer and lithium-ion batteries, the number of possible charge and discharges

possible range from approximatively 500 to 5000 cycles, before capacity degrades significantly, at which point they require replacement [61], [62]. Their low power density also has the disadvantage of making charge times relatively long compared to capacitor-based storage elements.

Capacitors, on the other hand, have lower energy density, but have a higher number of charge cycles available to them before failure, by a factor of two to three orders of magnitude [63]. This makes their use in low maintenance micro or nano-power nodes important. Although recent advances have permitted the development of supercapacitors, with higher energy densities, they currently are about two orders of magnitude lower than conventional or rechargeable batteries. However, charge times for capacitor-based storage elements can be lengthy, and leakage current remains problematic for supercapacitor-based storage devices.

For this work, capacitor and supercapacitor-based storage elements were selected in order to store energy, as they can be charged via the RF and solar powering methods selected, and they are low maintenance devices.

Subsection II.d.1 – Overview and Metrics

A summary of important parameters used for the selection of capacitor-based storage devices presented in fig. 50:

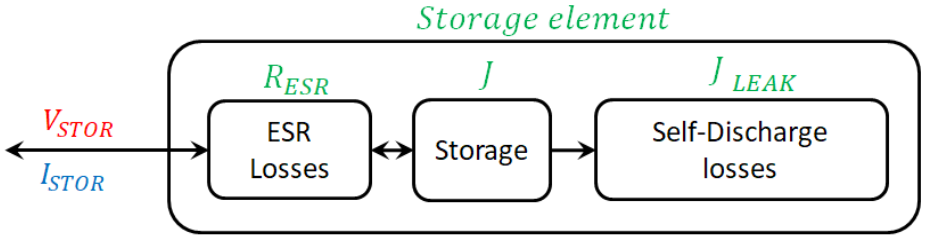

Figure 50 – Capacitor-based storage metrics.

Important metrics of this module include the following:

- For losses: a low equivalent series resistance (ESR), R_{ESR}, in order to limit Joule losses when the storage element is solicited, and J_{LEAK}, the energy losses over time due to the self-discharge of the storage element,
- For the storage element itself: its energy capacity, J, in joules, in order to determine the autonomy and feasibility of storing energy in the node,
- For the overall subsystem: The selection of an appropriate storage element.

Subsection II.d.3 – Modelling of Capacitors and Supercapacitors

Typical storage capacities for ceramic capacitors are in the range of picofarads to several hundreds of microfarads. Supercapacitors, on the other hand, are generally in the range of millifarads up to several hundreds of farads. Generally, ceramic capacitors are available at higher voltage ratings, whereas supercapacitors have lower ones, due to different underlying dielectric design.

Taking into account the power levels available for harvesting, a single supercapacitor was used in order to store solar energy, and ceramic capacitors were used for the storage of RF energy, to make energy storage size reflect the order of magnitude of power harvested. For this work, AMK432BJ477MM-T ceramic capacitors and an AVX supercapacitor were chosen for RF energy storage and solar energy storage, respectively [64], [65]. The characteristics provided by the manufacturers of the devices are presented in table 5:

Characteristic	Supercapacitor	Ceramic Capacitor
Higher tolerance (+ %)	100	10
Lower Tolerance (- %)	0	10
Capacitance (µF)	470 000	470
ESR (mΩ)	380	10
Rating (V)	5	4
Leakage Resistance (µF*MΩ)	-	> 10
Leakage Current (nA)	>5 000	-
Peak Current (mA)	800	-

Table 5 – Capacitor and supercapacitor characteristics.

The theoretical energy, J, that can be stored by a capacitor, is related to the voltage V to which is is charged, and is represented by the following formula:

$$J = \frac{C \cdot V^2}{2}$$

For the supercapacitor and capacitor, the maximum energy that can be stored at 4 V is $J_{SC} = 3.76\,J$ and $J_C = 3.76\,mJ$, respectively.

The ceramic capacitors are disadvantaged in the sense that their capacitance varies with the voltage present on them. These characteristics are provided by the manufacturer. As a result of this metric, the actual energy that can be stored is less than can be provided using only the nominal capacitance as reference. This energy storage derating is shown in fig. 51:

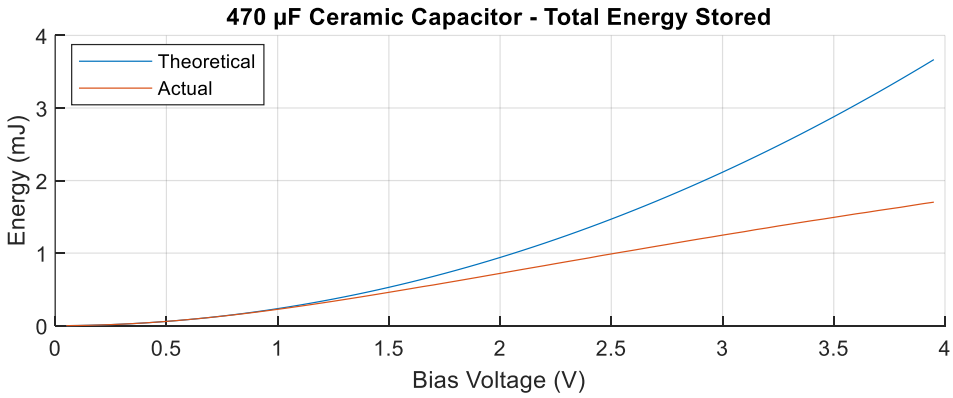

Figure 51 – Actual energy that can be stored by the ceramic capacitor.

Based on manufacturer data, it can be observed that the effective energy storage is halved, from the original 3.76 mJ, to approximatively 1.7 mJ. Supercapacitors, generally, do not have reduced capacitance at higher bias voltages [66].

Subsection II.d.4 – Implementation

Figure 52 shows a photograph of supercapacitor, and one of the ceramic capacitor arrays used in this work. The ceramic capacitor arrays are soldered to a circuit board, and their modular nature permits a varying number of ceramic capacitors to be implemented in the node. It should be noted that the association of ceramic capacitors in parallel increases their leakage resistance.

Figure 52 – Left to right: Supercapacitor and 8x ceramic capacitor array.

Section II.e – Power Management

In this section, the power management modules used in the node will be described and measured. Their position in the node is shown in fig. 53:

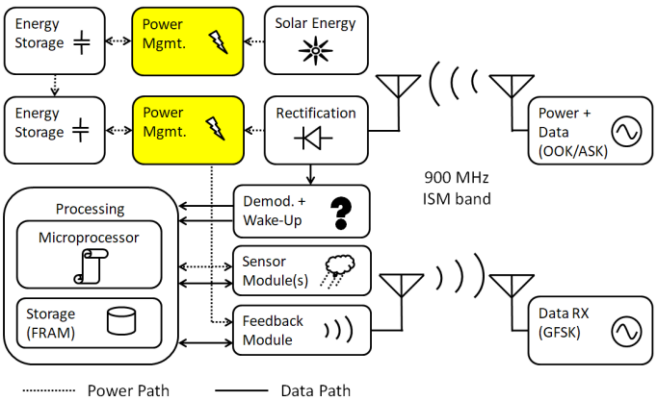

Figure 53 – Position of the power management modules in the node.

As seen in the previous sections, rectifiers deliver a DC output voltage that ranges approximatively from 10 mV to 1 V when far or close to an RF power source, respectively. This is not sufficient in order to power most COTS devices, for which the nominal operating voltage is usually between 1.8 V to 3.3 V. Therefore, the use of a boost converter must be considered in order to raise the voltage levels present at the rectifier in order to power the node. The addition of solar powered energy also requires adding another power management device, as the configuration to harvest energy is different for both solar and RF power.

Furthermore, as capacitive elements will be used for energy storage, they will be charged to their maximum extent possible using the boost converter. In order to use the energy stored in these elements, a buck converter will also be required to continuously supply the node with its nominal operating voltage, lest it use more power than necessary at higher voltages.

Finally, power management ICs also need to be programmed in several manners in order to control power storage, Maximum Power Point Transfer (MPPT), and need to indicate their status to the microcontroller powering the node in order for it to operate within nominal parameters.

Subsection II.e.1 – Overview and Metrics

A summary of important metrics used for the selection of a power management IC are presented in fig. 54:

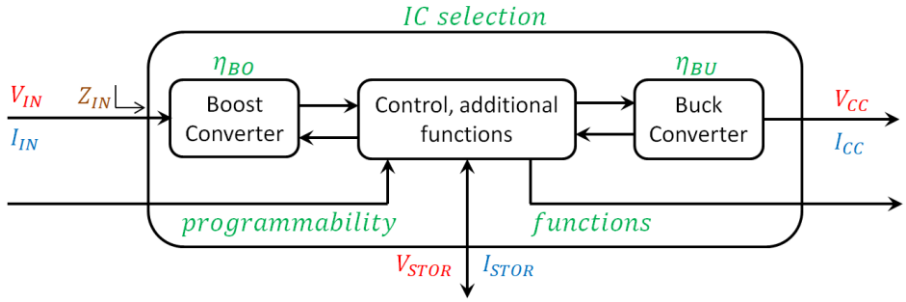

Figure 54 – Power management metrics.

Important metrics of this module include the following:

- For the boost converter : efficiency η_{BO}, and the impedance presented to Z_{IN},
- For the buck converter: efficiency η_{BU},
- The programmability of the power management unit, and the ability of the unit to furnish information to the system,
- For the overall subsystem: The selection of an IC capable of efficiently performing the functions above.

Subsection II.e.2 – Buck/Boost Converter

Buck and boost converters are switching DC to DC power converters, which, respectively, step down or step up a voltage at their inputs. They are used in order to furnish the voltages required to different subsystems, which may not always be identical. The switching nature of these circuits minimizes power loss, though this comes at increased noise levels in the power supply rails.

For the purposes of the subsection, the following terms will be defined:

- T, the switching period of the converters,
- D, the duty cycle of the switching period,
- R_L, the value presented by the load.
- V_{IN} and V_{OUT} the voltage present on the source and load, respectively,
- I_{IN} and I_{OUT}, the current present at the source and load, respectively.

The principle of operation of a boost converter, fig. 55, is that of a controlled charge and discharge of its main inductor, L_{BO}, using a switch S_{BO} and a diode D_{BO}, in order to charge the capacitor C_{BO} and load R_L to a voltage higher than that of the input. When the switch S_{BO} is activated, the inductor L_{BO} is shorted to ground, and as a result, the current through the inductor will increase, as its stores energy in its magnetic field. When the switch S_{BO} is opened, the energy stored in the magnetic field of L_{BO} is transferred into the capacitor and load, C_{BO} and R_L, through the diode D_{BO}. As the inductor is now in series with the source, the voltage provided to the load will be higher than the input voltage.

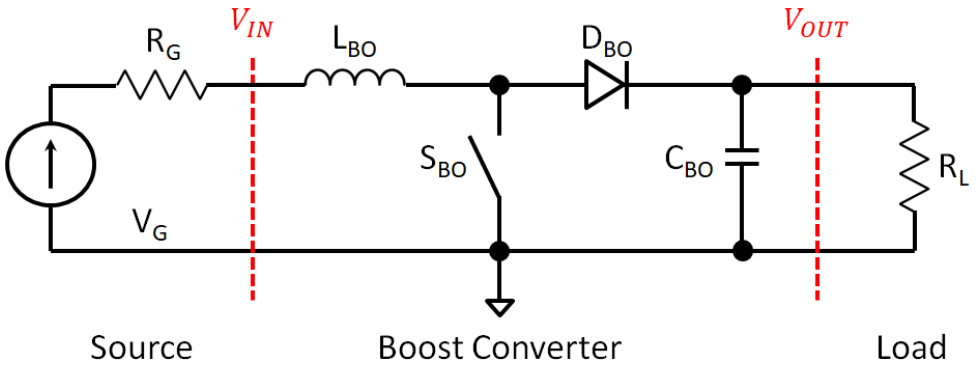

Figure 55 – Boost converter topology.

There are two modes of operation for the boost converter: continuous and discontinuous mode. In continuous mode, then the current flowing through the inductor is assumed to never be zero, and the output voltage as a function of the input voltage can be expressed by the following equation, where D is the duty cycle of the switching time T:

$$V_{OUT,CONT} = \frac{V_{IN}}{1 - D}$$

Under certain conditions, however, which generally happens under light loads, or very slow switching frequencies, the value of the current flowing through the inductor when the switch is off can reach zero, which changes the relationship of the output voltage:

$$V_{OUT,DISCONT} = V_{IN}\left(1 + \frac{V_{IN} \cdot D^2 \cdot T}{2 \cdot L_{BO} \cdot I_{OUT}}\right)$$

Figure 56 illustrates the relationship between the switching duty cycle D, and the normalized representation of the output voltage and current of the boost converter, with both modes of operation.

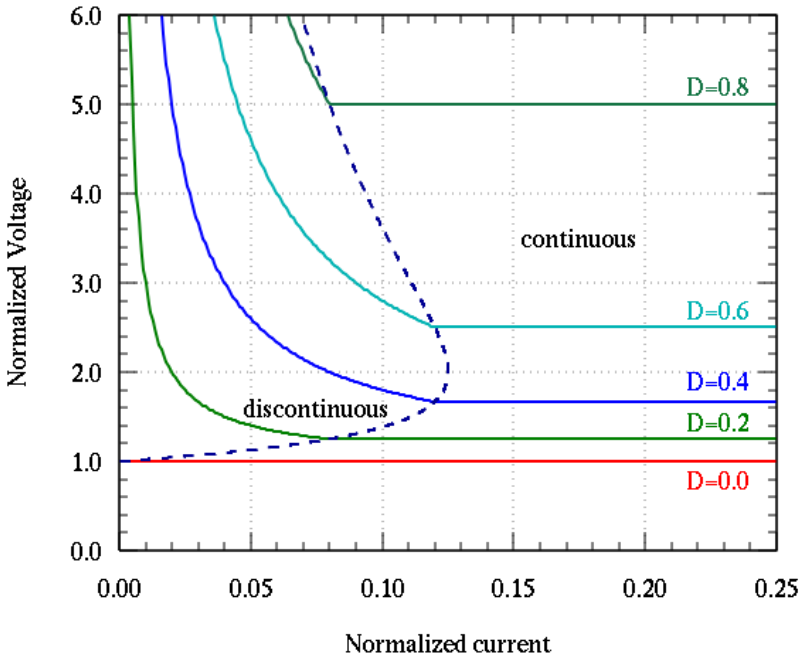

Figure 56 – Effect of duty cycle on normalized output voltage and current in both modes of operation for the boost converter.

The normalized voltage, V_N, and the normalized current, I_N, for the boost converter are defined as follows:

$$V_N = \frac{V_{OUT}}{V_{IN}} \qquad\qquad I_N = \frac{L}{T \cdot V_{IN}} I_{OUT}$$

These two parameters represent the ratio of the input to output voltage of the converter, and the ratio of the current that can be conducted by the converter to the amount of current that is present on the output.

Similarly, the principle of operation of a buck converter, fig. 57, is that of a controlled charge and discharge of its main inductor, L_{BU}, using a switch S_{BU} and a diode D_{BU}, in order to charge the capacitor C_{BU} and load R_L to a voltage lower than that of the input. When the switch S_{BU} is turned on, the diode D_{BU} is reverse-biased, and the current flows through the inductor L_{BU}, which stores energy in its magnetic field. As S_{BU} is turned off, then the input voltage is removed from the rest of the circuit, and D_{BU} becomes forward-conducting. L_{BU} then becomes a constant current source, discharging into the capacitor and load, C_{BU} and R_L.

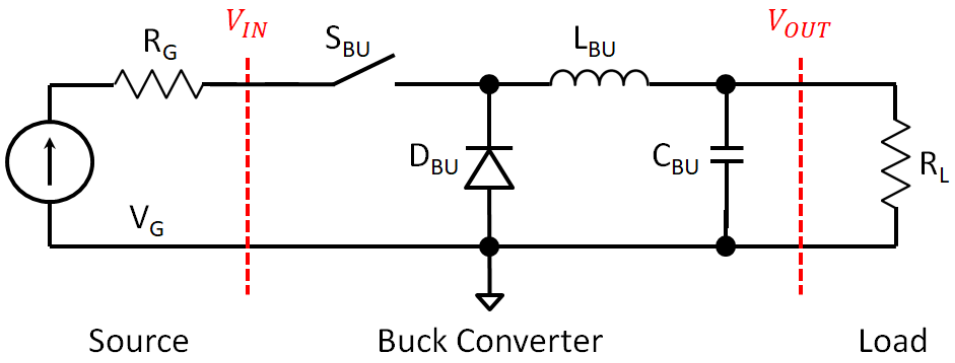

Figure 57 – Buck converter topology.

Fig. 58 illustrates the relationship between the switching duty cycle *D*, and the normalized representation of the output voltage and current of the boost converter, with both modes of operation.

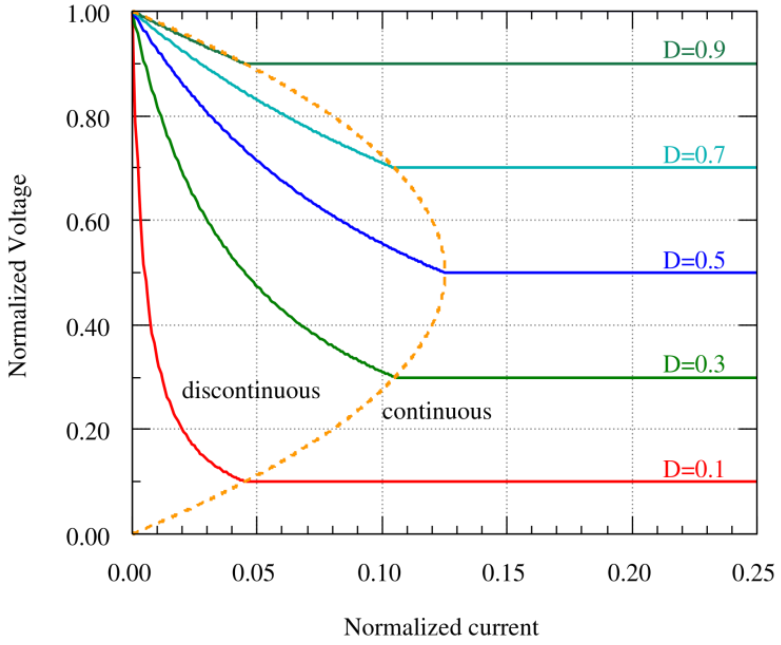

Figure 58 – Effect of duty cycle on normalized output voltage and current in both modes of operation for the buck converter.

There are two modes of operation for the buck converter as well: continuous and discontinuous mode. In continuous mode, then the current flowing through the inductor is assumed to never be zero, and the output voltage as a function of the input voltage can be expressed by the following equation, where *D* is the duty cycle of the switching time *T*:

$$V_{OUT,CONT} = D \cdot V_{IN}$$

Under certain conditions, however, which generally happens under light loads, or very slow switching frequencies, the value of the current flowing through the inductor when the switch is off can reach zero, which changes the relationship of the output voltage:

$$V_{OUT,DISCONT} = V_{IN} \frac{1}{\frac{2 \cdot L_{BU} \cdot I_{OUT}}{V_{IN} \cdot D^2 \cdot T} + 1}$$

For both converters, although the voltage output depends only on the duty cycle when they operate in continuous mode, in discontinuous mode, voltage output becomes heavily dependent on the contextual (current load) and technical (inductor size, duty cycle) parameters of the design. Furthermore, the equations presented above assume ideal components are present in the circuit, when in practice, they will not be. However, even with non-ideal components, the practical performance of buck and boost converters can be higher than 80 or 90%.

Subsection II.e.3 – MPPT

In order to properly extract a maximum amount of power from an energy source, the impedance of the input of the power management module must match the impedance of the former. Maximum Power Point Tracking (MPPT) is a technique which is used in order to solve this problem.

Energy sources, depending on load and origin of source energy, have differing current-voltage (I-V) characteristics. As the external environment is not inherently stable, these characteristics may change, thus modifying the I-V curve of the device. In order to accommodate for this, an IC with MPPT implemented must be selected, in order to extract energy in the most efficient way possible from rectifiers, notably, due to the low amount of energy they generate. This is achieved by presenting a variable load to the source, by varying the switching characteristics of a buck or boost converter, that will convert the energy received.

Fig. 59 is a graphical representation of MPPT, wherein the variable load of the device collecting energy, Z_{IN}, is represented as the load line applied to the instantaneous I-V curve of source. The power available can therefore be described as $P_{IN} = V_{IN} \cdot I_{IN}$. The short circuit current, and open voltage parameters of the device are illustrated as I_O and V_O, respectively.

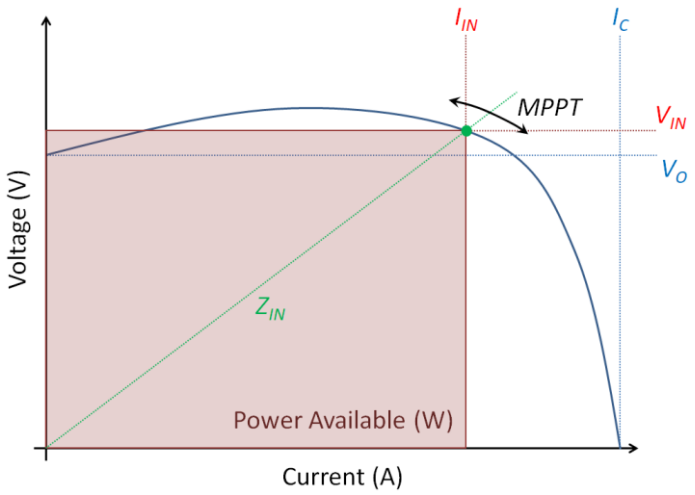

Figure 59 – Illustration of maximum Power Point Tracking (MPPT).

Subsection II.e.4 – Implementation

The bq25570 and bq25504 Power Harvesting ICs were chosen for power management, as they provide MPPT, and a boost converter at the power harvesting inputs [67], [68]. The bq25570 provides an additional buck converter connected to the storage element, which can be used to lower the voltage present at the power storage element in order to provide a preset voltage to the digital section of the node, to maximize power consumption efficiency. They both have a low quiescent, of 330 nA and 470 nA for the bq25504 and bq25570, respectively, which remains constant independently of the storage elements' voltages.

The bq25504 and bq25570 have several different modes of operation. If the main storage element ($C_{SUPERCAP}$ and $C_{CERAMIC}$, respectively) is depleted, it needs to be charged to a certain threshold (V_{CHGEN}) before operation of the MPPT and the bq25570's boost converter, through the use of a low efficiency (approximatively 5%) "cold start" charge-pump. The storage element is then charged to an acceptable voltage level, in order to allow the main parts of the IC to operate. The bq25504 and bq25570's more efficient boost converters begin functioning once the storage element reaches a voltage of 1.9 V.

In order to avoid rapidly regressing into a cold start state, once the desired voltage is reached (especially due to the activation of the load), a storage element threshold indicator (with hysteresis), V_{BATOK}, is provided by the IC, and is used in this work in order to turn on or off the supply to the digital section of the node, if power is scarce. The minimum storage voltage required to power on the system is 2.5 V, and the hysteresis shutoff is defined at 2.2

V. The values of the resistors to program the device are chosen using [69]. Schematics of the implementation are shown in fig. 60:

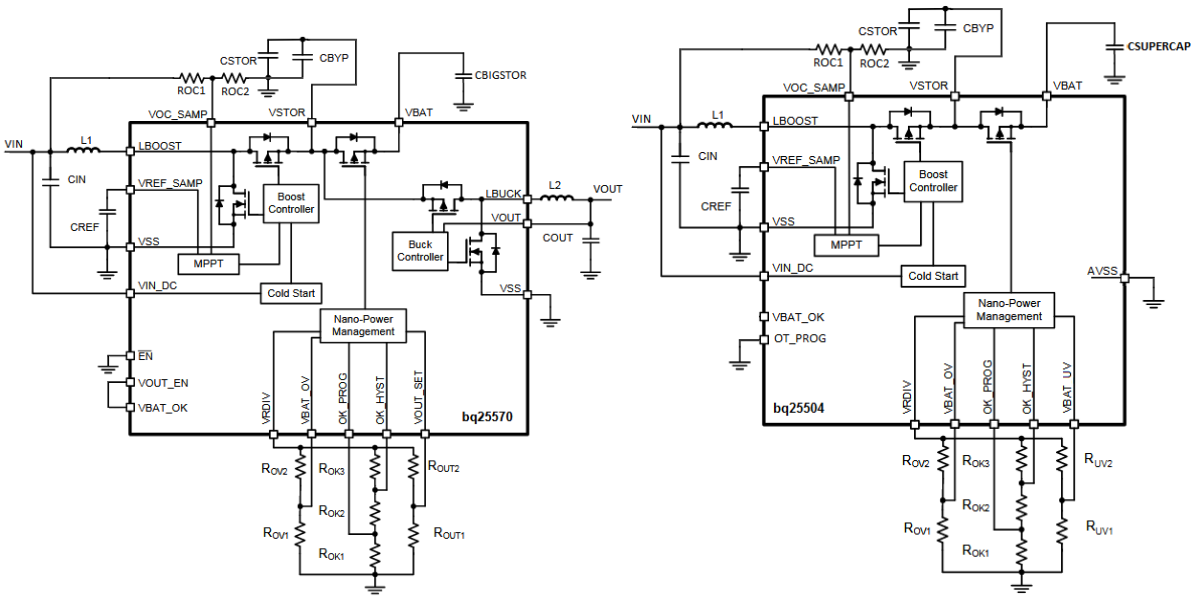

Figure 60 – Implementation of the harvesters, (a) the bq25570 used for the solar harvester, and (b) the bq25504 user for the RF power harvester. Adapted from [67], [68].

In order to perform MPPT, the bq25504 and the bq25570 periodically sample the sensitivity, *S*, of the solar panel or the 1-stage rectifier through their respective R_{OC1}/R_{OC2} divider bridges, and applies a load according to the voltage present between R_{OC1} and R_{OC2} (S_{MPPT}).

For the rectifier, which uses the bq25704, the optimal loads from -30 dBm to 0 dBm were determined for MPPT, and from them, the optimum voltage level that should be delivered through the voltage divider. This is presented as the ratio of S_{MPPT} / S in fig. 61.

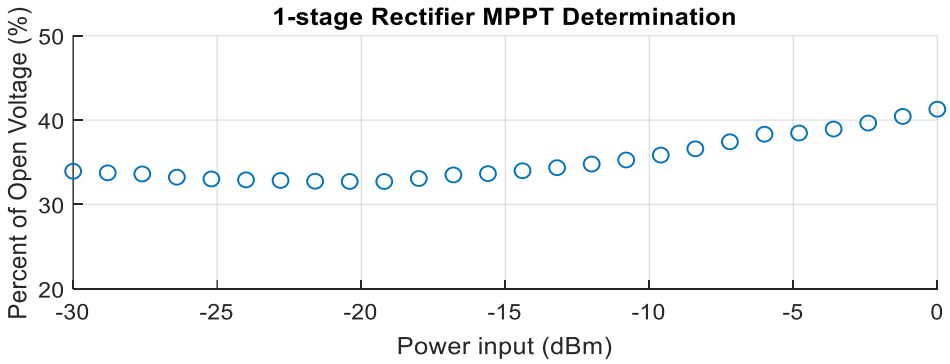

Figure 61 – Determination of MPPT configuration for the 1-stage rectifier.

It can be seen that a value of around 35% presents optimal power transfer, especially at lower input power, therefore R_{OC1} and R_{OC2} were set accordingly.

For the solar panel, which uses the bq25504, the optimal loads from 150 to 2000 lux were determined for MPPT, and from them, the optimum voltage level that should be delivered through the voltage divider. This is presented as the ratio of S_{MPPT}/S in fig. 62.

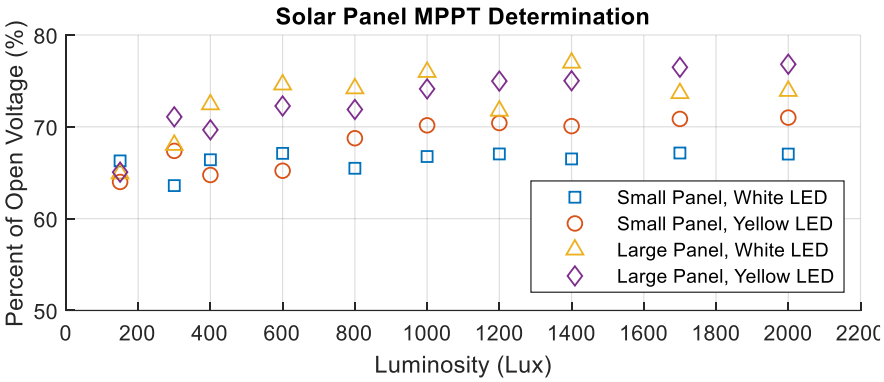

Figure 62 – Determination of MPPT configuration for the solar panel.

It can be seen that values of around 70% and 65% present an optimal power transfer, for the large and small solar panels, respectively, especially at lower luminosity levels. As the large solar panel will be used in this work, R_{OC1} and R_{OC2} were set accordingly.

With each powering method having its own power harvester, it is necessary to enable the transfer of energy from one to another. As the boost converter on the bq25570 is used to generate the voltage required by the node, the solar power unit must be able to transfer energy to the rectifier power unit. This was done through the use of a BAT17-04 Schottky diode, which was introduced between the supercapacitor serving as a storage element for the bq25504, and the ceramic capacitor array serving as a storage element for the bq25570 [70]. This modification is illustrated in fig. 63:

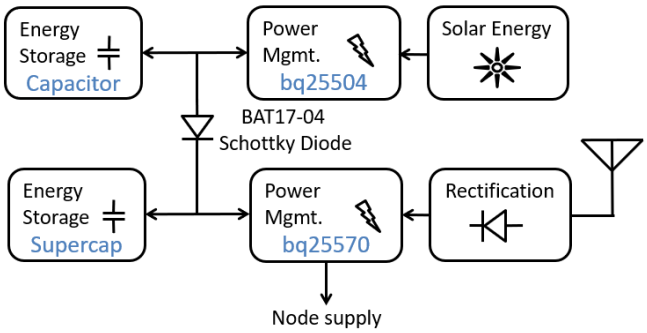

Figure 63 – Position of the BAT17-04 Schottky diode relative to both power harvesting circuits.

This is the optimal non-active method to keep the node powered, as it permits the low-leakage, ceramic capacitor to always contain energy. Should RF powering not be available, the supercapacitor present on the solar harvesting circuit discharges into the RF harvesting ceramic capacitor array. Inversely, should RF power be available, then the bq25570 will not consume any energy, as the diode prevents energy in the ceramic capacitor array to flow back into the supercapacitor. This, however, does come at a cost, as some energy is lost through the diode threshold voltage. However, as this is taken from solar energy stored in the supercapacitor, the impact is minimal.

The buck converter of the bq25570 can be configured to output a voltage below the current voltage present on the ceramic capacitor array. 1.8 V was chosen as the output voltage, as this is the minimal voltage required in order to power the digital modules of the node. The efficiency of the buck converter was measured, for a storage element voltage of 4 V, and is presented in fig. 64:

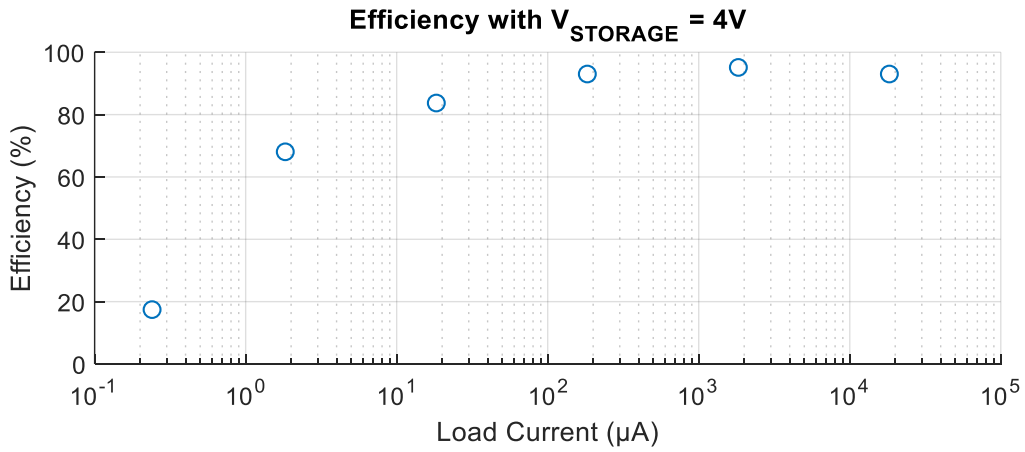

Figure 64 – Efficiency of the buck converter of the bq25570.

It can be observed that, the lower the load current, the lower the efficiency of the buck converter. This will have the disadvantage of artificially increasing the power consumption of the node in sleep mode, where it only uses several hundreds of nanoamperes in order to function. However, at higher consumption levels, which would be in effect when the node is operating, the efficiency is usually above 80%.

The power management modules are also capable of being entirely shut off through the use of an enable pin, which has been grounded in this work, but could be used in a more complete system to modulate between powering sources whilst minimizing power consumption. The module also provides a “battery good” indicated pin, which is connected to

the functionality module of the node, where it forces itself into sleep mode should the battery be discharged below a certain level.

Figure 65 shows a photograph of the implemented power management boards for RF and solar power harvesting.

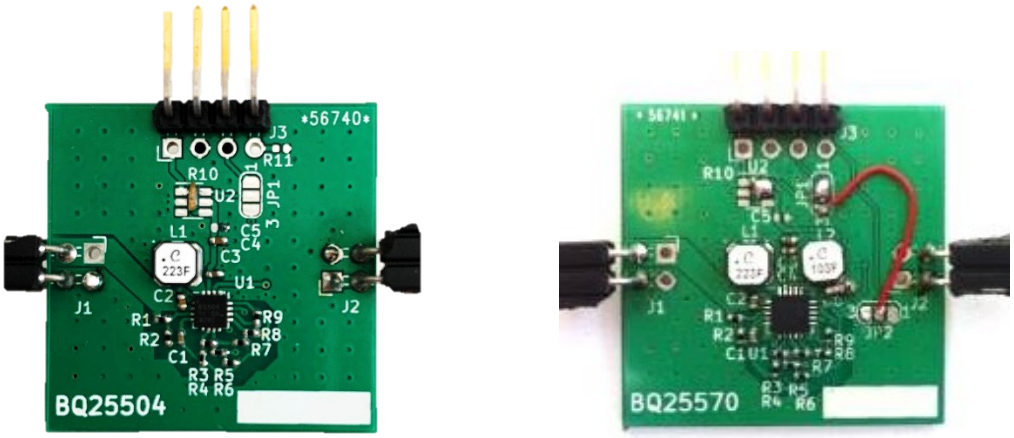

(a) (b)

Figure 65 – Physical implementation of the power management modules. (a) shows the bq25504 IC used for the harvesting of RF energy, and (b) shows the bs25570 IC used for the harvesting of solar energy.

Section II.f – Radio Demodulator

In this section, the data reception module used in the node will be described and measured. Its position in the node is shown in figure 66:

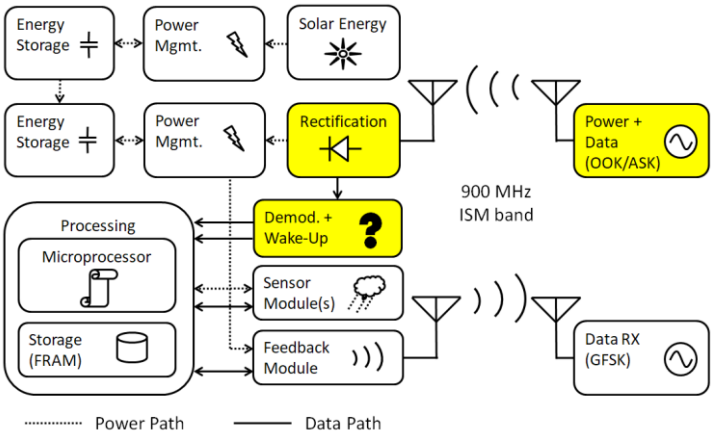

Figure 66 – Position of the data reception module in the node.

The node must be able to receive commands in order to perform intelligent functions or to give it further instructions. Due to the low power requirements of the node, an appropriate modulation method must be selected and implemented, along with an appropriate circuit.

Subsection II.f.1 – Modulation Selection

The modulations chosen in order to send instructions to the node are ASK and OOK modulation, both digital in nature. Analog modulation was not considered, as firstly, it would be distorted since the voltage output of rectifier circuits is exponential. Additionally, the decoding of analog signals would come at the cost of higher power consumption, which is not desired for this work.

Modulation schemes using the phase or the frequency in an RF signal in order to transmit data were also disregarded, for several reasons. Slow changes in phase information present in a modulated signal over an RF carrier are destroyed during the rectification process. Frequency based modulation was also considered, however, this would require additional COTS components with heavy power consumption, beyond the levels of magnitude desired for the operation of the node in normal scenarios. Furthermore, even though the sensitivity of the rectifiers changes depending on the frequency of the RF signal

received, the change in rectifier output voltage for low-bandwidth frequency modulation is too small for practical use [71]. This leaves only digital amplitude modulation for use in order to receive data.

As the implementation of data demodulator must be designed to use the least amount of power, a data slicer and a single comparator will be used in order to decode data and furnish a normalized signal to the microcontroller of the node. This eliminates any digital modulation schemes using multiple amplitudes.

Subsection II.f.2 – Metrics

A summary of important parameters used for the design of the data reception module are presented in fig. 67:

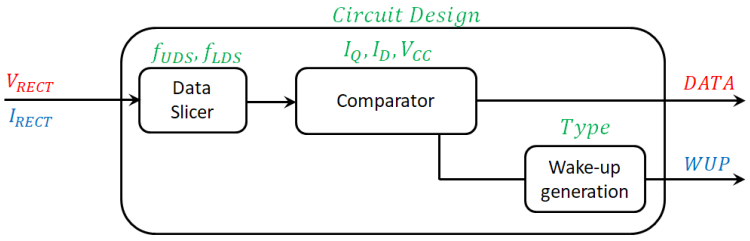

Figure 67 – Data reception metrics.

Important metrics of this module include the following:

- For the data slicer : upper filter frequency f_{UDS}, and lower filter frequency f_{LDS}, used to receive signals from the rectifier within a certain frequency range,
- For the comparator: quiescent current I_Q, dynamic current I_D, and power supply voltage V_{CC},
- For the wake-up generator: the implementation type T, able to solicit a microcontroller only when data for the node is received,
- For the overall system: The selection of a design capable of efficiently performing the functions above.

Subsection II.f.3 – Encoding

Amplitude modulated information, when transported over an RF carrier, must be able to satisfy two criteria: the recovery of the clock (baudrate), in order to sample data correctly

(known as synchronization), and turn the modulation into a stream of bits comprehensible by the software or hardware decoding the message.

Manchester encoding is selected for the encoding of messages in order to ensure that the recovery of the transmitted data does not require the DC component of the transmitted signal, as this information is lost when transmitted over RF. The generation of a Manchester encoded signal is done as a derivative of binary phase shift keying (BPSK), wherein data desired to be transmitted controls the phase of a square clock signal. The nature of this modulation ensures that there are constant bit transitions, avoiding issues with a stagnant DC component. Two versions of Manchester encoding exist, shown in fig. 68, illustrating the transitions as a function of data input and the clock. These two variations are essentially a variation on the polarity of the data transmitted.

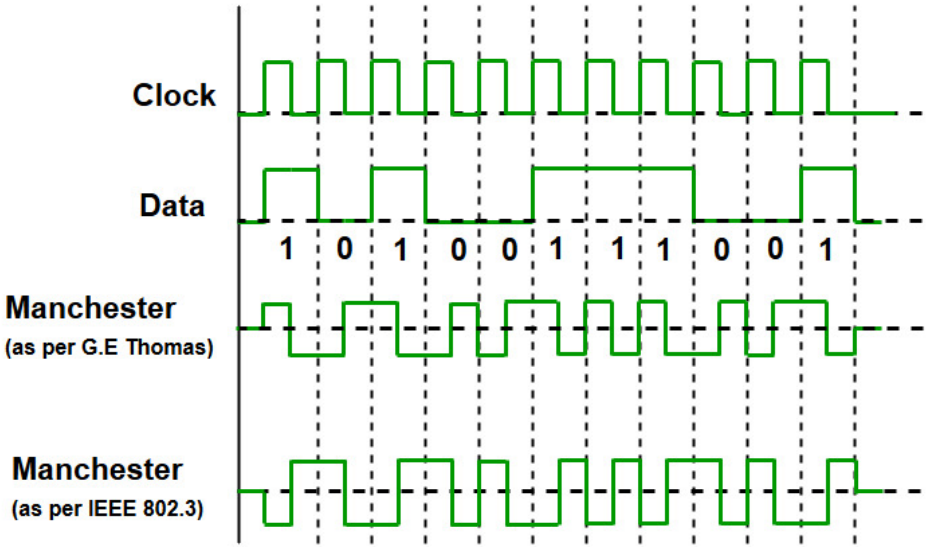

Figure 68 – Manchester encoding, with the two different polairty schemes.

However, as the receiver in this node is incapable of receiving phase modulated data, the resulting signal, instead of being transmitted through an RF carrier as phase modulation, will be modulated as amplitude-modulated data. This is necessary, as in order to receive data from the rectifiers, the amplitude of the carrier signal must vary for the data demodulator to generate an image of the received data.

The data to be transmitted to the node is encapsulated into a specific frame format, in order to permit reception of data. The frame format, illustrated in fig. 69, is composed of three major components:

- A synchronization/wake-up preamble, in order for the data slicer to settle properly on a mid-level voltage of the RF transitions, in order to appropriately be able to detect if the incoming data is at a high or low transition, *s* bits long,
- A stop bit to the preamble, in order to determine the end of the synchronization preamble without using power-consuming techniques, which is one bit in size,
- The message that is to be processed by the node, which is *m* bits long. The message will contain the instructions for the node to process.

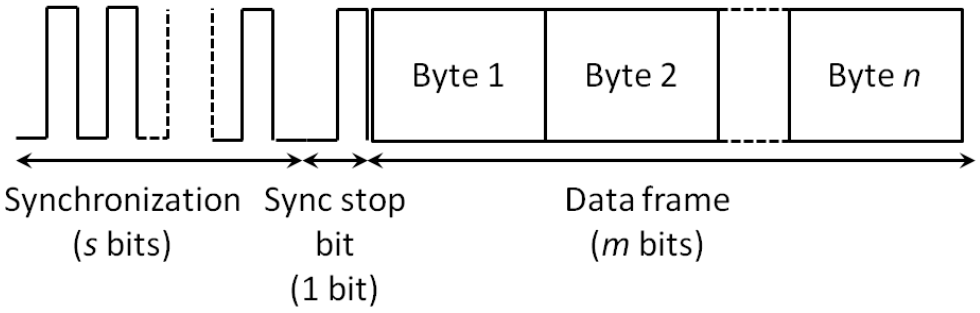

Figure 69 – Data frame format for the node.

Subsection II.f.4 – Implementation

In order to minimize power consumption, the node is kept in a "sleep" status when not solicited. This required the use of an external wake-up signal in order to indicate that data is inbound, in order to activate the node so it may process the message. The architecture used for the decoding of amplitude-modulated Manchester data was originally done using a combined data-slicer and comparator circuit. Initial iterations of the demodulator circuit were architecturally simple, consisting of a simple RC data slicer and a half-wave rectifier as the wake-up generator.

In order to improve the reliability of this circuit, a modified version of it was elaborated, on the basis that low-frequency interference was a significant source of errors and false wake-ups. This was generally due to varying RF power levels as the environment changed during testing scenarios (e.g., objects of people moving in the vicinity of the rectifier). The modifications make it robust against low-frequency, brutal changes in power levels, or against external interference from other communications in the same band, which may be interpreted by the comparator as data.

The improved comparator circuit is presented in fig. 70. The output of the comparator is a normalized representation of received binary data to V_{CC} (1.8 V). This is used in two ways: to generate a wake-up signal (WUP); and also give data to the microcontroller (DATA) to be processed when the wake-up signal is generated.

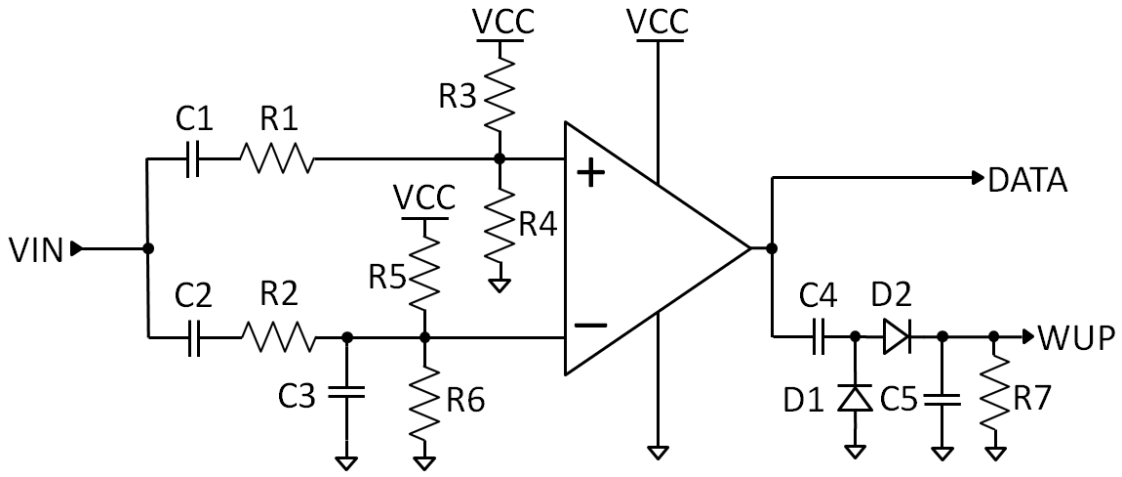

Figure 70 – Schematic of the final comparator/data slicer ciruit, with low-frequency filtering.

C_1, R_1, R_3 and R_4 form a high-pass filter on the positive input of the comparator. C_2, R_2, C_3, R_4 and R_5 form a band-pass filter on the negative input of the comparator. The band-pass filter is also implemented as the data slicer, which will average the amplitude-modulated, Manchester encoded data that has been extracted from the RF carrier through the rectifier module.

Furthermore, R_3, R_4, R_5 and R_6 are used to polarize the otherwise floating inputs of the comparator. In order to further improve reliability, albeit at the cost of slightly decreased sensitivity, the positive input of the capacitor is polarized slightly higher than the negative input. Using this configuration, the averaged amplitude of the incoming signal will be used to discriminate between the high and low amplitudes provided by the modulation.

The wake-up signal is generated through C_4, D_1, D_2, C_5 and R_7. These form a full-wave rectifier which charges as the synchronization preamble is received, and a wake-up signal is generated. Resistor R_7 is used to configure the discharge speed of the wake-up signal, in order to be able to configure the delay between messages. C_4 and C_5 can be used to configure the charge speed of the wake-up signal, in case a longer synchronization preamble should is used.

The values used in this work for the above components are specified in table 6:

Component	Value	Component	Value
C_1	10 nF	R_2	300 kΩ
C_2	10 nF	R_3	10 MΩ
C_3	5.6 nF	R_4	9.1 MΩ
C_4	15 nF	R_5	10 MΩ
C_5	33 nF	R_6	10 MΩ
R_1	360 kΩ	R_7	680 kΩ

Table 6 – Component values used for the comparator and data slicer.

The comparator used in this work was a TS881, with a low quiescent current of 210 nA [72]. The bias resistors consume a further 200 nA. The sensitivity of the circuit was measured, and the node messages could still be properly processed by the microcontroller with power input down to -31 dBm at the input of the 4-stage rectifier circuit. Maximal data reception speed was measured to be approximatively 40 kbps. An example of a received message on the output of the rectifier is presented in fig. 71.

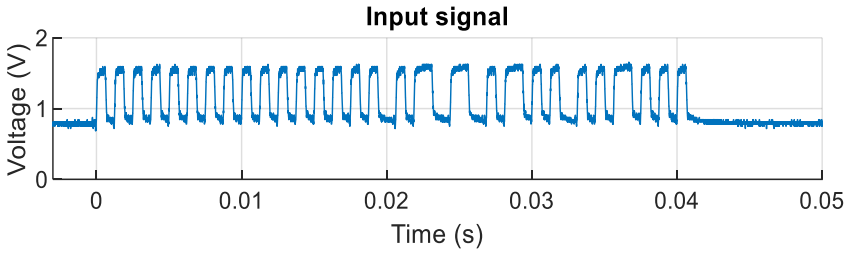

Figure 71 – Received message on the output of the rectifier.

It can be observed that the message is ASK modulated data, as the voltage varies as a zero or a one is received, in this specific case, the node was also powered via RF simultaneously. This message is then processed by the comparator module, resulting in the output shown in fig. 72:

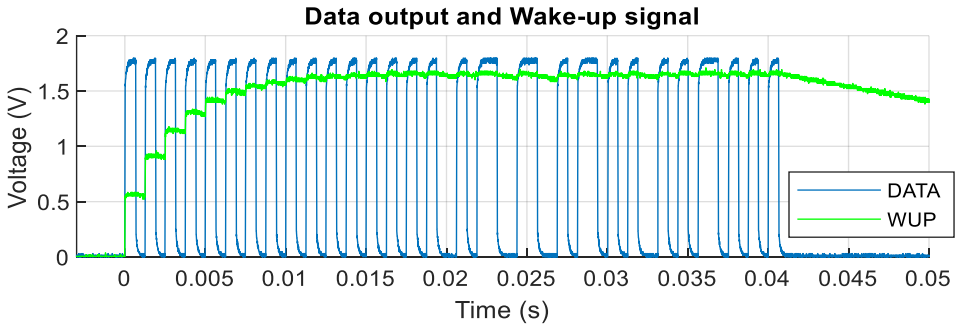

Figure 72 – Message demodulated by the comparator, showing the data sent received, and the wake-up signal.

Comparing the two previous figures, it can be seen that the message is properly demodulated by the comparator module, and that the data is an image of the signal at the

output of the rectifier, normalized to 1.8 V, which is the supply of the digital section of the node. The wake-up signal can also be observed; it is generated incrementally as the preamble is present at the data output, and can signal the microprocessor in the system to wake-up and process the message. The discharge of the wake-up signal can also be seen at the end of the transmission.

Fig. 73 shows a photograph of the implemented comparator board.

Figure 73 - Physical implementation of the comparator module.

Section II.g – Functionality

In this section, the functionality/microcontroller module used in the node will be described and measured. Its position in the node is shown in fig. 74:

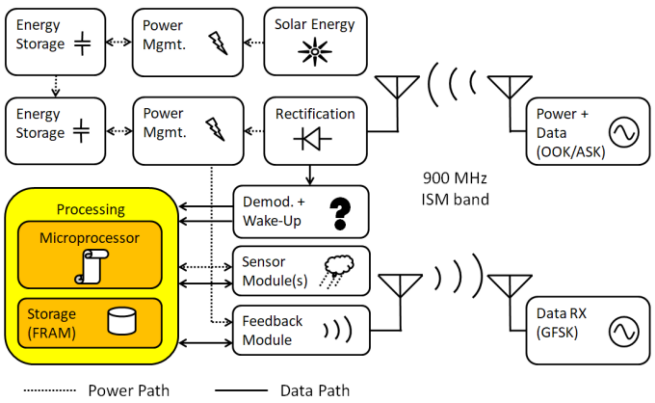

Figure 74 – Position of the functionality/microprocessor module in the node.

The intelligence of a node is defined by the node's aptitude to process, collect, store and retrieve information. This part of the node orchestrates the operation between all the different digital modules of the node, such as communications, storage, data processing, and measurements. It must also be capable of interfacing with the power management modules, in order to determine proper operation if power is scarce. Therefore, it is important that the firmware governing the node be conservative in terms of power usage. Furthermore, the microcontroller must also be capable of properly communicating with the external world, notably with sensors, in order to collect data to transmit.

As the principal limitation of this node is power consumption, a very low power microcontroller must be chosen for information processing. Ideally, storage must also be implemented, as data retransmission may not always be possible in real-time. Communications interfaces must ideally use as little power as possible, yet also be able to interface to several devices at once, in order to maximize the functionality of the node.

Subsection II.g.1 – Overview and Metrics

A summary of important parameters used for the design of the functionality module are presented in fig. 75:

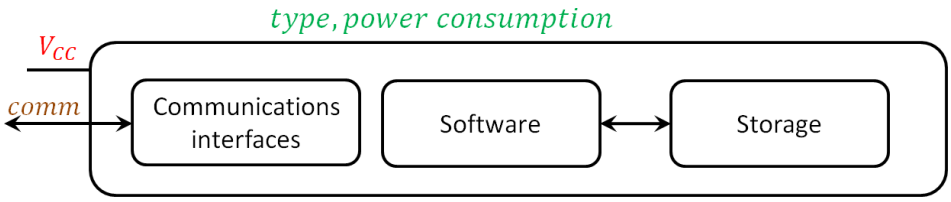

Figure 75 – Functionality metrics.

Important metrics of this module include the following:

- The type of microcontroller used for the functionality aspect of this module,
- The supply voltage, V_{CC},
- The peak and average power consumption during various operating states of the microprocessor,
- The time taken in various states of operation,
- The communications interfaces available to it,
- The software implemented in the microcontroller,
- The storage space available,

Subsection II.g.2 – Implementation

In order to interact with the environment, perform commands sent, and to manage the concurrent operation of different modules, the data decoding capabilities and intelligent functions of this sensor node are provided by a PIC16LF1559 microcontroller [73]. As this microcontroller does not have storage memory, a 128 kilobyte F-RAM IC, an MRV45V100A, is used to store data [74]. While sleeping, the quiescent current of the microcontroller and F-RAM are 30 nA and 100 nA, respectively, in sleep mode.

At any point in its operation, if the microcontroller detects that the battery is low, as indicated by the power management modules, it immediately interrupts the task it is processing and goes into sleep mode, in order to avoid regressing the power management modules into “cold start” mode.

In order to minimize power consumption, the PIC spends as much time as possible in sleep mode, and only wakes up when an event is received from the comparator/data slicer module. A Manchester decoding algorithm is implemented in a purely software-based manner, using interrupts and timer loops in order to demodulate incoming data after a wake-up, fig. 76.

Although software-based decoding is time consuming, and thus power inefficient, no suitable devices exist to implement this functionality at a reasonable power cost. However, the algorithm can be adapted for different synchronization formats, message sizes, and data transmission speeds, from 20 bps up to 10 kbps.

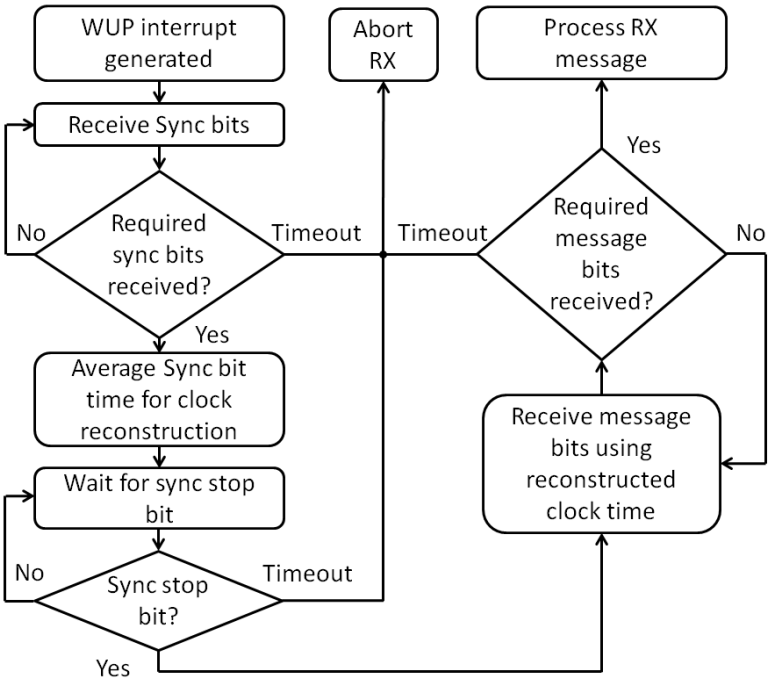

Figure 76 – Operation of the node during the reception of a command.

In order to communicate with external peripherals, the PIC possesses two, independent communication modules, which can be used with SPI or I2C protocols. Most sensors and external devices that can communicate with microcontrollers use either of these interfaces.

One I2C/SPI bus is reserved for communications with system peripherals, that are integral to the correct operation of the node, and the other bus is reserved for communications with environmental sensing devices. This permits the control of power consumption, as the PIC may power on or off system devices and sensors to minimize power consumption, and to reduce the possibility of a single point of failure. Generally, if possible, the SPI communications protocol should be prioritized, as it uses push-pull outputs to transmit and receive data, whereas I2C uses an open-drain architecture, which can be power consuming, as the standard specifies that the pull-up resistors used should be around several tens of kilo-ohms at most.

Once a message is received, it is then processed. If successful, then an action is performed, fig. 77. The node possesses a programmable 1-byte address, which can permit the deployment of 256 nodes.

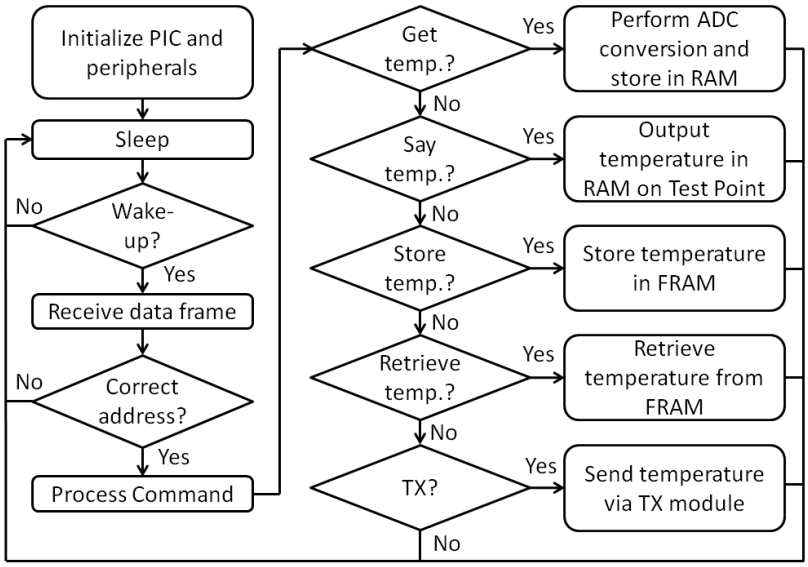

Figure 77 – Operation of the node after the receipt of a message.

The various commands that the node can process are listed in table 7:

Byte	Description of command instructions
0xF0	Samples the temperature of the node
0xF1[1]	Show the temperature on a test point
0xF2[1]	Turn on the FRAM power supply, makes the FRAM sleep
0xF3[1]	Turn off the FRAM power supply
0xF4[1]	Turn on the comparator power supply
0xF5[1]	Turn off the comparator power supply
0xF6[1]	Shows the command on a test point
0xF7[1]	Resets the temperature in the node to 25 °C
0xF8	Send the node temperature via the TX module
0xFB	Sanity check of FRAM and TX modules (verify device IDs)
0xFC	Change the node's address
0xD*n*[2]	Store the temperature in FRAM address *n*
0xC*n*[2]	Retrieve the temperature in FRAM address *n*
0x3*n*[1, 2]	Set the high nibble of the temperature byte in RAM with *n*
0x4*n*[1,2]	Set the low nibble of the temperature byte in RAM with *n*
[1]These commands are used for debugging purposes. [2]For these commands, *n* is a variable, ranging from 0x0 to 0xF	

Table 7 – Commands avaialable in the node's current firmware.

An example of the results of a received command, fig. 78, is illustrated with the PIC indicating current temperature through a test point, configured to show the temperature in a pulse-modulated format.

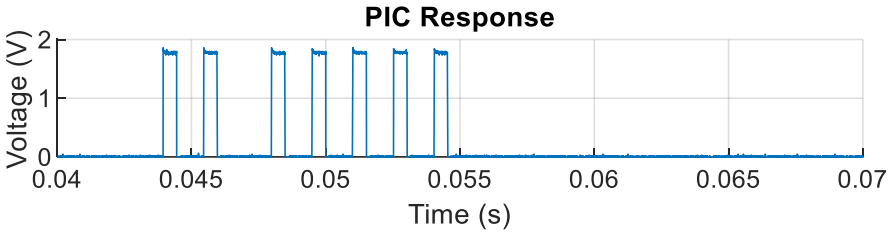

Figure 78 – Example of the PIC outputting temperature on a test pin after a temperature request (25°C).

The constructed functionality module is shown in fig. 79. Interfaces to the data reception module, power management modules and the sensor modules can be seen to the left, bottom and right respectively. The top connector provides access to the PIC programmer.

Figure 79 – Physical implenetation of the microprocessor and data storage (F-RAM).

Section II.h – Sensors

In this section, the sensor modules used in the node will be described and measured. Their position in the node is shown in fig. 80:

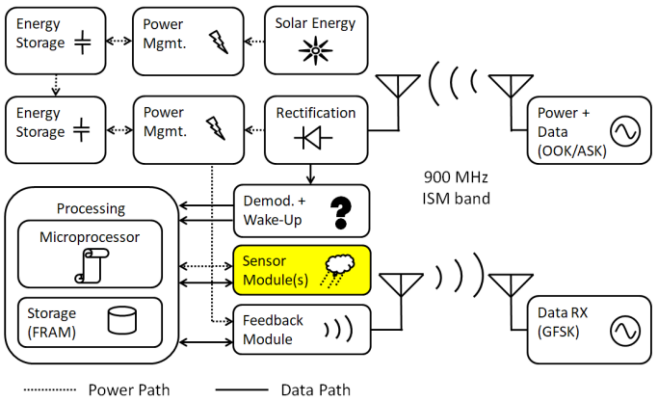

Figure 80 – Position of the sensor modules in the node.

Sensors are of quintessential importance to the node. They are used to collect data on the surrounding environment, and without them, the node would have limited, if any, utility. Currently available sensors for environmental parameters are diverse, and exist in many different formats, voltage supplies, and can measure various environmental parameters.

Subsection II.g.1 – Overview and Metrics

A summary of important parameters used for the design of the sensor modules are presented in fig. 81:

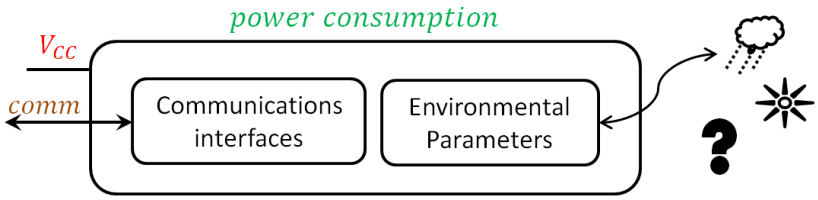

Figure 81 – Sensor metrics.

Important metrics of this module include the following:

- The supply voltage, V_{CC},
- The peak and average power consumption during various operating states of the sensors,
- The time taken during various operating states of the sensors,

- The communications interfaces of the sensors,
- The environmental parameters measured by the sensors.

Subsection II.h.2 – Sensor Selection

Various sensors were considered for implementation. The criteria used to select sensors were supply voltage, peak and average current consumption, sensor interface, as well as the different functionalities of each sensor. A list of selected sensors is provided in table 8. All of these sensors operate with a communications protocol which is compatible with the functionality module. They can also operate with a voltage of 1.8 V.

Sensor Name	Type	Interface	Reference
MS5837-30BA	Pressure/Temp.	I2C	[75]
Si7050	Temp.	I2C	[76]
BME280	Pressure/Temp.	I2C/SPI	[77]
SM351LT	Magnetometer	Analog	[78]

Table 8 – Selected sensors for this work.

The operating states, and associated currents, of the sensors are defined as follows:

- The average current, I_{AVG}, is the current the sensor uses to perform one measurement, initializing included.
- The peak current, I_{PEAK}, is the maximum instantaneous current used by the sensor,
- The inrush current, I_{INRUSH}, is the current used by the sensor when turned on.
- The measurement current, I_{MEAS}, is the current used by the sensor during a measurement.
- The communications current, I_{COM}, is the current used for a communication with the functionality board.
- The standby current, I_{STDBY}, is the current used when the sensor is in sleep or standby mode.

Table 9 shows these measured currents for the sensors above:

Sensor	Iavg	Ipeak	Iinrush	Imeas	Icom	Iinit	Istandby	Vmin
	µA	*mA*	*µA*	*µA*	*µA*	*µA*	*µA*	*V*
MS5837-30BA	0.48	1.05	43	593	168	179	0.04	1.30
Si7050	1.40	3.45	151	212	562	610	0.12	1.80
BME280	1.50	2.41	175	750	257	546	0.10	1.80
SM351LT	0.38	1.08	13	300	-	-	0.17	1.65

Table 9 – Current consumption of the sensors.

It can be seen that although the sensors can use a lot of current when turned on, communicating or measuring, generally, during sleep mode, the current consumption remains at a minimum, which permits their use for measurements, albeit the speed at which measurements are made depends on energy availability. Furthermore, the sensors can be shut off, and the interface from the functionality module to the sensors can be disabled in order to completely remove current consumption, though this comes at the cost of having to restart and reinitialize the sensors.

Subsection II.h.3 – Implementation

Fig. 82 shows sensors boards that were made for use in this work:

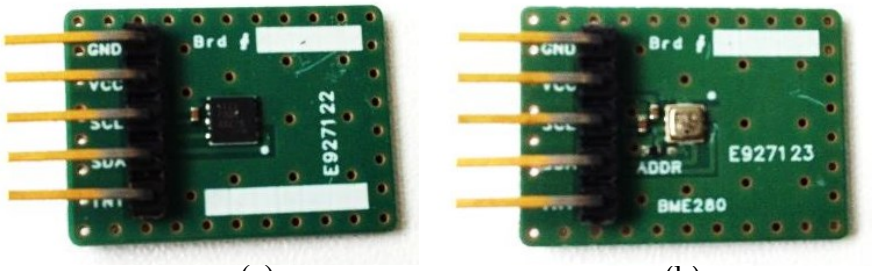

(a) (b)

Figure 82 - Various sensors. (a) Si7050 temperature sensor (b) BME280 pressure/temperature sensor.

Section II.i – Data Transmission

In this section, the data transmission module used in the node will be described and measured. Its position in the node is shown in fig. 83:

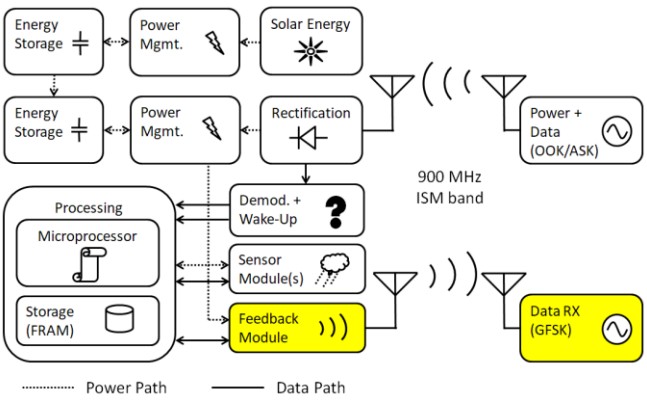

Figure 83 – Position of the data transmission module in the node.

Retransmission of data being sensed and processed by the node is of primordial importance if it is to be useful. Several methods can be used in order to retrieve data generated by sensing nodes. In scenarios where latency is not an issue, the node can be left to autonomously collect data, and the information can be retrieved when it is needed, or if possible. This method required the least amount of energy; however, the node must not be lost, and cannot indicate its status or any other information it may have collected. If proximity is not an issue, then a close-range data transfer can be organized, using either a wired or close-range wireless link. However, for a node to possess true autonomy, it is best to include a method to wirelessly retransmit data, either independently or on demand.

Several methods can be used to retransmit data, though the most ubiquitous remains the use of RF transceivers. It is commonly accepted, that in most embedded systems, the radio retransmission of wireless devices is the most consuming part of the energy budget [79].This must be mitigated by using a rapidly programmable transmitter, with low power used for transmission, and considering the time taken to set up the transmitter, data must be sent as fast as possible.

Subsection II.i.1 – Overview and Metrics

A summary of important parameters used for the design of the data transmission module are presented in fig. 84:

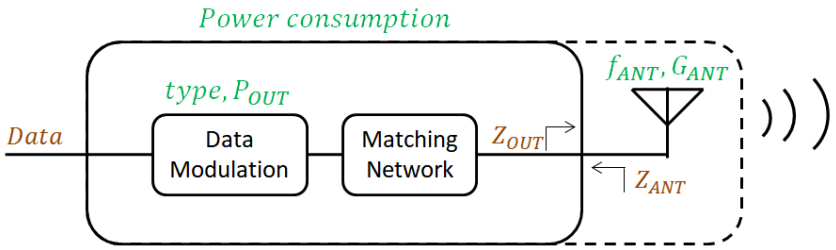

Figure 84 – Data transmission metrics.

Important metrics of this module include the following:

- The power consumption of the data transmission module while in different phases of operation, and the power supply voltage V_{CC},
- The type of modulation used, the output power, P_{OUT}, of the module, and the transmission frequency f_{TX}
- For the output antenna: output impedance Z_{ANT}, gain of the antenna G_{ANT}, and operating frequency of the antenna f_{ANT}.

Subsection II.i.2 – Implementation

The selected device for wireless data retransmission is the SPIRIT1 module, operating in the 868 MHz ISM band [80]. This IC is capable of sending data using different modulation formats, which include OOK, ASK, FSK and GFSK. The power levels used to transmit the data are configurable, within a range from 11 dBm down to -30 dBm. The baudrate of data transmission can also be configured from 1 kbps up to 500 kbps.

It can use either direct modulation, wherein the user must specify the transmitted bit stream, or use a standard predefined packet format. Using the standardized packet format, data transmission integrity can be verified using a Cyclic Redundancy Check (CRC). The Advanced Encryption Standard (AES) can also be used in order to secure data transmission. The module also includes a Carrier Sense Multiple Access (CSMA) algorithm, which can be exploited to detect if another module or device is already transmitting, thus avoiding packet collisions. Quiescent current in sleep mode is 30 nA.

For the purposes of the development of this IoT node, 2-GFSK modulation was selected in order to transmit data, at a data rate of 38.4 kpbs, and the basic packet format was used in order to minimize overhead on the microcontroller. The frequency at which the data was emitted is 868 MHz. The output power level chosen for data transmission is -30 dBm.

The frequency deviation for the modulation around the carrier is 19 kHz. A transmission of the basic packet was collected via a B200 Software Defined Radio (SDR), and demodulated in order to show the digital data sent, using the default settings of the transmitter, in fig. 85.

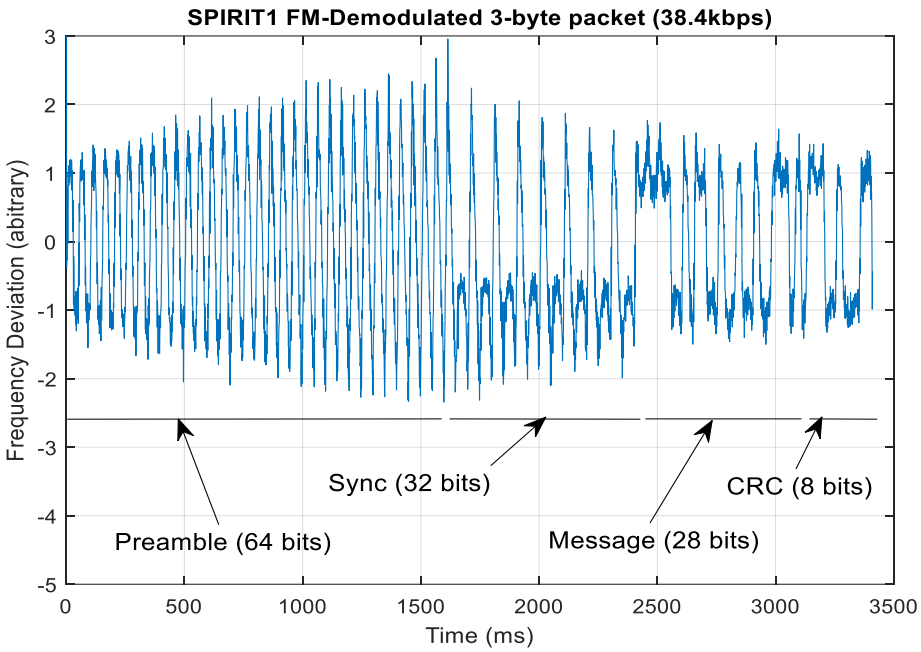

Figure 85 – Sample data packet sent using the SPIRIT1 transmitter.

The packet is split into 4 main parts: the preamble, which is 64 bits long, the synchronization word, which is 32 bits long, the actual message, which is 3 bytes (or 28 bits) long, and the CRC checksum, which is 1 byte (or 8 bits) long. The packet format can be modified through registers present in the module, and additional fields can be added, depending on the usage scenario, which includes addressing capabilities, multi-packet or variable length messages. The demodulation of the received packets is performed using the same transceiver IC, connected to the same computer that transmits messages to the node.

The data transmission module must be operated in a particular order for data to be properly sent. It must be turned on, reset, and then set into its ready operating state. Afterwards, the Voltage Controlled Oscillator (VCO) operating within the integrated PLL must be calibrated, after which it must also be returned to a ready operating state. After this initialization phase, data may be sent to the transmitter buffer, and the device may send data. At the end of the transmission, it returns into ready state, and may then be shutdown.

The device operates at 1.8 V. Fig. 86 below shows the power consumption during the transmission of a 128-bit packet, at 868.25 MHz, with an output power of -30 dBm.

Preambles and synchronization are included in the bit count, along with a 3-byte payload. A generic 50 Ω, 868 MHz omnidirectional dipole (with 3 dBi of gain) was used.

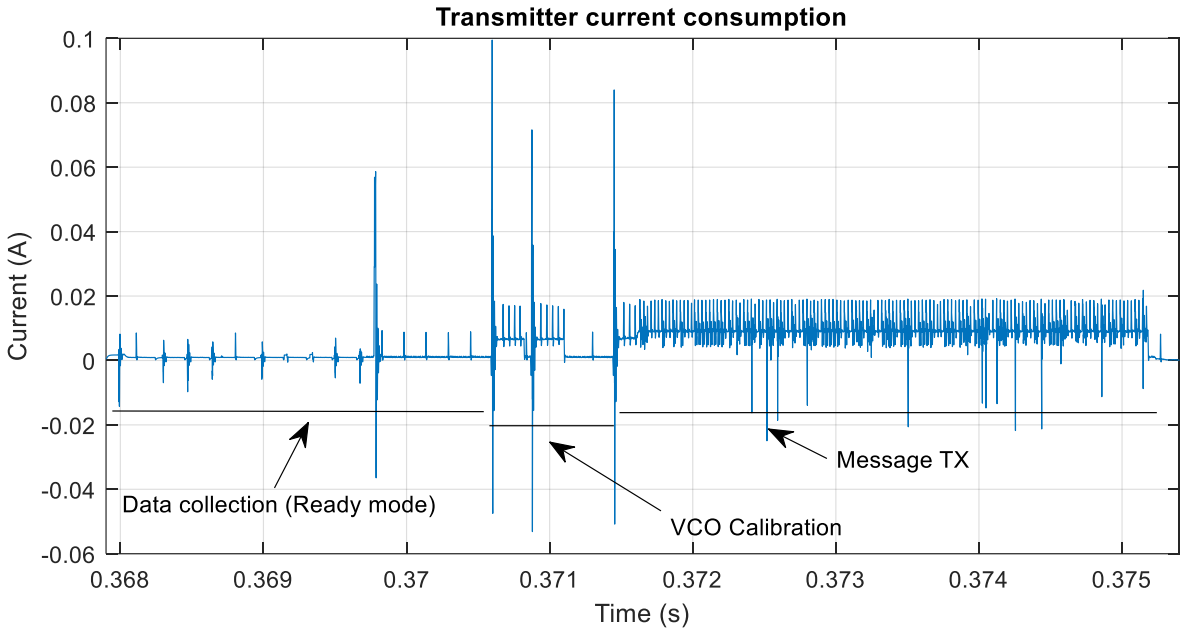

Figure 86 – Current consumption of the transmitter.

The device in shutdown mode consumes 2 nA. In ready mode, it consumes 430 µA, or 774 µW. When calibrating its VCO, it consumes 6.72 mA, or 12.33 µW. Finally, when transmitting data, it consumes 9.58 mA, or 17.56 mW. The module sends messages at 38.4 kbps, and consumes 17.56 mW while sending a message for 3.75 ms. It therefore consumes approximatively 65.9 µJ to transmit 128 bits, which is 514 nJ per bit sent during the actual transmission state. If VCO calibration and module setup is to be included, then the power consumption per bit increases to 592 nJ per bit.

The supplied software is used to receive data packets. An example of packet reception, containing temperature data as the third byte, is shown in fig. 87:

	Time stamp	Info	RSSI	Data Received
1	22:02:03.92	Packet received (3 bytes)	-81	54 3F 19
2	22:02:53.91	Packet received (3 bytes)	-80	54 3F 21
3	22:03:10.92	Packet received (3 bytes)	-81	54 3F 21
4	22:03:36.91	Packet received (3 bytes)	-81	54 3F 21
5	22:04:01.92	Packet received (3 bytes)	-81	54 3F 20

Figure 87 – Example of temperature data received from the node.

The transmitter board used is shown in fig. 88:

Figure 88 – Data transmission module.

Section II.j – Conclusion

This chapter has presented a detailed analysis into the different modules that will be used node. The approach for each module is as follows:

1. A brief description of the module is given,
2. Metrics that determine the operation of the module are stated,
3. Theoretical considerations are discussed if necessary,
4. Measurements and associated results are shown,
5. A manufactured version of each module is presented.

For the rectenna module, the antenna operates at 935 MHz, with a S_{11} of -15 dBm at the operating frequency. It has 2 dBi of gain. The rectifier uses the Greinacher topology, with a "double L" network to match the antenna to the rectifier.

For data reception, a 4-stage rectifier is used, with a sensitivity ranging from 0.1 V to 6 V for power input levels from -30 dBm to 0 dBm. For power harvesting, a 1-stage rectifier is used. Supposing a perfect MPPT configuration, measured efficiency varies from 4 % to 40 %, increasing with power input levels from -30 dBm to 0 dBm. Available power output ranges from several tens of nanowatts to 0.5 mW.

The solar panel used in this work is the large solar panel, due to increased power output, at the cost of a slightly larger footprint. Using LED lighting, typical of an indoor configuration, a measured efficiency of around 1.5 % to 3.5 % is observed. Although the measured efficiency is low compared to typical outdoor lighting conditions, available power on the large solar panel ranges from several hundreds of μW to 2 mW – 3 mW. Even at extremely low luminosity, the power output of solar panels is several orders of magnitude higher than the rectifier for low RF power levels.

A single ceramic capacitor used in this work can store up to 1.8 mJ of usable energy, whereas the supercapacitor can store up to 3.76 J of usable energy. It is possible, however, to create an array of ceramic capacitors. The use of the supercapacitor and ceramic capacitors are recommended, respectively, for solar power harvesting and RF power harvesting. Leakage currents remain problematic for conservation of energy, especially for the supercapacitor.

Power management for the node are ensured by bq25570 and bq25504 modules for solar and RF power harvesting, respectively. These contain boost converters and are capable of MPPT, ensuring an efficient extraction of energy. In order to share energy, the storage elements of these modules are tied together through a Schottky diode. The bq25570 contains a buck converter, used to supply the node with power. Their quiescent current remains minimal, at approximatively 500 nA each, independently of voltage.

The radio demodulator module can process amplitude-modulated transmissions (OOK/ASK) at 935 MHz, with a sensibility of -31 dBm. Its quiescent current is approximatively 400 nA in operating conditions. It also generates a wake-up signal to alert the node in case a message is received.

The functionality module of the node contains microprocessor and FRAM data storage. It can software-demodulate received messages encoded in a Manchester format, and depending on the command received, complete actions requested. The control of external sensors and modules is possible, using either a SPI or I2C bus. Each functionality module contains an address, which can be used to differentiate between several nodes. During sleep, quiescent current is approximatively 130 nA.

A variety of sensor modules are available, capable of measuring various environmental parameters, such as luminosity, temperature, barometric pressure and/or magnetics fields. Average operating currents can range up to 1.5 µA, however, the modules can be shut-off using the microprocessor in the functionality module.

A data transmission module capable of sending messages was also characterized for this work, and is capable of a variety of modulations at variable baud rates. It can also emit at different power levels, ranging from -30 dBm to 10 dBm. Although instantaneous power consumption is approximatively 9.58 mA when sending a message at -30 dBm, transmission of data costs approximatively 592 nJ per bit for a 128-bit message. Its sleep quiescent current is 2 nA.

Using the above modules, the next chapter of this work will fully characterize the power consumption of an IoT node composed of these modules. Different scenarios of operation will be envisioned, and tested using a test bench for in-situ measurements, as well an empirical simulator to analyze the feasibility of such scenarios.

This page intentionally left blank.

Chapter III

System Analysis

This page intentionally left blank.

Chapter III System Analysis

Section III.a – Introduction

In the previous sections, the importance of IoT nodes and the development of different modules for such a node were explored, giving performance metrics for different parts of the system. This section will analyze the fully assembled node, study its power consumption profile depending on its activity, and showcase its performance under several different scenarios of application.

Although performance of the node may be reduced compared to more specific or VLSI-based implementations of different submodules, the purpose of this work is not to seek optimal performance of all subsystems, but to showcase the feasibility of passive power harvesting in order to implement such nodes, whilst providing useful levels of operation which can be expected in an IoT network.

Section III.b – Modular Design

Subsection III.b.1 – Initial Iteration

The initial iterations of the modular system were haphazard at best, due to the lack of standardization between module size, shape, and connectivity, fig. 89.

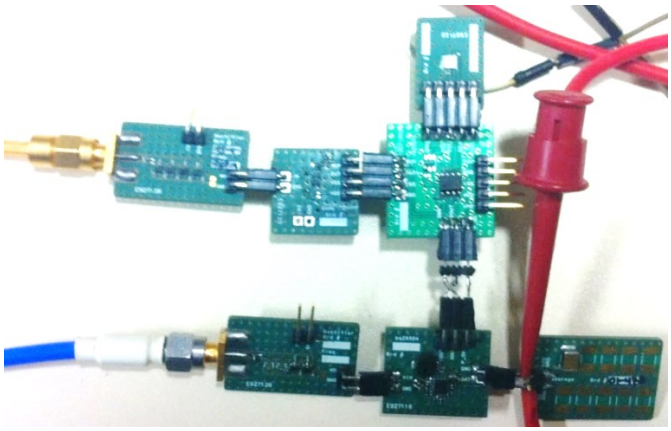

Figure 89 –Initial iterations of the node's modular format.

As can be seen, this system created difficulties in getting different modules connected together, and prototypes with different modules were sometimes incompatible, as connectivity could not be ensured between different modules that provided the same function. This system was also particularly vulnerable to spurious disconnections, and was not mechanically robust. In order to solve this issue, a more modular format was developed.

Subsection III.b.2 – Final Iteration

The second modular system was developed using a standardized format, fig. 90:

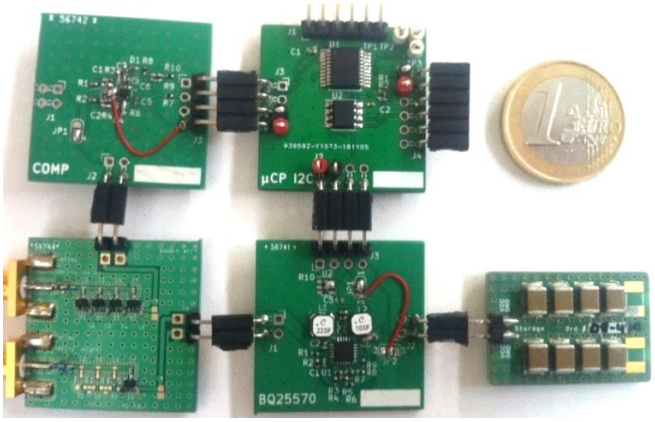

Figure 90 – Improved modular format, with a euro coin for reference.

The modules measure 3 by 3 cm. Power polarities were standardized in order to avoid power rail and ground inversions, and the connectors are aligned in order to provide easy "plug and play functionality". Due to the alignment of connectors and circuit boards, the node remains highly immune to spurious disconnections between circuit boards.

Furthermore, the format easily permits the replacement of various modules of the node, allowing independent testing, measurement and assembly of the node in order to test different architectures and functionalities. The node that is used for measurements, testing and for the simulator is presented in fig. 91:

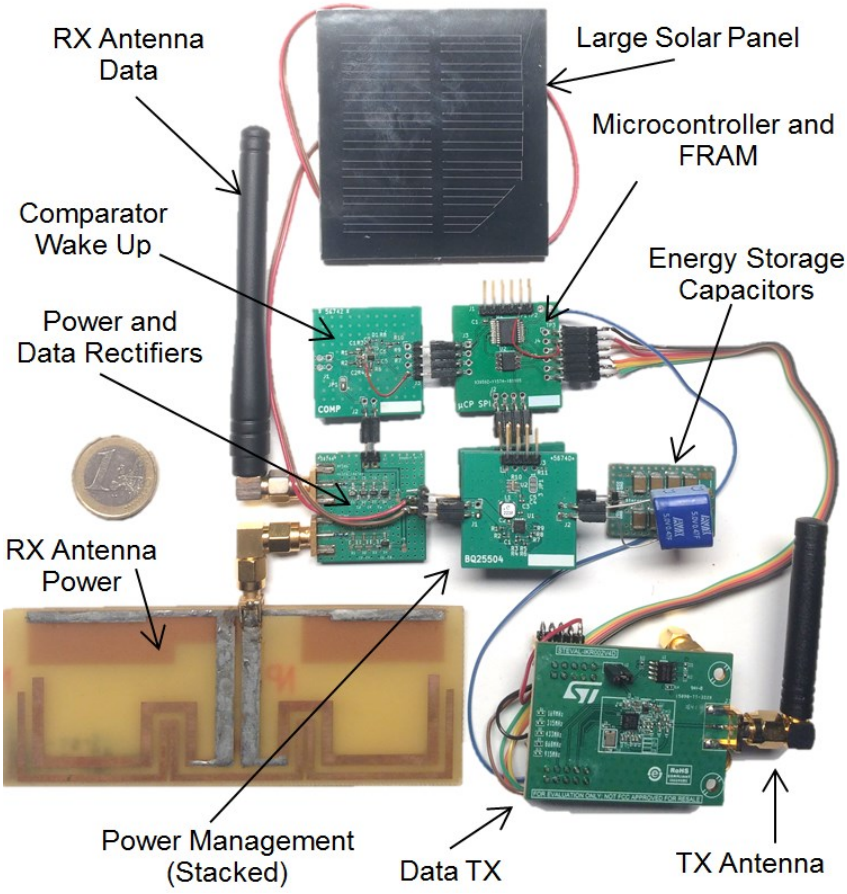

Figure 91 – Fulyl assembled node.

It includes a separate data and power reception antenna, a dual rectifier board for the former and latter, respectively, a solar panel, dual power management modules, a wake-up radio module, energy storage modules, and a functionality module (µC). Functionality in this case is provided by an SPI bus on the microcontroller, to which a data transmission module is connected and powered. A temperature sensor is provided in the microcontroller.

Section III.c – Power Consumption

In order to accurately model the node, a good understanding and measurement of its power consumption is required. This permits the validation of different scenarios of operation, and can be used in order to give a rough estimate of the node's performance in a range of given hypothetical scenarios. This is important, as it may be necessary to limit certain power consuming features of the node (mainly the retransmission of any measurements) when only minimal amounts of power are available, notably when only RF power is available. It is equally important to determine the required size of storage elements in order to meet the requirements of a given scenario.

This section characterizes the power consumption of the different modules developed for the node, taking into account their different power consumption levels during various modes of operation. The modules are subdivided into both digital and analog ones. Digital modules have more phases of operation than analog modules, the latter having more predictable and static power consumption over time. For this node, the voltage delivered to the node, V_{CC}, from the power management module, is configured to 1.8 V.

Subsection III.c.1 – Power Management Modules

The power management modules are composed of a bq25504 for RF harvesting, and a bq25570 for solar harvesting, present similar power consumption to each other. During their respective cold-start modes, at least 15 µW has to be present at their power inputs to operate the cold-start charge pumps. If less power is present, they will never manage to enter warm-start (normal) operational mode, due to the inefficiency of the cold-start charge pump, which is approximatively 5%, leakage currents of storage elements notwithstanding.

Once in normal mode, the power consumption of the devices varies little, and is voltage-independent. With no power present on the input, this was measured to be around 500 nA. Depending on the storage element voltage, this can range from a power consumption of 2 µW down to 850 nW, with the voltage decreasing, respectively.

For the bq25570, which contains the buck converter that is used to supply the node with a voltage regulated to V_{CC}, the efficiency of the converter exceeded 80% for load currents above 10 µA. However, for currents between 1 µA and 10 µA, the efficiency

dropped down to 60%, and for load currents below 1 µA, the efficiency is approximatively 20% or less, fig. 92.

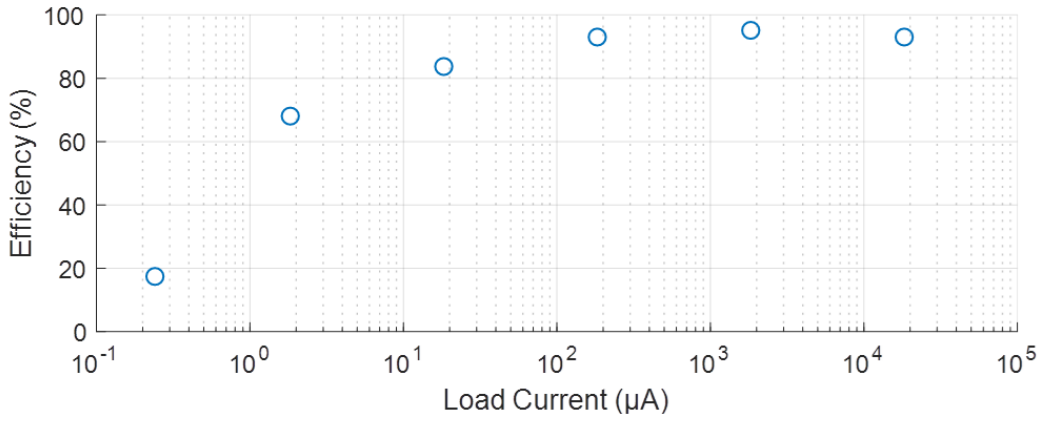

Figure 92 – Measured efficiency of the buck converter, measured against manufacturer specifications.

Subsection III.c.2 – Energy Storage Modules

This work uses two types of energy storage modules. For RF-based and solar-based energy storage, respectively, low leakage ceramic capacitor elements and high capacitance supercapacitors are used.

Both types of capacitors are capable of storing energy as a function of their nominal capacitance. They differ, however, in terms of their leakage currents. The ceramic capacitors used in this work have a worst-case insulation resistance of 100 MΩ·µF, or approximatively 220 kΩ. The worst-case leakage should therefore occur when the capacitor is fully charged, which gives a leakage current of 1.8 µA at 4 V. Measurements have indicated that the leakage current is generally in the hundreds of nA range.

The supercapacitor has higher leakage current of around 6 µA, 72 hours after self-discharging. The current was measured to be approximatively around 10 to 20 µA after discharge starts, leakage currents in supercapacitors tend to decrease over time. The ESR of this supercapacitor is approximatively 400 mΩ.

Subsection III.c.3 – Data Reception Module

The data reception module consumes the most power when the node is asleep, for two reasons. Firstly, the inputs of the comparator are polarized to $V_{CC}/2$. This is due to the presence of a high-pass filter, whose purpose is to reduce the effects of low-frequency

interference. This resistor network consumes approximatively 180 nA, or 324 nW. Secondly, the comparator itself has a quiescent current of 220 nA, or 396 nW. Additional current is used when the wake-up and data outputs change, due to the reception of data. This was measured to be about 10 nA to 20 nA at most, or 18-36 nW. The module therefore consumes about 850 nW of power during any phase of operation of the node.

Subsection III.c.4 – Functionality Module

The PIC microcontroller has several modes of operation: deep sleep mode, message reception mode (separated into false wake-up reception and full message reception), message processing mode (which includes SPI transactions), and temperature/ADC measurement mode.

The power consumption in of the PIC in deep sleep mode is measured to be 40 nA, or 72 nW. When receiving messages, whether due to false wake-ups or actual messages, the consumption of the microcontroller is 230 µA, or 415 µW. However, the amount of time spent processing messages depends on their validity. In message processing mode, the power consumption is 410 µA, or 738 µW, and, finally, in temperature/ADC measurement mode, the power consumption is 800 µA, or 1.44 mW.

Another metric that is important is the amount of energy consumed per bit received. The microcontroller receives messages at approximatively 800 baud, and consumes 415 µW while receiving a message. As the received message is 36 bits long, it takes 40 ms to receive a message. It therefore consumes 16.6 µJ, which is approximatively 461 nJ per bit received.

The FRAM IC present in the functionality module also has several modes of operation: read mode, write mode, sleep mode and idle mode. In sleep mode, current consumption is measured to be 30 nA, or about 55 nW. During this mode, the FRAM is not available to process commands, and must be woken up in order to operate. Wake-up time is measured to be 15 µs.

Once woken up, the FRAM is in idle mode, where it consumes 4 µA of current, or 7.2 µW. In this mode, the FRAM module is ready to read and write data, depending on the commands that it is issued. Reading a byte of data from one address consumes 2.13 mA, or 3.83 mW of energy. Writing a byte of data consumes 2.32 mA, or 4.17 mW of energy. The power consumption of FRAM modules is significantly lower than Flash devices [81].

Subsection III.c.5 – Data Transmission Module

The data TX module must be programmed in a particular order, so as to ensure data transmission. It must be turned on, reset, and then set into its ready operating state. Once this is complete, the Voltage Controlled Oscillator (VCO) operating within the integrated PLL must be calibrated, after which it must be set back into a ready operating state. Once the initialization phase is finished, data may be sent to the transmitter buffer, and the device may send data. When the transmission ends, it returns into ready state, and may then be shutdown.

The TX module, in shutdown mode, consumes 2 nA of current, or 2.6 nW. In ready mode, it consumes 430 µA, or 774 µW. When calibrating the VCO, it consumes 6.72 mA, or 12.33 mW. Finally, when transmitting data, it consumes 9.58 mA, or 17.56 mW.

The module is programmed to send messages at 38.4 kbps. As the transmitted message is 128 bits long, it takes 3.75 ms to send it. During this transmission, it consumes 17.56 mW. Therefore, approximatively 65.9 µJ of energy is used, which is 514 nJ per bit. If VCO calibration and module setup is to be included, then the power consumption increases to 592 nJ per bit.

Subsection III.c.6 – Summary

This section has analyzed and documented the power consumption of different elements present in the node. A summary of power consumption is presented in table 10 for analog components:

Device	State	Current (µA)	Power (µW)
bq25570	Warm Start/Full Start	500	850 - 2000
	Cold Start	-	15
bq25504	Warm Start/Full Start	500	850 - 2000
	Cold Start	-	15
Comparator	Static	0.42	0.756
Supercapacitor	Leakage	5 - 20	20 – 80
Ceramic Capacitor	Leakage	0.1 – 2	0.4 – 8

Table 10 – The power consumption of the different analog parts in the node's modules.

A summary of power consumption is presented in table 11 for digital components:

Device	State	Current (µA)	Power (µW)
PIC	Sleep	0.04	0.072
	Message RX	230	423
	Processing	410	738
	Temp. measurement	800	1440
	False Wakeup	230	423
FRAM	Sleep	0.03	0.054
	Idle	4.00	7.200
	Storage (read)	2130	3834
	Storage (write)	2315	4167
SPIRIT1	Sleep	0.02	0.036
	Ready State	430	774
	VCO calibration	6720	12334
	TX (-30 dBm)	9580	17558

Table 11 – The power consumption of the different digital parts in the node's modules.

A summary of power consumption is presented table 12 for the node as a whole:

Command	Duration (ms)	Power (µW)	Energy Used (µJ)
Sleep mode	-	0.92	-
False wakeup	16.8	416	7.00
Temperature measurement	40.6	422	17.1
FRAM data storage	42.1	420	17.7
FRAM data retrieval	42.2	417	17.6
Data transmission	55.9	1750	97.8

Table 12 – The power consumption of the whole node, depnding on its state of operation.

Section III.d – Simulations

With the node's power consumption analyzed in the previous section, an iterative power consumption simulator, based on the previous measurements, was developed with MATLAB in order to be able to simulate the node's performance by creating hypothetical scenarios. In order to ensure the accuracy of the simulator, the hypothetical simulations were compared against real node performance.

Theoretical predictions of device power consumption were calculated by taking into account multiple factors from the empirical data measured previously. These include various inefficiencies of the device, including the leakage current of storage devices; the power consumption of the power management modules; the quiescent currents of the different components and their power consumption during the various phases of operation.

Subsection III.d.1 – Simulator Overview

Due to the complexity of the node, it is impossible mathematically model its power consumption as a single equation. However, by measuring performance of the various modules of the node, mathematical models for the behavior of different integrated circuits can be extrapolated, and the flow of power in the device can be modeled as a function of time, by combining different models together.

The simulator used in this approach is iterative, approximating the power consumption over a small period of time, Δt. Once the calculation of the power consumption during Δt is complete, the various parameters are updated, and the next state is calculated from this new state. The general equation modeling the consumption of any given module of the node in the simulator is show below:

$$P(t) = P(t - \Delta t) + M(\Delta t, S)$$

Where P is the power consumption of any given device, M is the change in power consumption over the previous Δt time increment, and S is the current state of operation of the node, which includes current power conditions (solar and RF), power storage element levels, and any operations undertaken by the node.

The general flow of power in the simulator, fig. 93, is used as a framework to develop the simulator:

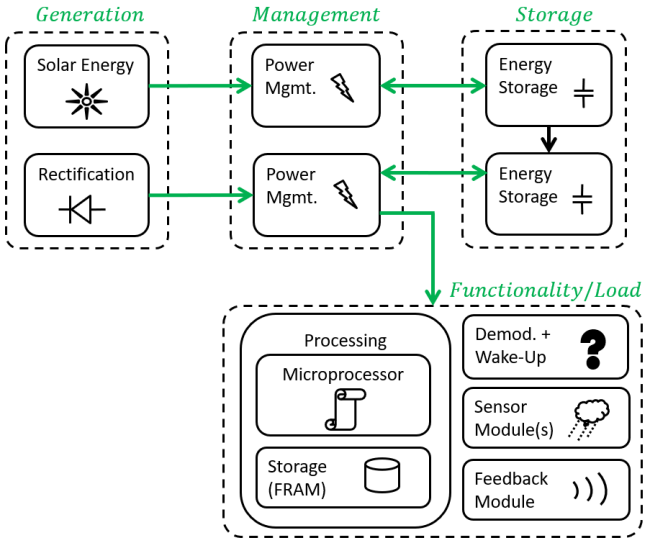

Figure 93 – Flow of power within the node.

Subsection III.d.2 – Models

In order to model the simulator, the different elements of the node must be analyzed to understand their impact of on the power flow within the device. Once understood, these impacts are then modeled appropriately, and the power flow within the simulator is adapted to respect the constraints of the devices.

Unless otherwise specified, models are derived from power consumption data presented in the previous section, or from data presented in chapter II.

Subsubsection III.d.2.i – Energy Generation

The rectenna is a power generating device. Therefore, in the simulator, it is modelled as a device that generates a certain amount of power in watts depending on the power input of an RF signal that it receives, in dBm. Variables of adjustment in the simulator for the rectenna include the efficiency of the rectifier circuit, antenna gain, and an adjustment of power input based on frequency changes, derived from S_{11} parameters, fig. 94.

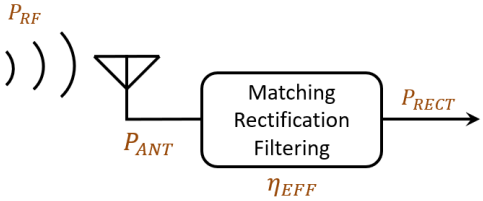

Figure 94 – Variables influencing the production of power at the rectifier.

Similarly to the rectenna, the solar panel is also modelled as a power generating device, wherein power is delivered depending on luminosity. Variables that determine the power output of the solar panels include their effective area, and the type of lighting, and the efficiency of the solar panel, fig. 95.

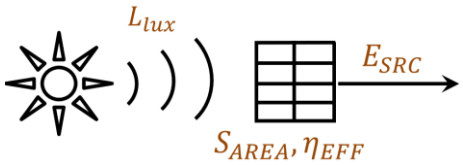

Figure 95 – Variables influencing the production of power at the solar panel.

Additional types of energy generation circuits can also be implemented into the simulator, provided that they can be characterized and modelled.

Subsubsection III.d.2.iii –Power Management

Once the generation of power is analyzed, it is necessary to determine how the power will be used in the node. The first devices to process the received power are the power management devices: the bq25504 and the bq25570.

The power management modules serve several purposes: they boost the incoming voltage and permit the storage of energy from generating devices, they manage an efficient extraction of energy from energy generating devices, and they also provide a regulated voltage to energy consuming devices in the node.

Variables of adjustment for these devices include the amount of power at the input, the type of operating mode (cold-start or warm-start), and the associated energy extraction efficiencies, the quiescent current of the device, fig. 96. For the bq25570, there is an additional variable, which is the efficiency of the buck converter, as a regulated voltage must be provided to the node. Its efficiency depends on its load.

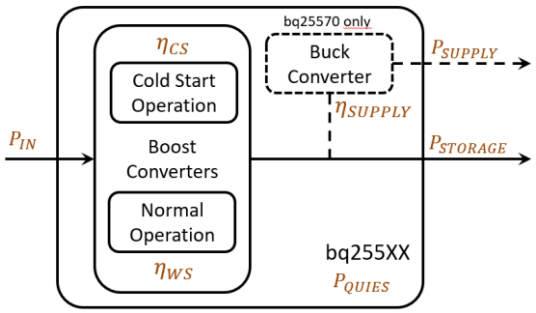

Figure 96 – Variables influencing the consumption of power by the power management modules.

Subsubsection III.d.2.iv – Energy Storage

Energy storage devices, theoretically, neither generate nor consume power. Practically, due to losses and leakages, however, they act as devices that consume power, albeit very little. As capacitors are used for energy storage in this work, the sources of loss for these types of components comes from self-discharge/leakage losses, and ESR losses when power is stored or taken from the capacitor. Variables for adjustment therefore include ESR and leakage currents that depend on the type of capacitor, fig. 97:

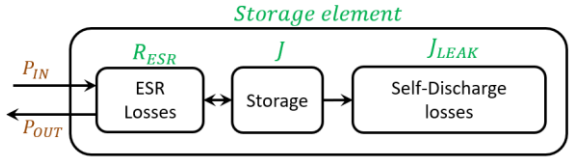

Figure 97 – Variables influencing the storage of energy in the energy storage modules.

Analysis of unloaded capacitor discharge curves have yielded an analytical solution for leakage currents, which can be modelled by the following equation:

$$V(t) = Ae^{B \cdot t} + Ce^{D \cdot t}$$

The coefficients determined for this equation, based on different capacitor types, are shown in table 13:

Capacitor	Coefficients			
	A	B	C	D
470 µF Ceramic	-	-	3.95	$-5.32 \cdot 10^{-5}$
470 mF Supercapacitor	$3.06 \cdot 10^{-1}$	$-1.91 \cdot 10^{-4}$	3.98	$-1.96 \cdot 10^{-6}$

Table 13 – Coefficient parameter table for the ceramic capacitor and the supercapacitor used in this work.

The two different elements in the equation represent soakage and leakage currents, respectively. Soakage current was not implemented in the simulator for the ceramic capacitors, as it was negligible compared to self-discharge current. It can be noted that the C coefficient represents the original voltage of the capacitor, and D the RC discharge time constant, where R is the insulation resistance. R varies as a function of voltage; however, the worst-case value is used for the purpose of calculating D.

Subsubsection III.d.2.v – Functionality/Load

In the node, the remaining devices, which implement the rest of all the functional aspects of the node, only consume power, fig. 98. The variables are generally determined by

the type of device, which is to say whether it is an analog or digital. Analog devices generally consume a certain static quiescent current, with a secondary dynamic current sometimes occurring if changes in input and outputs occur. Digital devices consume a fixed amount of power depending on their state of operation.

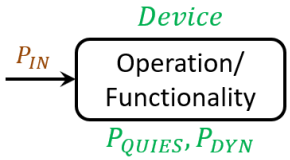

Figure 98 – Variables influencing the consumption of energy in the data reception module.

Subsection III.d.3 – Simulator Algorithm

The previous section analyzed and categorized elements as one of four types of power consumers for simulation purposes:

- Energy Generators,
- Energy Translators (Power Management)
- Energy Storage,
- Energy Consumption (Functionality).

Simulation of such devices requires a structured approach based on time. A time increment, Δt, is chosen to be small enough to account for all phenomena that occur during normal operation, which is considered to be at least the smallest amount of time any operating mode of any of the devices in the system lasts.

The flow of the simulator is as follows:

1. All fixed parameters for the scenario to be simulated are set in the simulator. These include:
    - A list of energy providers with the amount of energy they can provide depending on their type (fixed parameters can include solar panel size, RF frequency of operation…)
    - A list of energy consumers, and their respective power consumption during various states of operation (FRAM read/write, TX energy consumption, quiescent currents…)
    - A list of power storage elements, and their associated capacities and inefficiencies (capacitor size, EST, leakage current profile…)

- A list of power management translators, their states of operation, and their respective power consumption and transfer efficiencies (buck conversion efficiency, quiescent currents, cold or warm start modes…)

2. All the elements are initialized to their default state, according to the scenario of operation that will be simulated.
3. Every time increment Δt, according to the flow of power, the interaction between the aforementioned elements is calculated, and the state for each element is updated according to external stimuli, such as the reception of a message, or a change in simulation conditions, such as different levels of luminosity, or message frequency. Calculations are performed in the direction of the connections between devices according to the flow of power, in order to ensure an accurate simulation.
4. Step 3 is repeated until a request to end the simulation is sent to the simulator.
5. Data of importance is stored, and visual representations can be shown to the user.

A general overview of the simulator is presented in fig. 99:

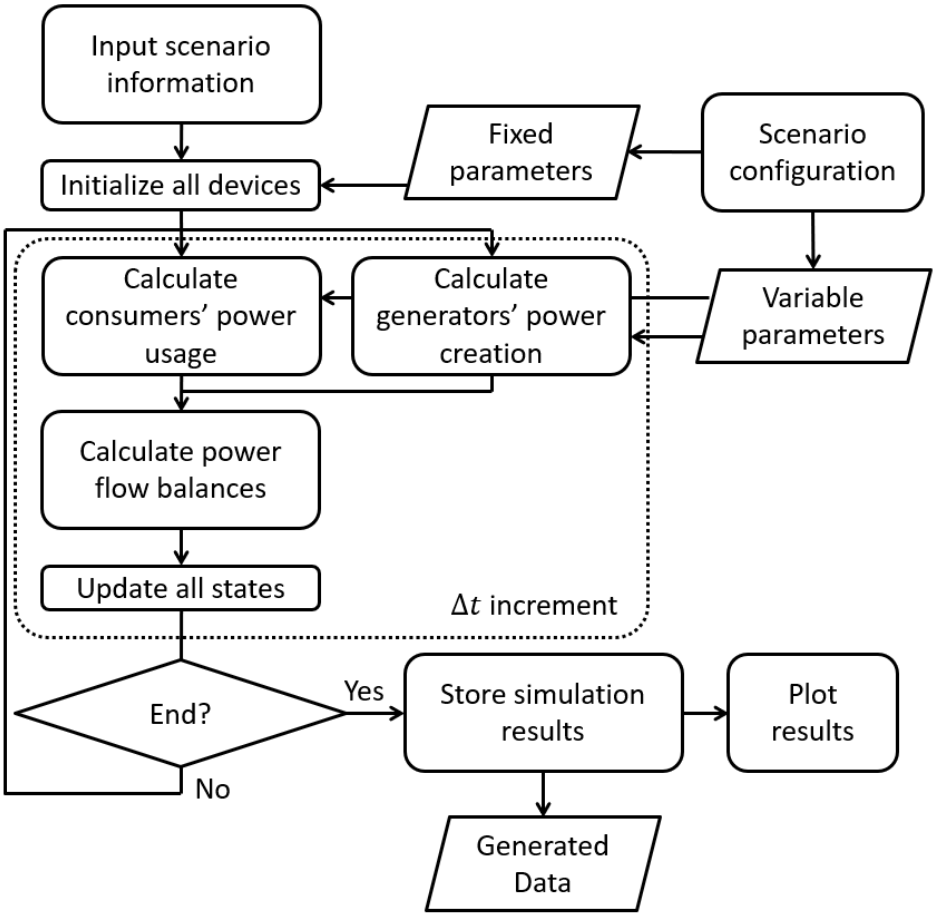

Figure 99 – General overview of the simulator architecture.

The interaction between the simulator and devices present in it are shown in fig. 100:

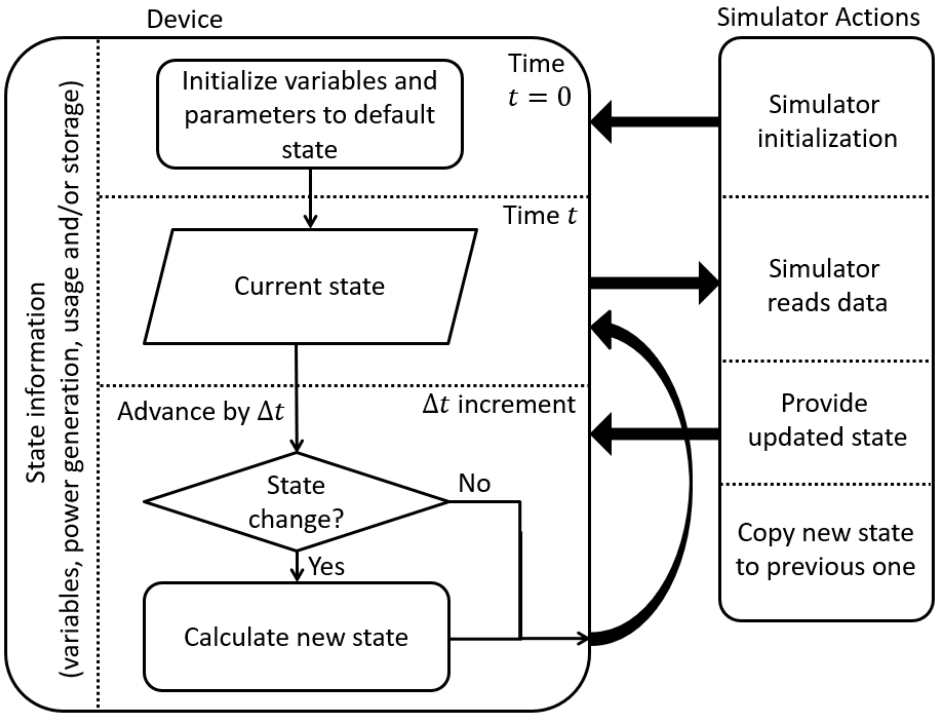

Figure 100 – Simulator/Device Interaction diagram.

Scenarios, in terms of the simulation parameters, are a collection of environmental variables to be simulated around the node (i.e., RF power levels, sunlight levels, pre-charge the storage element(s), storage element size…). External stimuli can also be programmed into the scenario (i.e., sending a message to the node). It should be noted that the simulator only approximates power consumption, based on the empirical measurements presented in the previous sections. Therefore, no information or results that the node could otherwise produce can be inferred.

The simulator can be adapted for different node configurations and different scenarios. It can therefore be used in order to study the viability of a scenario, before any test bench is setup, or measurements are undertaken.

Section III.e – Test Bench

In order for an IoT node to be useful, it is necessary for it to be able to send data back to the user. Several methods exist in order to implement this, though there is a tradeoff between energy consumption, and ease of data access.

For instance, should the node have no retransmission capabilities, but assuming collected data is stored within it, manual intervention is necessary to retrieve the information. However, this is more burdensome for the user, as it requires physical access. On the other hand, wireless retransmission of data uses more energy (whose consumption increases as a function of distance), but does not require any physical intervention to retrieve data, device failure notwithstanding.

In order to send commands to the node, due to non-standard baudrate (800 bits per second), the non-standard node reception frequency (935 MHz) and the requirement to keep RF energy available when no messages are being sent (RF powering of the node), an SDR-based "front-end" solution was developed. The schematical representation of this system, with GPIB-based debugging instruments, is shown in fig. 101:

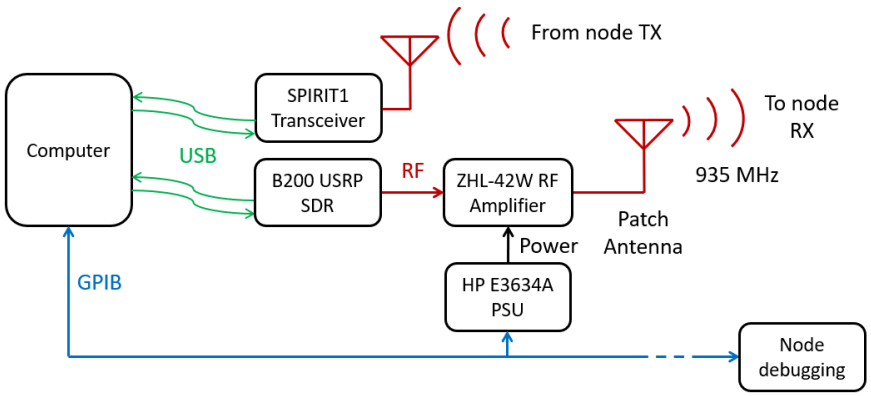

Figure 101 – Overview of the "front-end" of the node testbench.

The system is composed of a computer, capable of handling USB 3 and GPIB interfaces. The USB 3 interface is used in order to communicate with a B200 USRP, a software-defined radio (SDR) hardware platform. The output of the SDR is fed into a ZHL-42W amplifier, in order to transmit up to 30 dBm of power in the ISM band, in order to power the node when using RF powering only. The SDR is also capable of taking input from the computer to produce a RF CW carrier, or apply an OOK/ASK modulation to the carrier. Subsequently, the output from the amplifier is fed to a 2.5 dBi patch antenna.

A GPIB interface is also present on the computer for two reasons. The first one is order to turn on or off the RF amplifier programmatically, should it be necessary for certain scenarios of operation or to shut off RF power. The second reason is in order to provide debugging facilities to monitor the node's operation, particularly during the development of node firmware. This includes the ability to measure voltages on the node of key parts of the circuitry, such as the storage element, the voltage output to the active part of the node, or the output of the RF/solar energy sources.

In order to easily configure the commands sent to the node, to visualize debugging data and to control the SDR, a graphical user interface (GUI) for the transmitter was made under MATLAB, fig. 102:

Figure 102 – GUI used in order to debug and to transmit data packets to the node.

The interface is composed into three main panels. The leftmost panel is used for several purposes. Firstly, it can configure the SDR and set the frequency of message retransmission in order to test scenarios of operation. It also sets the baudrate of the sent packets, and can change their parameters (polarity of the message, duty cycle of the OOK/ASK transmissions, and synchronization preamble length). Finally, it can also be used

to choose which message to send, in order to determine which action will be undertaken by the node.

The middle panel is used in order to display debugging data acquired from the GPIB interface, which, in this instance, includes the voltage level of the node's storage element, the voltage present on the output of the power harvesting rectifier, and the voltage level present on the output of the buck regulator which provides a regulated voltage to the digital section of the node. The rightmost panel is used in order to visualize a frame data sent to the SDR (raw I/Q samples), and to show what the message packet looks like before transmission.

The first iterations of this work had no retransmission capability, however later revisions include a 900 MHz ISM band, low-power wireless transceiver module. Fig. 103 shows a typical configuration of the "front-end" of the test bench of the node, where RF signals and power are generated, and subsequently sent to the node:

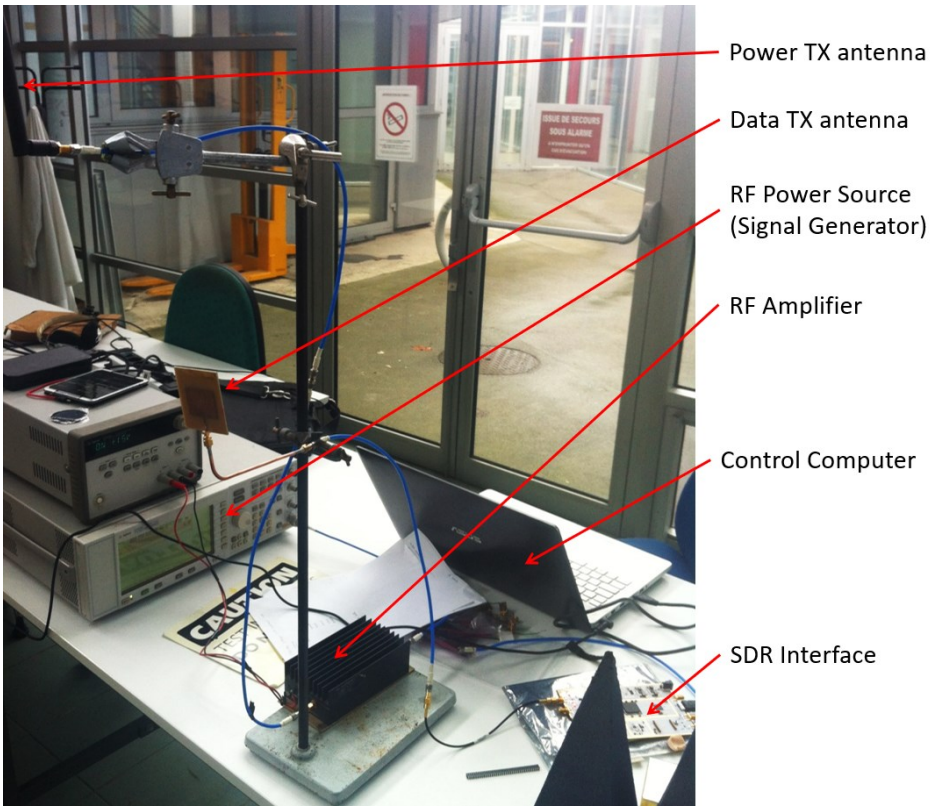

Figure 103 – Instance of the front-end of the testbench, where data is transmitted by SDR, and powering ensured by an RF signal generator.

Fig. 104 shows a schematical representation of the "back-end" of the test bench, where the actual node is located. It is placed on a mobile cart in order to change input RF power levels, and test the maximum distance at which in can operate.

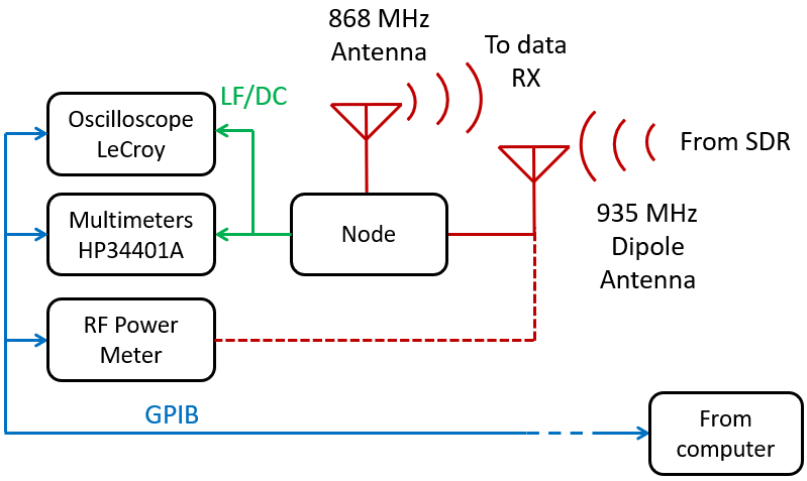

Figure 104 – – Overview of the "back-end" of the node test bench.

A typical configuration of the "back-end" of the node test bench, without data retransmission from the node is presented, with debugging equipment located below the node, fig. 105:

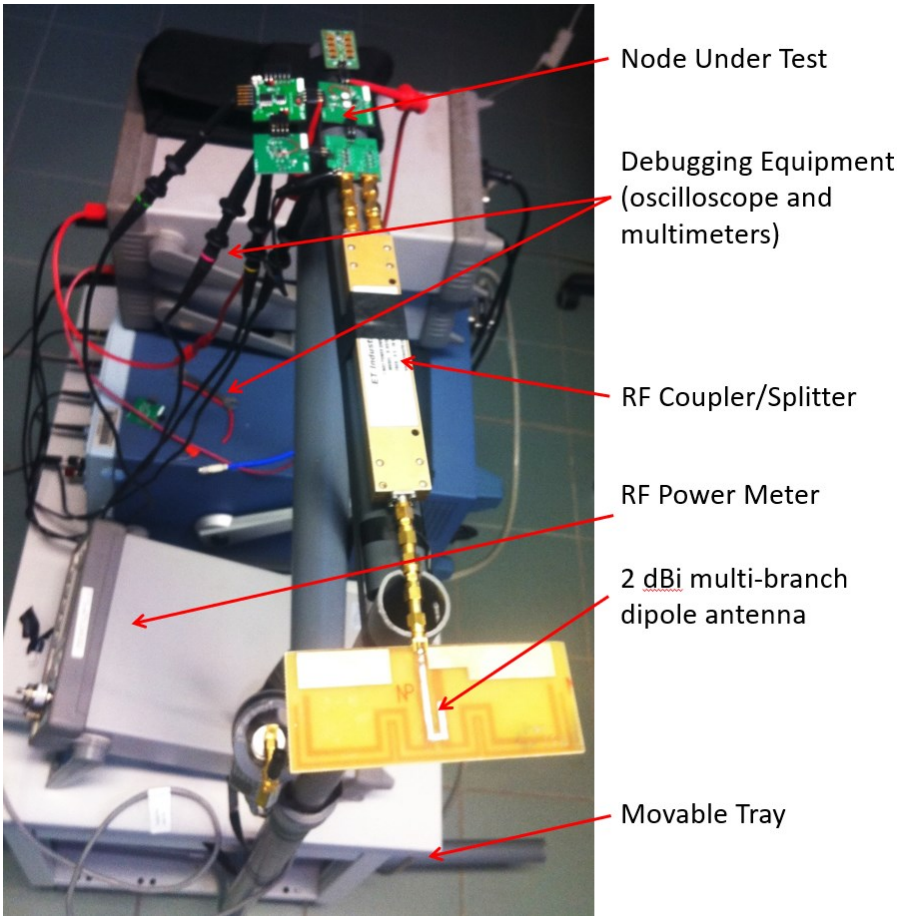

Figure 105 –Instance of the back-end of the testbench, presenting the node and various debugging accessories attached to it, along with RF reception antenna and coupler. The whole system is placed on a movable tray to ensure mobility.

Fig. 106 shows an example of the output of one of the debugging instruments on the movable tray, an oscilloscope. Signals on the screen show the reception of a data packet, as seen going through several parts of the node. The reception of the message (ASK modulation) through the rectifier can be seen in yellow, the generation of wake-up and data signals in purple and blue, respectively, and in green is a debugging signal, indicating when the microprocessor has finished receiving the message.

Figure 106 – Example of a signal outputted by the node during a message reception sequence, as captured by the oscilloscope.

Section III.f – Scenarios of Operation

Multiple applicative scenarios were envisioned for the node, which can include data measurement, communication and maintenance tasks. The type of scenario that is operable can vary depending on the power source available, or the functional aspect desired. Using data in the previous two sections of this chapter, results are theoretically calculated, in order to compare the simulated results to the actual power consumption as measured in this section.

For all of the scenarios, the storage elements will be charged to a maximum of 4 V. The bq25504 and bq25507's hysteresis voltages are set to 2.2 V for the shut-off and 2.5 V for turn on, in order to have a safety margin to avoid re-entering cold-start mode, once successfully in warm-start mode.

A data measurement operation is defined as the sequential combination of a temperature measurement command with an FRAM write command. Likewise, a data transmission operation is defined, sequentially, as an FRAM read command combined with a data transmission command. Certain scenarios have not been measured in situ, however the power consumption of the devices, during their various states of operation, have been measured, and appropriately implemented within the simulator.

As the time taken to process a command sent to the node is approximately 150 ms (spent mostly in the reception and decoding received packets via the wake-up radio), the maximum speed at which the node can receive commands is approximatively at 6.67 Hz. This allows the wake-up generator circuit to recover properly between commands, and should be considered as the upper limit in terms of the number of commands the node can process in time.

Therefore, data measurement operations with this node are limited to a maximum speed rate of 6.67 Hz, and data transmission operations, as they require two received packets, are limited to a maximum speed rate of 3.33 Hz.

Subsection III.f.1 – Scenario 1 – Continuous RF Operation

Continuous RF operation of the node is defined as powering it through a continuous RF signal, on which any data transmission to the node will be superimposed. The bq25504 (power management IC dedicated to solar harvesting) will be considered to be non-

operational in scenario and will not consume any energy. The storage element for this scenario is a 3720 µF ceramic capacitor-based element.

The main criterion of the scenario is to evaluate the performance of continuous operation of the node. This is done by evaluating the speed at which a measurement command can be sent, without the main storage capacitor discharging. This will depend on the RF power provided to the node by the source.

This scenario is divided into two sub-scenarios: during the first one, the node will operate in RX only mode, where the only instructions it will receive are that of data measurement and storage; during the second one, in addition to RX mode, it will also send back the data using the data TX module.

Subsubsection III.f.1.i – RX Only Mode

Simulated and measured results are presented in fig. 107:

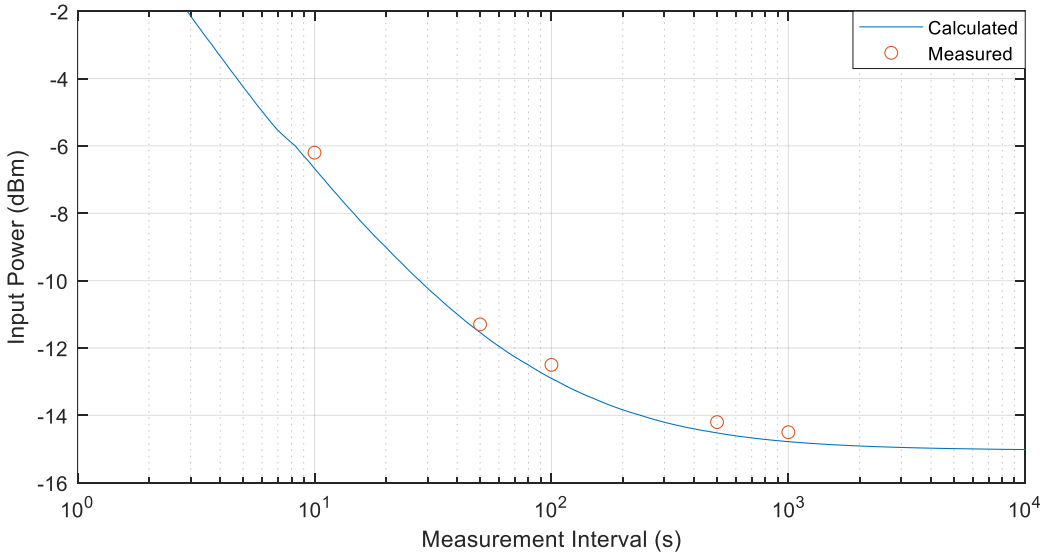

Figure 107 - Maximum operation speed of the node as a function of input power, with a 3720 µF ceramic capacitor-based storage element, for data measurement operations.

Measured measurement intervals were done at intervals of 10, 50, 100, 500, and 1000 seconds. Using these intervals, the node requires, respectively, -6.2, -11.3, -12.5, -14.2, and -14.5 dBm of input power in order to remain operational.

As the frequency of measurements becomes increasingly close to the theoretical 3.33 Hz limit, the amount of power required to maintain the node operational increases rapidly. The theoretical limit of 3.33 Hz cannot be reached, as this would require more instantaneous

energy than the rectifier can provide, 10 mW, if it is supposed that a maximum input power of 0 dBm is available for this scenario. As the interval between measurements increases, the power level trends towards the hard limit of -15.1 dBm, which represents the minimum amount of power required to maintain the node functional in sleep mode.

In regards to the difference between measurements and theoretical predictions, the higher levels of power that are required as the frequency of measurements increases are probably due to cumulated interaction of inefficiencies (buck converter, MPPT out of range as power input levels increase…) in the node as power consumption rises. These inefficiencies that were not present when characterizing the individual modules for the simulator likely only occur when all modules are associated together.

Subsubsection III.f.1.ii – RX and TX Mode

Similarly to the first part of the scenario, the node is now be told to perform a data measurement operation, followed by a data transmission operation for each instruction. This will reduce the effective maximal frequency rate of measurements down to 1.67 Hz. Simulated and measured results are presented in fig. 108:

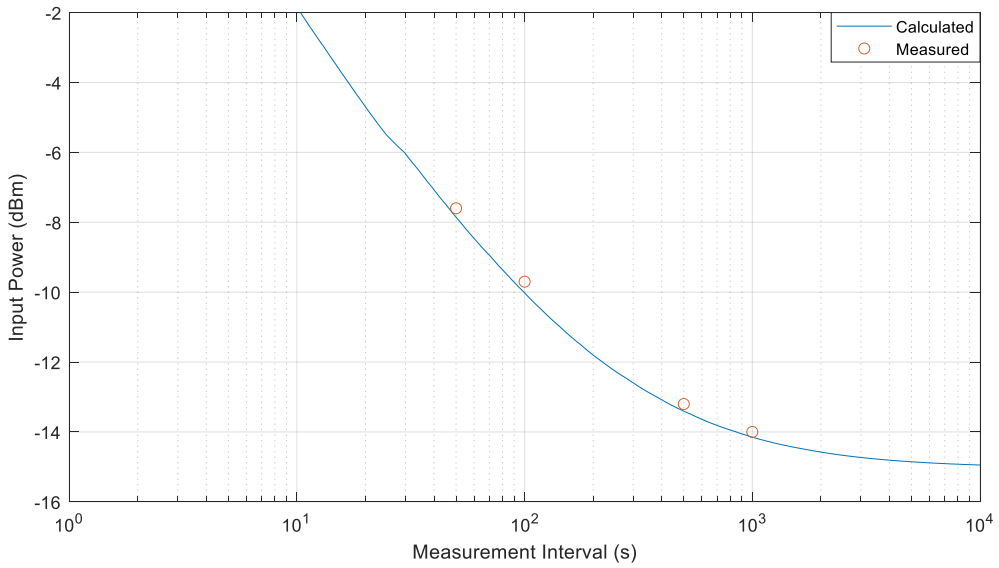

Figure 108 - Maximum operation speed of the node as a function of input power, with a 3720 µF ceramic capacitor-based storage element, for data measurement and transmission operations.

With the same measurement intervals as the previous sub-scenario, 10, 50, 100, 500, and 1000 seconds, the node requires, respectively, -1.9, -7.6, -9.7, -13.2, and -14 dBm of input power in order to remain functional.

The node is restricted to larger measurement intervals, compared to the previous sub-scenario, in order to remain operational at the same power levels. This is due to the power consumption of transmission operations, which are nearly an order of magnitude higher than any reception and measurement only operations. Operation is still possible with only RF power, albeit near real-time operation will be hindered.

Subsubsection III.f.1.iii – RX and TX Mode with Multiple Sensors

It may be of interest to increase the number of sensors present on the node in order to collect more data from its surroundings. This part of the scenario will analyze the additional power consumption, and therefore, power requirements that will be expected of the node by adding one or more environmental sensors, and evaluate the feasibility of implementing such a system in real life, by determining the maximum operating distance of the node from a RF power source.

The sensors that will be used are the Si7050 temperature sensor, the MS5837-30BA pressure sensor, and the SM351LT analog magnetometer, whose power consumption has been characterized in previous work [82]. It will be assumed that each additional sensor adds one byte to the message retransmitted to the requester.

The results of the simulations show the different amount of input power required depending on the number of sensors actively attached to the node, fig. 109:

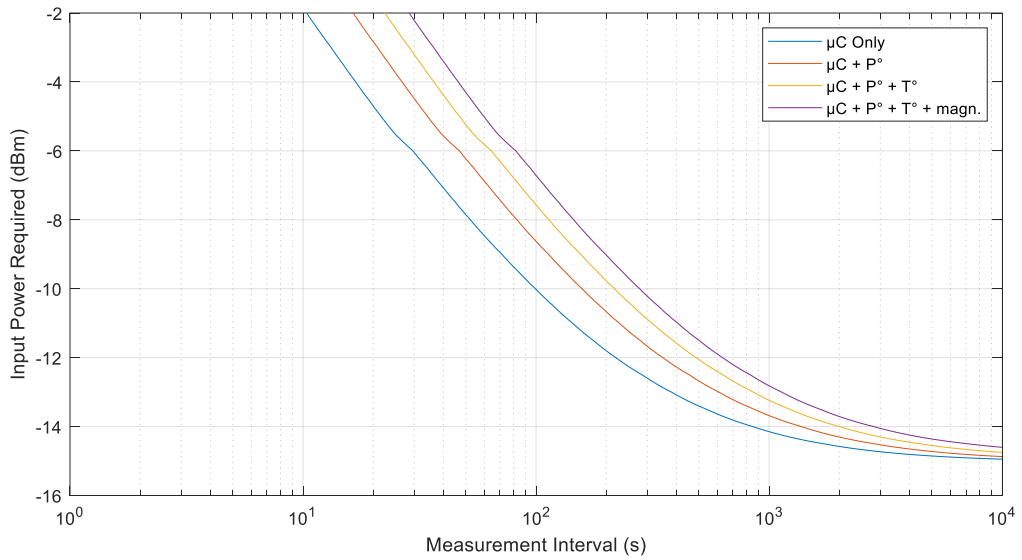

Figure 109 – Maximum operation speeds of the node, with a 3720 µF ceramic capacitor-based storage element, for data measurement and transmission operations with additional sensors.

The more sensors that are added, the more power is used during a measurement operation, as multiple sensors not only consume more energy during a measurement, but because the retransmitted message length increases in order to accommodate for more data. It can also be noted that with the increase of quiescent current, the minimal input level of power required to maintain the node operation increases with added sensors.

Assuming an RF source powering the node with a nominal output power of 28 dBm, the amount of power available to the node is estimated using the free-space path loss (FSPL) formula, with A_{dB} the resulting loss in dB, d the distance between the source and the node, f the frequency of the RF power source, c the speed of light, and $GAnt_{RX,dB}$, $GAnt_{TX,dB}$ the gain of the RX and TX antennas, respectively.

$$A_{dB} = 20log_{10}\left(\frac{4\pi df}{c}\right) - GAnt_{TX,dB} - GAnt_{RX,dB}$$

Table 14 illustrates the maximal frequency of operation, depending on the distance at which the node operates, depending on the number of sensors present.

Maximum Measurement Interval				
	Distance (m)			
	1	2	5	6
µC only	< 10 s	21 s	344 s	1505 s
µC and P° sensor	< 16 s	33 s	549 s	2445 s
µC and P°, T° sensors	< 23 s	46 s	670 s	3835 s
µC and P°, T°, magn. sensors	< 28 s	58 s	1012 s	5900 s

Table 14 – Maximum operation frequency depending on the node distance and configuration.

It can therefore be noted that, as the number of independent sensors on the node increases, that the frequency at which the node can operate decreases rapidly. If all three sensors are used, then the node's measurement frequency decreases by approximatively 65 % compared to no external sensors used, almost independently of the power level required for operation. Therefore, when possible, it is important to minimize the number of sensors used on the node, and to prefer more integrated solutions in terms of environmental sensing.

Subsection III.f.2 – Scenario 2 – Fully Autonomous Operation

Autonomous operation of the node, defined as having the node operate without a power source, would require at least a day's worth (or more) of energy storage. Therefore, it is necessary to use a supercapacitor for energy storage requirements, in order to power the circuit during sleep mode, and support any measurement operations.

This scenario uses a 470 mF capacitor, pre-charged to 4V, for 30 minutes, using a standard power supply, in order to minimize leakage currents of the former. Afterwards, it is hot plugged into the bq25504 circuit. No power, whether it be solar or RF energy, is given to the device. Both the bq25570 and the bq25504 operated in WS mode during the length of the scenario. The main criterion to evaluate the performance of this scenario is to determine how long the node can operate with main storage supercapacitor discharging, and without a power source. The autonomy will depend on the frequency of measurements and the discharge rate of the supercapacitor.

The discharge time of the node was measured to be 2.25 days, without any measurement commands sent to it. This is considered to be the best-case scenario, as the energy drain is only supercapacitor self-discharge, and the quiescent current of the circuit in sleep mode. The worst-case scenario, on the other hand, is when the node is nearly-continuously solicited with data measurement and transmission requests.

Subsubsection III.f.2.i – RX Only Mode

Simulated and measured results are presented in fig. 110:

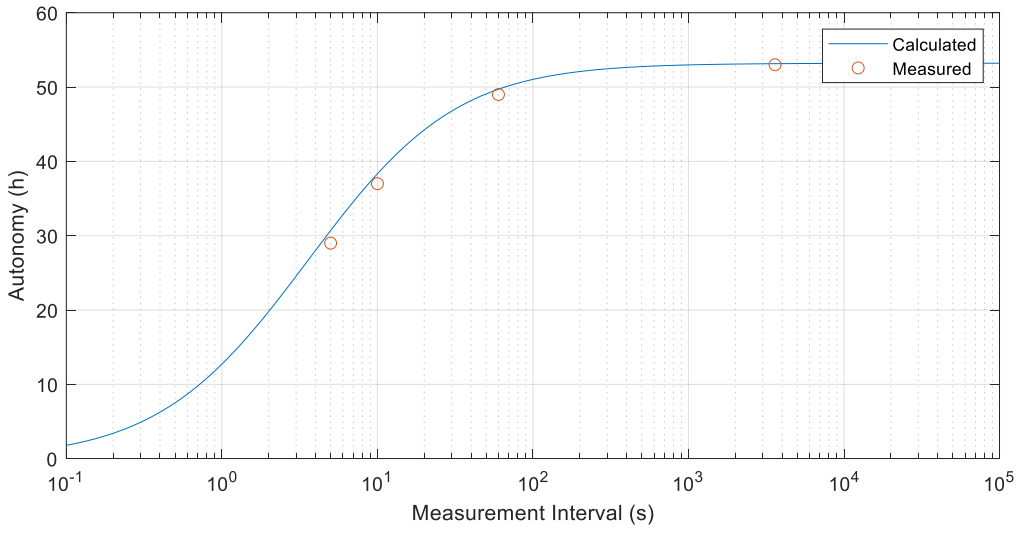

Figure 110 - Autonomy of the node in RX mode, depending on the measurement interval.

With measurement intervals of 5 s, 10 s, 1 min, 1 hour, and 2.8 hours, the autonomy of the node is, respectively, 29, 37, 49, 53, and 53 hours. This is similar to, but slightly less efficient than simulations. As the measurement frequency increases, the autonomy of the node decreases. However, with a measurement every ten seconds, the node can still have an autonomy of 37 hours. If the node is never solicited, its autonomy is approximatively 54

hours. This upper limited is the best-case scenario initially measured, i.e., when the node is in sleep mode and the supercapacitor is self-discharging.

It can be noted that as measurement intervals increase to be longer than one hour, the static power consumption of the system, including the storage element's leakage current, overtakes that of the power used during normal operations, and therefore the autonomy varies little past this measurement interval. Using a larger supercapacitor, or higher maximum storage element voltages, would increase the autonomy of the node. However, larger storage elements would come at a cost of longer cold start times.

For longer autonomy requirements, it may be necessary to implement a cold start charge method that will rapidly kick-start the system into warm start mode, which may use existing energy harvesting methods (i.e., leave the node under a very bright light, or leave the node next to a high-power transmitter, until it indicates that it is operational) or implement a cable-based solution.

Subsubsection III.f.2.ii – RX and TX Mode

Simulated and measured results are presented in fig. 111:

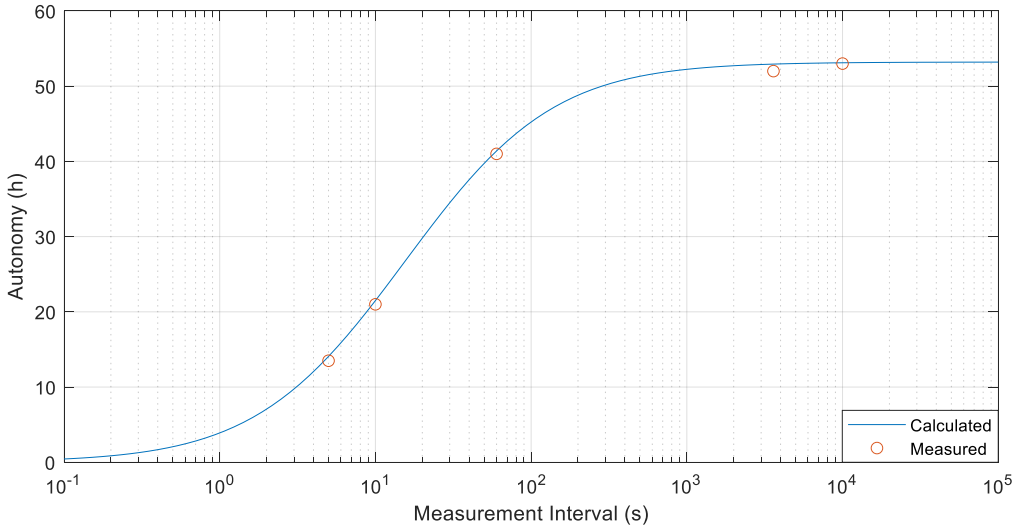

Figure 111 – Autonomy of the node in RX/TX mode, depending on the measurement interval.

With measurement intervals of 5 s, 10 s, 1 min, 1 hour, and 2.8 hours, the autonomy of the node is, respectively, 13.5, 21, 41, 52, and 53 hours. The autonomy of the node has decreased compared to the previous sub-scenario, due to the high energy consumption of data transmission operations. However, if the measurement requests are spaced out to be over an hour away each, the node still presents similar autonomy as the RX-only sub-scenario.

Subsubsection III.f.2.iii – Daily Burst Transmission

For an IoT node, frequently repeated transmission of measured data can be necessary in order for the node to accomplish its goals. For instance, in a scenario where a node is used to indicate meteorological conditions to a user during the day, frequent measurement intervals would be expected by the end user. However, in certain applications where real-time or near-real-time data is not required, it may be more power efficient to automatically measure the data, and then to transmit it in bulk once daily, using the storage capabilities of the node to temporarily store the data.

The main objective of this scenario is to analyze the autonomy of the node, as a function of the amount of data measured, with a daily burst transmission of equivalent length, and to compare it to the previous autonomous RX/TX scenarios. The node will no longer require a command for each measurement, and will instead use a periodic interrupt generator device, the TPL5010 [83]. This component uses approximatively 35 nA of quiescent current during operation. It will be assumed that, should the node run out of power before a daily transmission is timed, that is will send the data it has collected for the last day before shutting off.

Results of the simulation are presented in fig. 112:

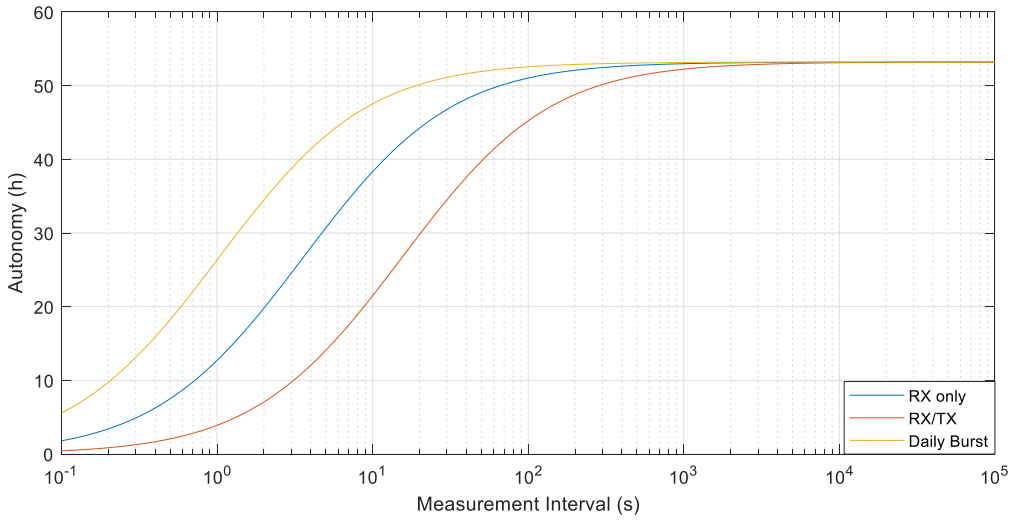

Figure 112 – Daily burst transmission scenario, depending on measurement frequency.

The autonomy of the node, although still limited to the hard-limit created by the supercapacitor leakage current, presents a greater autonomy than both previous sub-scenarios. This is due to the fact that, as messages are no longer transmitted for measurement operations, no energy is spent decoding them. Grouping daily data into a single packet

increases the efficiency of data TX power consumption, reducing when data packets are longer, decreasing the energy spent per bit transmitted.

The autonomy of the node remains the same, independently of the transmission/reception combination, at 53 hours. As previously shown in figure 111, the RX/TX performance presents the worst-case autonomy, due to the energy consumed for both the reception of a request, and the transmission of information as a result. As seen in figure 110, the RX-only performance is better, as no data is transmitted.

However, it can be observed that be best case for this scenario is the daily burst transmission. Although the node spends a significant amount of energy sending data, as the measurement itself is autonomous with the addition of a periodic interrupt generator, the energy saved by avoiding repeated requests for data can be allocated instead to transmission. Furthermore, as the node only sends information once a day, the efficiency per bit sent is lower than in the case of repeated TX/RX requests. It should be noted, on the other hand, that daily transmission of data impedes timely demands for data. This mode of operation should be privileged only if timely reception of the measurements is not required.

Subsection III.f.3 – Scenario 3 – Solar Operation

Solar energy, although primarily designed to collect energy from the sun in an outdoor setting, can easily provide sufficient energy to power the node, due to its extremely low consumption. Even in low-luminosity settings, photovoltaic cells, although operating at reduced efficiency themselves, can still collect milliwatts of power, which is sufficient to both power the node and store energy.

The main criterion for this scenario will be to analyze the amount of luminosity required in order to recharge the node during the day, assuming that it will be operated exclusively during the night. In regards to the duration of a day, a worst-case of 8 hours of light, and 16 hours of darkness will be contemplated. Furthermore, it will also be assumed that the node will always be operating in warm start mode. Just as the previous scenario, two sub-scenarios will be envisioned: a RX only mode, and a RX/TX mode.

Fig. 113 shows the amount of time required for the node to charge from the beginning of warm start mode, until the storage element (supercapacitor) is full as a function of luminosity and LED type, supposing that the node is not solicited.

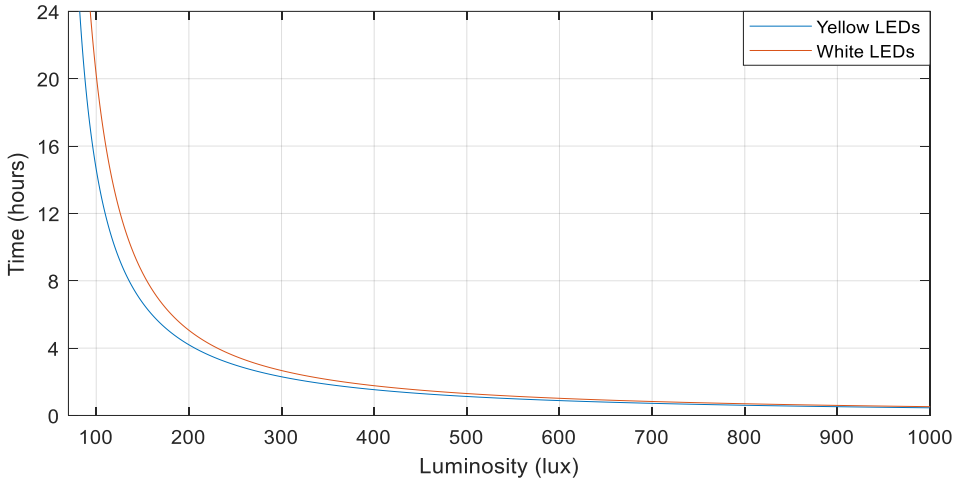

Figure 113 – Warm-start charge time, as a function of luminous intensity, for both LED types used in this work.

It can be inferred that, for the white LEDs, at least 155 lux of luminosity is necessary in order to recharge the node in 8 hours. On the other hand, for the yellow LEDs, 135 lux is required for the same 8-hour charge time. This scenario assumes that the node's storage element is at the shutoff level in terms of the warm start mode (2.2 V), but is not completely discharged or in cold-start mode.

Indoor luminosity levels can vary from 300 lux to 500 lux in a typical indoor setting at an office or a place or residence. Therefore, if the node is exposed directly to ambient lighting, operation is possible as long as lights are on at least 2 to 4 hours a day, which is likely in such surroundings. However, if the node is only exposed indirectly to light, reliable operation may be problematic.

In this scenario, if it is assumed that the node is solicited at night, then 16 hours of autonomy are required. From fig. 110 and fig. 111, from the previous autonomous scenario, it can be determined that the node must not receive commands more than once every 1.5 seconds and every 7 seconds, respectively, for RX and TX/RX operations, in order to maintain operation in warm start mode. Therefore, it can be concluded that the node may operate in environments with luminosity levels as low as 150 to 200 lux for an indefinite amount of time, with reasonable environmental sensing capabilities available.

Section III.h – Conclusion

This chapter has presented an analysis of the node, by demonstrating its modular design and power consumption. This data is further used in order to create a simulator, which is then used to simulate the power consumption of the node under different scenarios, where a scenario is one of the operating modes of the node which can be programmed, or is programmed, into it. The hypothetical results from the simulator are shown for a number of scenarios, out of which a select number have been experimentally verified.

With continuous RF operation, the node is capable of operating at power levels down to -15.1 dBm, which is a hard limit based on its quiescent power consumption. Operation is still possible every minute, with power levels of -13 dBm and -11.5 dBm for RX and RX/TX operations, respectively.

Operation at higher speeds, although theoretically possible, is limited in practical terms, due to the amount of RF power required, which may not be available in practice due to emission limits, coupled with the distance of the node from the power source. The addition of multiple sensors also increases the minimal amount of power required for operation, as well as the amount energy used for the storage or retransmission of measured data, by approximatively +3 dB if multiple sensors are used.

The node presents a maximum autonomy of 53 hours, and can operate at diverse measurement intervals, depending on the application. The use of either RX or RX/TX operations is energy intensive, as communications overhead solicits the node heavily. With a measurement every second, the autonomy of the node is 12 hours and 4 hours for RX and RX/TX operation, respectively. The addition of a daily burst mode, however, increases this autonomy to 24 hours, albeit reducing data reception latency.

Solar operation is also possible with luminosity levels down to 135 lux, assuming light is repeatedly available for 8 hours a day. Practically, if the node has access to sunlight or direct indoor illumination for this duration, then continuous operation is possible indefinitely. This, however, is dependent on the reliability of devices within the node, which can fail (i.e., supercapacitor recharge cycles…).

Results from measurements indicate that the node operates correctly within its design parameters. Furthermore, hypothetical scenario predictions closely match measured data,

which indicates that for the current iteration of the node, the simulator is at least accurate for the scenarios that have been measured.

Finally, the test bench of the node is also presented, in order to demonstrate how data is measured, as well as to show how different elements of the test bench interact in order to collect data.

Chapter IV

Conclusion and Perspectives

This page intentionally left blank.

Chapter IV Conclusion and Perspectives

Section IV.a – Introduction

This chapter will conclude this work. Firstly, the node's performance and associated metrics will be compared and analyzed with other work currently in the same domain. Then, possible improvements to the node, and discussion of possible future research, will be discussed. Finally, a brief conclusion overviewing the whole work will be presented.

Section IV.b – Comparison to Other Works

Due to different topologies and solutions used in various works in the same domain, table 15, it is difficult to compare such work homogeneously and to determine appropriate metrics for comparison. However, it is possible to present all the different categories of other systems, and determine how the node is situated within these.

	Energy sources	Freq. (Gain)	Performance (Efficiency, Sensitivity…)	Type	RF RX/TX?	Load
This work	RF/Light	900 MHz ISM (2 dBi)	**RF:** 6.3 µW, 20 % @ -15 dBm **Solar:** 250 µW, 2.2 % @ 500 lux **Both:** Up to 3.0 mW	COTS	RX/TX	µC (PIC), FRAM 2x PMU (bq255XX) RF Transceiver Sensor(s)
Nikotiaki [84]	RF/Light	2.4 GHz ISM (~2 dBi)	**RF:** <15 % @ -15 dBm **Solar:** 830 µW @ 100 W/m^2 **Both:** Up to 1.5 mW	COTS	*RX/TX*[1]	PMU (bq25504) *µC*[1] *RF Transceiver*[1] *Sensor*[1]
Bito [85]	RF/Light	2.4 GHz ISM (7.4 dBi)	**RF:** 23 % @ -15 dBm **Solar:** 200 µW @ 500 lux **Both:** Up to 80 µW	COTS	*RX/TX*[1]	PMU (bq25504) *µC*[1]
Collado [86]	RF/Light	800 MHz - 2.5 GHz (~2 dBi)	**RF:** 20-25 % @ -15 dBm **Both:** 25-300 mV @ 0-20 dBm, 150 W/m^2 (no load)	COTS	-	-
Georgiadis [87]	RF/Light	900 MHz RFID	**Both:** 58-62 % @ >24 dBm Addition of solar panel does not degrade energy transfer.	COTS	RFID	Class E Oscillator
Sample [88]	RF/Light	900 MHz RFID	Solar panel permits operation indoors w/o reader, increases RFID tag range when read w/reader.	COTS	RFID	WISP 4.1 or RFID IC
Usami [89]	RF/Light	1 GHz	**Both:** 26% @ -17 dBm, 10 mW/m^2	ASIC	-	-
Piñuela [10]	Multi-RF	UHF DTV, 2G, 3G (~4.5 dBi)	**RF:** 10-40% @ -30 to -10 dBm **All:** Operation down to -29 dBm	COTS	-	PMUs (bq25504)
Vyas [90]	RF	Multi-Channel UHF DTV (7 dBi)	**RF:** 22% @ 400 µW RF power	COTS	-	µP (PIC) PMU
Bito [91]	RF	2.4 GHz ISM	**RF:** 17.6% @ -20 dBm	COTS	-	Custom solar-powered RF-boosting PMU
Karolak [49]	RF	900 MHz, 2.5 GHz ISM (2 dBi)	**RF 900 MHz**: 70% @ -20 dBm^2 **RF 2.4 GHz:** 68% @ -20 dBm^2	ASIC	-	-
Roberts [92]	RF	2.4 GHz ISM	**RF:** Operates from -7 dBm	ASIC	RX	Wake-up radio

[1] Theoretical (unimplemented) load/functionality.
[2] Inductive antenna matching.

Table 15 – Overview of different nodes and associated metrics.

Novel aspects of this work include the use of both RF and solar power sources to power a fully-functional IoT node, with data retransmission. This node is capable of both receiving and responding to commands. Furthermore, if required, and if possible, it can retransmit data. A custom-based interface using SDR was also created for sending commands to the node.

A power consumption simulator is also created, based on measured performance data, and is compared with rea, in-situ measurements. Although most of the models describing the devices are empirical in nature, theoretical predictions and real data match closely. The simulator can be used to create and test other hypothetical scenarios before they are implemented. This can be used to test these scenarios' viabilities, before requiring measurements to be undertaken.

Most RF to DC conversion circuits exhibit similar performance, with power input ranging from -30 dBm up to 0 dBm, with efficiencies varying down from 10% up to 70%, depending on the application or use case scenario of the circuit. The frequencies at which RF power is harvested are relatively diverse, ranging from the UHF band (500 MHz) up to the 2.4 GHz ISM band. Power provided by RF power harvesting can range from down to 500 nW, up to several hundreds of milliwatts, depending on the proximity of the energy source to the node. Similarly, solar harvesting is implemented at various illumination levels, ranging from low-light indoor environments up to full sunlight. Power output from solar modules ranges from several dozens of microwatts up to several milliwatts.

Combining solar and RF power harvesting (or any multi-source power harvesting system) can be done in several ways. The method chosen by this work was to implement one power management unit (PMU) per source, and to combine them at the energy storage level. It is however possible to daisy chain sources together in series (or in parallel), such as in [10], [84], [86] and [89]. However, this may cause undesired interactions of each source with each other, especially with MPPT. Generally these can be controlled and mitigated against by determining the optimal way to connect and manage the power sources. However, in certain instances, series implementations can actually increase the minimum level at which RF power can be scavenged [10]. Adding solar harvesting also presents an advantage for systems such as RFID tags, as this permits the tag to be operational when not associated or next to a tag reader. For the most part, the addition of solar panels near an antenna does not affect the antenna's performance.

Most COTS systems are similar in size, ranging from several cm^2 to approximatively 500 cm^2 in diameter. Several systems are entirely flexible, such as [86]. ASICs, of course, remain the smallest of systems; however, the antenna must be externally supplied at typical operating frequencies.

Section IV.c – Future Perspectives

Although the node operates satisfactorily, it is always possible to improve different aspects of the node. Increased autonomy results in improved robustness, should non-ideal powering situations occur. Lessened power consumption is desired to reduce powering requirements. Smaller component footprints or higher integration could be implemented in order to make the node smaller. Increased efficiency could be achieved using more specialized integrated circuits or systems.

Many of the limitations of this node are due to the use of COTS components. COTS circuits are generally required to be generic, as opposed to specialized, which is often traded-in at the cost of efficiency. This is because COTS components are manufactured on a scale, and are only made if a sufficient market exists to commercialize them.

It is difficult to further increase the efficiency of the rectifier, as most modern iterations of COTS diodes are mature [93]. Furthermore, at very low input power levels, from -20 dBm downwards, the theoretical efficiency for COTS Schottky diodes reaches theoretical limits, due to diode forward voltage and associated semiconductor effects. However, the study of rectification in the microwave domain is still active [94]. Further improvement could also be made as better semiconductor processes become available, or different rectifier technologies become commonplace. Matching also remains elusive and difficult to scale, due to the high capacitance of diodes.

Solar power harvesting provides plentiful amounts of energy for nodes requiring little energy, such as in this work. However, the solar panel still remains one of the largest elements in the node. Improvements in solar power harvesting could be obtained by using more efficient solar panels, which exist [53]. These would be more expensive due to their manufacturing process, but would require a smaller surface area for an equivalent amount of power output, efficiency notwithstanding. Solar panels optimized for indoor usage can also be used [95].

The bq22570 and bq25504 power management ICs are being at or below their limits in terms of energy and voltage inputs. It is therefore unsurprising that they do not always provide highly-efficient energy transfer, which can easily triple the static energy consumption in sleep mode, or cause long cold-start charging times. This could be mitigated by using

custom-designed power management ICs, or by using extremely low-power techniques to create equivalent replacements [91], [96].

Radio demodulation suffers from two main problems. The first is that of false wake-ups. Indeed, due to the presence of other transmissions in the 900 MHz ISM band, and sometimes even due to objects moving in the node's environment, false wake-ups are sometimes triggered, costing the node valuable energy. Generally, this is resolved by using different modulations. The destruction of phase information in the RF carrier by the rectifier restricts RF signals to convey information using amplitude modulation only. However, the use of correlation or other techniques can possibly change this situation, so long as power consumption remains minimal, such as in [97]. Likewise, RF transmission is problematic due to power consumption, the use of more specialized and low power-consuming circuits can remain of interest [98].

Although the microprocessor remains versatile, the decoding of messages uses high amounts of energy, due to the software-based implementation of the Manchester decoding algorithm. Migration from a microcontroller to a more application specific ASIC could resolve this problem.

Although the node is not excessively large, modularity requires the use of connectors, which use significantly more PCB area. This problem can be mitigated as the node matures and functionalities become "locked-in", in which case a compact board can be manufactured with all components closely spaced together. Further integration can be realized by rendering different energy sources inter-compatible, such as combining the rectenna and the solar panel as one, or directly integrating the node onto the solar panel and/or rectenna, such as in [86].

Although the simulator performs adequately, it is currently command-line based only and uses a functional programming paradigm. Parameters orchestrating the operation of scenarios must be hard-coded into the code. Further improvements in this domain could include giving the simulator a GUI, and implementing the code in an object oriented language could make the creation of more complex scenarios of operation possible without requiring excessive amounts of effort. An interesting addition would be to integrate randomness to certain scenario parameters, in order to account for possible variations in the node's environment.

Further improvements could be implemented by developing more advanced models, based on more extensive measurements. It could be possible to use manufacturer models, however their availability is restricted. This would further be complicated by co-integration with other simulators (SPICE…) in order to obtain desired results, and would require longer simulation times due to increased complexity.

The test bench operates correctly, and is relatively easy to use thanks to its GUI. However, performance is not particularly satisfying, especially in regards to the control of the SDR. Generation of SDR waveforms is also simplistic, and could be expanded upon by implementing more sophisticated modulation schemes and parameters.

Section IV.d – Conclusion

The purpose of this work was to analyze the feasibility of implementing and powering an IoT node with currently existing components "off the shelf" (COTS), using RF and/or solar power harvesting. It was possible to characterize several different modules of this node, with theoretical considerations and implementation details, and determine how they performed as a whole. It can be seen the node operates correctly at a distance of up to several meters with typical RF powering settings for the 900 MHz ISM band. RF Powering is capable of providing up to 400 µW of power, though values around 20-30 µW are more typical. Solar powering can provide at least 2.5 mW of power in broad daylight, and around 100-200 µW in ambient, indoor lighting conditions.

The node is capable of environment sensing with a restrained power budget. The active section of the node consumes 920 nW of power in sleep mode, of which 870 nW is used for the wake-up circuitry. The system is fully operational, and able to handle both communications and RF energy transfer over the same band. It may also operate over a period of one or two days, with the presence of a supercapacitor as a storage element in an autonomous scenario. Additionally, the node is capable of wirelessly transmitting back data when requested to do so.

During RF-only power operation in the 900 MHz ISM band, the device functions with RF power levels down to -15.1 dBm, though a cold-start power level of -13.1 dBm is required. When using solar energy, the device may function with continuous luminosity levels down to 70 lux, albeit with a cold-start requirement of 100 to 150 lux, depending on the leakage current of the supercapacitor storage element. Notably, indefinite solar operation in indoor environments is possible, with only 8 hours of solar harvesting per day, albeit this requires slightly higher luminosity levels of 135 lux.

Various operational scenarios that IoT nodes could be used in were also considered, giving an additional insight into the abilities and limitations that are possible in a small subset of potential operating environments. Besides an overview of different modes of operation, at the system level, an empirical simulation tool was also developed, based on the analysis and characterization of the modules featured in the proposed hybrid node. The resulting simulations exhibit a good correlation with actual measurements, thus allowing for prediction of the node's performance in various environments, or other hypothetical scenarios.

Furthermore, a software-defined radio interface is also developed in order to aid data collection. The resulting test-bench was also partially automated, permitting an easier measurement and analysis cycle for different modules. This is a result of the node's modular design, with permits rapid feedback once different modules were modified or upgraded as this requires additional data.

This page intentionally left blank.

References

[1] GEC Designs, 2020. Different Domains Of The Iot. [image] Available at: <https://gecdesigns.com/img/blog/iot/iot-02.jpg> [Accessed 30 October 2020].

[2] A. A. Khan, A. Mahmud and D. Ban, "Evolution From Single to Hybrid Nanogenerator: A Contemporary Review on Multimode Energy Harvesting for Self-Powered Electronics." IEEE Transactions on Nanotechnology, vol. 18, pp. 21-36, 2019, doi: 10.1109/TNANO.2018.2876824.

[3] S. Roundy, D. Steingart, L. Frechette, P. Wright, and J. Rabaey, “Power Sources for Wireless Sensor Networks,” in Lecture Notes in Computer Science, Springer Berlin Heidelberg, 2004, pp. 1–17.

[4] L. Wald, “Basics in Solar Radiation at Earth Surface.” 2018. hal: 01676634.

[5] J. W. Stevens, “Optimized Thermal Design of Small ΔT Thermoelectric Generators,” presented at the 34th Intersociety Energy Conversion Engineering Conference, Aug. 1999, doi: 10.4271/1999-01-2564.

[6] Francioso, L., De Pascali, C., Farella, I., Martucci, C., Creti, P., Siciliano, P., & Perrone, A. (2010, November). Flexible thermoelectric generator for wearable biometric sensors. 2010 IEEE Sensors. 2010 Ninth IEEE Sensors Conference (SENSORS 2010), doi: 10.1109/icsens.2010.5690757

[7] R. Moghe, Yi Yang, F. Lambert, and D. Divan, “A scoping study of electric and magnetic field energy harvesting for wireless sensor networks in power system applications,” presented at the 2009 IEEE Energy Conversion Congress and Exposition. ECCE 2009, Sep. 2009, doi: 10.1109/ecce.2009.5316052.

[8] K. Tashiro, H. Wakiwaka, S. Inoue, and Y. Uchiyama, “Energy Harvesting of Magnetic Power-Line Noise,” IEEE Trans. Magn., vol. 47, no. 10, pp. 4441–4444, Oct. 2011, doi: 10.1109/tmag.2011.2158190.

[9] T. Beng Lim, N. M. Lee, and B. K. Poh, “Feasibility study on ambient RF energy harvesting for wireless sensor network,” presented at the 2013 IEEE MTT-S International Microwave Workshop Series on RF and Wireless Technologies for Biomedical and Healthcare Applications (IMWS-BIO), Dec. 2013, doi: 10.1109/imws-bio.2013.6756226.

[10] M. Pinuela, P. D. Mitcheson, and S. Lucyszyn, “Ambient RF Energy Harvesting in Urban and Semi-Urban Environments,” IEEE Trans. Microwave Theory Techn., vol. 61, no. 7, pp. 2715–2726, Jul. 2013, doi: 10.1109/tmtt.2013.2262687.

[11] E. Khansalee, Y. Zhao, E. Leelarasmee, and K. Nuanyai, “A dual-band rectifier for RF energy harvesting systems,” presented at the 2014 11th International Conference on Electrical Engineering/Electronics, Computer, Telecommunications and Information Technology (ECTI-CON), May 2014, doi: 10.1109/ecticon.2014.6839870.

[12] S. Mekid, A. Qureshi, and U. Baroudi, “Energy Harvesting from Ambient Radio Frequency: Is it Worth it?,” Arab J Sci Eng, vol. 42, no. 7, pp. 2673–2683, Sep. 2016, doi: 10.1007/s13369-016-2308-y.

[13] S. Roundy, P. K. Wright, and J. Rabaey, “A study of low level vibrations as a power source for wireless sensor nodes,” Computer Communications, vol. 26, no. 11, pp. 1131–1144, Jul. 2003, doi: 10.1016/s0140-3664(02)00248-7.

[14] R. J. M. Vullers, R. van Schaijk, I. Doms, C. Van Hoof, and R. Mertens, “Micropower energy harvesting,” Solid-State Electronics, vol. 53, no. 7, pp. 684–693, Jul. 2009, doi: 10.1016/j.sse.2008.12.011.

[15] F. Liu et al., “Acoustic energy harvesting using an electromechanical Helmholtz resonator,” The Journal of the Acoustical Society of America, vol. 123, no. 4, pp. 1983–1990, Apr. 2008, doi: 10.1121/1.2839000.

[16] J. Smoker, M. Nouh, O. Aldraihem, and A. Baz, “Energy harvesting from a standing wave thermoacoustic-piezoelectric resonator,” Journal of Applied Physics, vol. 111, no. 10, p. 104901, May 2012, doi: 10.1063/1.4712630.

[17] D. Carli, D. Brunelli, D. Bertozzi, and L. Benini, “A high-efficiency wind-flow energy harvester using micro turbine,” presented at the 2010 International Symposium on Power Electronics, Electrical Drives, Automation and Motion (SPEEDAM 2010), Jun. 2010, doi: 10.1109/speedam.2010.5542121.

[18] D. Vatansever, R. L. Hadimani, T. Shah, and E. Siores, “An investigation of energy harvesting from renewable sources with PVDF and PZT,” Smart Mater. Struct., vol. 20, no. 5, p. 055019, Apr. 2011, doi: 10.1088/0964-1726/20/5/055019.

[19] “2G, 3G, 4G LTE Network Shutdown Updates. “ Digi | IoT Solutions, Software, Products, Services for the Industrial IoT | Digi International. Last modified June 10, 2020. Available at: <https://www.digi.com/blog/post/2g-3g-4g-lte-network-shutdown-updates> [Accessed 2 November 2020].

[20] “What Are Near Field And Far Field Regions Of An Antenna?” Everything RF. [online] Everythingrf.com. Available at: <https://www.everythingrf.com/community/what-are-near-field-and-far-field-regions-of-an-antenna> [Accessed 2 November 2020].

[21] C. Mensink. "Wireless power and data over inductive links The technology for real ULP devices." AnSem BV. [online] Available at: <https://ulpc.nl/wp-content/uploads/2018/03/Clemens-Mensink.pdf> [Accessed 2 November 2020].

[22] “Power Density.” Radar Systems Engineering Handbook. RF Café. [online] Available at: <https://www.rfcafe.com/references/electrical/ew-radar-handbook/power-density.htm> [Accessed 2 November 2020].

[23] “Annexe 7 : Fréquences Utilisables Pour Certains Matériels De Faible Puissance Et De Faible Portée.” Agence Nationale des Fréquences. [online] Available at: <https://www.anfr.fr/fileadmin/mediatheque/documents/tnrbf/Annexe_A7.pdf> [Accessed 2 November 2020].

[24] W. Gilbert, “Guilielmi Gilberti Colcestrensis, medici londinensis, De magnete.” Excudebat Petrus Short, 1600, doi: 10.5479/sil.113709.39088016899940.

[25] “VIII. A dynamical theory of the electromagnetic field,” Phil. Trans. R. Soc., vol. 155, pp. 459–512, Dec. 1865, doi: 10.1098/rstl.1865.0008.

[26] A.-M. Ampère, “Théorie mathématique des phénomènes électro-dynamiques, uniquement déduite de l‘expérience.” Méquignon-Marvis, Paris. (November 1826).

[27] M. Faraday, “Description of an Electro-magnetic Apparatus for the Exhibition of Rotatory Motion.” Quarterly Journal of Science, Literature and the Arts 12,. London. (1821): 283–285.

[28] J. Maxwell, “VIII. A dynamical theory of the electromagnetic field,” Phil. Trans. R. Soc., vol. 155, pp. 459–512, Dec. 1865, doi: 10.1098/rstl.1865.0008.

[29] W. B. Carlson, “Tesla Inventor of the Electrical Age”. Princeton: Princeton University Press. (2015): 133–142.

[30] Ibid: 262–301.

[31] Brown, W.C. “The History of Power Transmission by Radio Waves.” IEEE Transactions on Microwave Theory and Techniques 32, no. 9 (September 1984): 1230–42. doi:10.1109/tmtt.1984.1132833.

[32] W. C. Brown, “The Microwave Powered Helicopter*,” Journal of Microwave Power, vol. 1, no. 1, pp. 1–20, Jan. 1966, doi: 10.1080/00222739.1966.11688626.

[33] R. Dickinson, “Evaluation of a High- Power Reception-Conversion Array for Wireless Power Transmission,” NASA-JPL Technical Memorandum 33-741, Sept. 1,1975.

[34] N. Shinohara, “Wireless Power Transfer via Radiowaves”. John Wiley & Sons, Inc., 2013. doi: 10.1002/9781118863008

[35] J. Valenzuela-Valdes, F. Luna, R. M. Luque-Baena, and P. Padilla, “Saving energy in WSNs with beamforming,” presented at the 2014 IEEE 3rd International Conference on Cloud Networking (CloudNet), Oct. 2014, doi: 10.1109/cloudnet.2014.6969001.

[36] S. Kundra, A. Dureja, and R. Bhatnagar, “The study of recent technologies used in E-passport system,” presented at the 2014 IEEE Global Humanitarian Technology Conference - South Asia Satellite (GHTC-SAS), Sep. 2014, doi: 10.1109/ghtc-sas.2014.6967573.

[37] Sun-Jin Kim, Jung Hae Seo, Jonnalagadda Krishna, and Sun-Joong Kim, “Wireless sensor network based asset tracking service,” presented at the Technology, Jul. 2008, doi: 10.1109/picmet.2008.4599893.

[38] M. Siciliano, “The ICAO MRTS Programme.” International Civil Aviation Organization. [online] Available at: <https://www.icao.int/Meetings/mrtd-Zimbabwe2012/Documents/1-Siciliano_MRTD-Standards.pdf> [Accessed 4 November 2020].

[39] L. Ayre, “Library RFID systems for identification, security, and materials handling.” Library Technology Reports. 48. (2012). p. 9-16.

[40] A. Price, “Tags, RFID and the Internet of Things.” E-tech News, no. 05/2017 (2017). [online] Available at: <https://etech.iec.ch/issue/2017-05/tags-rfid-and-the-internet-of-things> [Accessed 6 November 2020].

[41] J.-R. Lin, T. Talty, and O. K. Tonguz, “Feasibility of Safety Applications Based on Intra-Car Wireless Sensor Networks: A Case Study,” presented at the 2011 IEEE Vehicular Technology Conference (VTC Fall), Sep. 2011, doi: 10.1109/vetecf.2011.6093065.

[42] Wang Yifeng, “The design of smart home system based on wireless sensor network,” presented at the 2013 IEEE 4th International Conference on Electronics Information and Emergency Communication (ICEIEC), Nov. 2013, doi: 10.1109/iceiec.2013.6835464.

[43] N. Sghaier et al., “Wireless Sensor Networks for medical care services,” presented at the 2011 7th International Wireless Communications and Mobile Computing Conference (IWCMC 2011), Jul. 2011, doi: 10.1109/iwcmc.2011.5982596.

[44] Z. Moghaddam, I. Ahmad, D. Habibi, and Q. V. Phung, “Smart Charging Strategy for Electric Vehicle Charging Stations,” IEEE Trans. Transp. Electrific., vol. 4, no. 1, pp. 76–88, Mar. 2018, doi: 10.1109/tte.2017.2753403.

[45] “Inductive battery charging, side (with explaining text).” Volvo Cars, May 19, 2011. [online] Available at: <https://www.media.volvocars.com/uk/en-gb/media/photos/38141> [Accessed 6 November 2020].

[46] J. Landt, “The history of RFID,” IEEE Potentials, vol. 24, no. 4, pp. 8–11, Oct. 2005, doi: 10.1109/mp.2005.1549751.

[47] H. Dai, Y. Lu, M.-K. Law, Sai-Weng Sin, U. Seng-Pan, and R. P. Martins, “A review and design of the on-chip rectifiers for RF energy harvesting,” presented at the 2015 IEEE International Wireless Symposium (IWS), Mar. 2015, doi: 10.1109/ieee-iws.2015.7164642.

[48] L.-G. Tran, H.-K. Cha, and W.-T. Park, “RF power harvesting: a review on designing methodologies and applications,” Micro and Nano Syst Lett, vol. 5, no. 1, Feb. 2017, doi: 10.1186/s40486-017-0051-0.

[49] D. Karolak. “Système de radiocommunication télé-alimenté par voie radiofréquence à 2.45 GHz." Université de Bordeaux, 2015. hal: 01668407.

[50] J. Olsson, H. Norde, and U. Magnusson, “Investigation of the current-voltage behavior of a combined Schottky-p-n diode,” Solid-State Electronics, vol. 35, no. 9, pp. 1229–1231, Sep. 1992, doi: 10.1016/0038-1101(92)90154-5.

[51] C.-T. Shah. “Fundamentals of Solid-State Electronics.” World Scientific Publishing Co. Pte. Ltd, 1991. pp. 430.

[52] “HSMS-285x Series Surface Mount Microwave Schottky Detector Diodes”. Avago. 2006. [online] Available at: <https://docs.broadcom.com/doc/AV02-1377EN> [Accessed 7 November 2020].

[53] “Best Research-Cell Efficiency Chart.” NREL. 2020. [online] Available at: <https://www.nrel.gov/pv/cell-efficiency.html> [Accessed 13 November 2020].

[54] “Recommended Light Levels.” NOAO. Available at: <https://www.noao.edu/education/QLTkit/ACTIVITY_Documents/Safety/LightLevels_outdoor+indoor.pdf> [Accessed 7 November 2020].

[55] P. Valicek, T. Novak, J. Vanus, K. Sokansky, and R. Martinek, “Measurement of illuminance of interior lighting system automatically dimmed to the constant level depending on daylight,” presented at the 2016 IEEE 16th International Conference on Environment and Electrical Engineering (EEEIC), Jun. 2016, doi: 10.1109/eeeic.2016.7555604.

[56] P. Michael, “A Conversion Guide: Solar Irradiance and Lux Illuminance.” IEEE DataPort, Sep. 20, 2019, doi: 10.21227/MXR7-P365.

[57] V. Smil. “Our Best Lamps Still Can’t Equal the Luminosity of the Sun.”. IEEE Spectrum Magazine. 27 March 2020. [online] Available at: <https://spectrum.ieee.org/energy/environment/our-best-lamps-still-cant-equal-the-luminosity-of-the-sun> [Accessed 18 November 2020].

[58] T. W. Murphy Jr., “Maximum spectral luminous efficacy of white light,” Journal of Applied Physics, vol. 111, no. 10, p. 104909, May 2012, doi: 10.1063/1.4721897.

[59] P. T. Tolnai and E. Racz, “Preliminary spectral design of a LED- and light bulb-based sun spectrum simulator,” presented at the 2019 IEEE 17th World Symposium on Applied Machine Intelligence and Informatics (SAMI), Jan. 2019, doi: 10.1109/sami.2019.8782735.

[60] Wilson, Benjamin E. “Nanostructured Materials for Advanced Electrochemical Energy Storage Applications.” (2016).

[61] F. Vellucci, V. Sglavo, G. Pede, E. Pasca, V. Malvaldi, and S. Scalari, “Life cycles test on a lithium battery system,” presented at the IECON 2014 - 40th Annual Conference of the IEEE Industrial Electronics Society, Oct. 2014, doi: 10.1109/iecon.2014.7048957.

[62] A. Abdollahi et al., “Battery health degradation and optimal life management,” presented at the 2015 IEEE AUTOTESTCON, Nov. 2015, doi: 10.1109/autest.2015.7356481.

[63] M. Uno and K. Tanaka, “Accelerated Charge–Discharge Cycling Test and Cycle Life Prediction Model for Supercapacitors in Alternative Battery Applications,” IEEE Trans. Ind. Electron., vol. 59, no. 12, pp. 4704–4712, Dec. 2012, doi: 10.1109/tie.2011.2182018.

[64] “Multi-Layer Ceramic Capacitor.” Taiyo Yuden, July 2020. [online]. Available at: <https://ds.yuden.co.jp/TYCOMPAS/or/specSheet?pn=AMK432BJ477MM-T> [Accessed 20 November 2020].

[65] “SCM Series-Connected Super Capacitor Modules.” AVX, June 2020. [online]. Available at: <http://datasheets.avx.com/AVX-SCM.pdf> [Accessed 20 November 2020].

[66] S. Trieste et al. “Accurate sizing of supercapacitors storage system considering its capacitance variation.”. European Conference on Power Electronics and Applications - EPE’11. 14th, Aug 2011, Birmingham, United Kingdom. pp.978-90-75815-15-3. hal:00741131.

[67] “bq25570 Nano Power Boost Charger and Buck Converter for Energy Harvester Powered Applications”, Texas Instruments, March 2013, revised December 2018. [online]. Available at: <http://www.ti.com/lit/ds/symlink/bq25570.pdf> [Accessed 20 November 2020].

[68] “bq25504 Ultra Low-Power Boost Converter With Battery Management For Energy Harvester Applications”, Texas Instruments, October 2013, revised November 2019. [online]. Available at: <http://www.ti.com/lit/ds/symlink/bq25504.pdf> [Accessed 20 November 2020].

[69] Y. Ramadash, “bq25505/70 Design Help V1.3,” Texas Instruments, 2013. [online]. Available at: <http://www.ti.com/lit/zip/sluc484> [Accessed 20 November 2020].

[70] “RF Schottky diodes”, Infineon, September 2016. [online]. Available at: <https://www.infineon.com/dgdl/Infineon-RF%20Schottky%20Diodes-PB-v01_01-EN.pdf?fileId=5546d462557e6e890155917b964163fb> [Accessed 21 November 2020].

[71] H. Sakaki, S. Yoshida, K. Nishikawa, and S. Kawasaki, “Analysis of rectifier operation with FSK modulated input signal,” presented at the 2013 IEEE Wireless Power Transfer Conference (WPTC), May 2013, doi: 10.1109/wpt.2013.6556914.

[72] “TS881 Rail-to-rail 0.9 V nanopower comparator”, ST, December 2013. [online]. Available at: <https://www.st.com/resource/en/datasheet/ts881.pdf> [Accessed 22 November 2020].

[73] “PIC16LF1554/1559: 20-Pin Flash, 8-Bit Microcontrollers with XLP Technology”, Microchip, 2016. [online]. Available at: <http://ww1.microchip.com/downloads/en/DeviceDoc/40001761E.pdf> [Accessed 22 November 2020].

[74] "FeRAM MR45V100A", Lapis Semiconductor, September 2017. [online]. Available at: <http://www.lapis-semi.com/en/data/datasheet-file_db/Memory/FEDR45V100A-01.pdf> [Accessed 22 November 2020].

[75] "MS5837-30BA Ultra Small Gel Filled Pressure Sensor," TE Connectivity, Nov. 2015. Available at: <https://www.te.com/commerce/DocumentDelivery/DDEController?Action=srchrtrv&DocNm=MS5837-30BA&DocType=DS&DocLang=English> [Accessed 22 November 2020].

[76] "Si7050/1/3/4/5-A20 I2C Temperature Sensors," Silicon Labs, 2016. Available at: <https://www.silabs.com/documents/public/data-sheets/Si7050-1-3-4-5-A20.pdf> [Accessed 22 November 2020].

[77] "BME280 Combined humidity and pressure sensor". Bosch Sensortec, Sep. 2018. Available at : <https://www.bosch-sensortec.com/media/boschsensortec/downloads/datasheets/bst-bme280-ds002.pdf> [Accessed 22 November 2020].

[78] "Magnetoresistive Sensor ICs, Nanopower Series," Honeywell Sensing, Apr. 2015. Available at : <https://sensing.honeywell.com/honeywell-sensing-nanopower-series-datasheet-50095501-c-en.pdf> [Accessed 22 November 2020].

[79] "Green and Sustainable Cellular Base Stations: An Overview and Future Research Directions," Energies, vol. 10, no. 5, p. 587, Apr. 2017, doi: 10.3390/en10050587.

[80] "SPIRIT1: Low data rate, low power sub-1GHz transceiver", ST Microelectronics, October 2016. [online]. Available at: <https://www.st.com/resource/en/datasheet/spirit1.pdf> [Accessed on 22 November 2020].

[81] H. Medu, "Energy Comparison of Cypress F-RAM and EEPROM," Cypress Semiconductor, October 2017. [online]. Available at: <https://www.cypress.com/file/46746/download> [Accessed on 22 November 2020].

[82] J. Nicot and T. Taris, "Remote RF powering of ambient sensors," presented at the 2016 IEEE International Conference on Electronics, Circuits and Systems (ICECS), Dec. 2016, doi: 10.1109/icecs.2016.7841313.

[83] "TPL5010 Nano-Power System Timer With Watchdog Function," Texas Instruments, Jan. 2015, revised Sep. 2018. Available at: <https://www.ti.com/lit/ds/symlink/tpl5010.pdf> [Accessed 25 November 2020].

[84] K. Niotaki, F. Giuppi, A. Georgiadis, and A. Collado, "Solar/EM energy harvester for autonomous operation of a monitoring sensor platform," Wireless Power Transfer, vol. 1, no. 1, pp. 44–50, Mar. 2014, doi: 10.1017/wpt.2014.6.

[85] J. Bito, R. Bahr, J. G. Hester, S. A. Nauroze, A. Georgiadis, and M. M. Tentzeris, "A Novel Solar and Electromagnetic Energy Harvesting System With a 3-D Printed Package for Energy Efficient Internet-of-Things Wireless Sensors," IEEE Trans. Microwave Theory Techn., vol. 65, no. 5, pp. 1831–1842, May 2017, doi: 10.1109/tmtt.2017.2660487.

[86] A. Collado and A. Georgiadis, "Conformal Hybrid Solar and Electromagnetic (EM) Energy Harvesting Rectenna," IEEE Trans. Circuits Syst. I, vol. 60, no. 8, pp. 2225–2234, Aug. 2013, doi: 10.1109/tcsi.2013.2239154.

[87] A. Georgiadis and A. Collado, “Improving range of passive RFID tags utilizing energy harvesting and high efficiency class-E oscillators,” presented at the 2012 6th European Conference on Antennas and Propagation (EuCAP), Mar. 2012, doi: 10.1109/eucap.2012.6206429.

[88] A. P. Sample, J. Braun, A. Parks, and J. R. Smith, “Photovoltaic enhanced UHF RFID tag antennas for dual purpose energy harvesting,” presented at the 2011 IEEE International Conference on RFID (IEEE RFID 2011), Apr. 2011, doi: 10.1109/rfid.2011.5764615.

[89] R. Usami, T. Komiyama, Y. Chonan, H. Yamaguchi, and K. Kotani, “Photovoltaic-Assisted Self-Vth-Cancellation CMOS RF Rectifier for Wide Power Range Operation,” presented at the 2018 IEEE Asian Solid-State Circuits Conference (A-SSCC), Nov. 2018, doi: 10.1109/asscc.2018.8579349.

[90] R. J. Vyas, B. B. Cook, Y. Kawahara, and M. M. Tentzeris, “E-WEHP: A Batteryless Embedded Sensor-Platform Wirelessly Powered From Ambient Digital-TV Signals,” IEEE Trans. Microwave Theory Techn., vol. 61, no. 6, pp. 2491–2505, Jun. 2013, doi: 10.1109/tmtt.2013.2258168.

[91] J. Bito, J. G. Hester, and M. M. Tentzeris, “A fully autonomous ultra-low power hybrid RF/photovoltaic energy harvesting system with −25 dBm sensitivity,” presented at the 2017 IEEE Wireless Power Transfer Conference (WPTC), May 2017, doi: 10.1109/wpt.2017.7953858.

[92] N. E. Roberts et al., “26.8 A 236nW −56.5dBm-sensitivity bluetooth low-energy wakeup receiver with energy harvesting in 65nm CMOS,” presented at the 2016 IEEE International Solid-State Circuits Conference (ISSCC), Jan. 2016, doi: 10.1109/isscc.2016.7418101.

[93] S. Hemour and K. Wu, “Radio-Frequency Rectifier for Electromagnetic Energy Harvesting: Development Path and Future Outlook,” Proc. IEEE, vol. 102, no. 11, pp. 1667–1691, Nov. 2014, doi: 10.1109/jproc.2014.2358691.

[94] C. H. P. Lorenz et al., “Overcoming the efficiency limitation of low microwave power harvesting with backward tunnel diodes,” presented at the 2015 IEEE MTT-S International Microwave Symposium (IMS2015), May 2015, doi: 10.1109/mwsym.2015.7167070.

[95] “Amorphous Solar Panel, Indoor PV Cells, Indoor Solar Cells”. WSL Solar. [online]. Available at: <https://www.wsl-solar.com/indoor-pv-cell.html> [Accessed 27 November 2020].

[96] T. Paing, E. Falkenstein, R. Zane, and Z. Popovic, “Custom IC for Ultra-low Power RF Energy Harvesting,” presented at the 2009 Twenty-Fourth Annual IEEE Applied Power Electronics Conference and Exposition (APEC), Feb. 2009, doi: 10.1109/apec.2009.4802822.

[97] S. Oh, N. E. Roberts, and D. D. Wentzloff, “A 116nW multi-band wake-up receiver with 31-bit correlator and interference rejection,” presented at the 2013 IEEE Custom Integrated Circuits Conference - CICC 2013, Sep. 2013, doi: 10.1109/cicc.2013.6658500.

[98] A. Molnar, B. Lu, S. Lanzisera, B. W. Cook, and K. S. J. Pister, “An ultra-low power 900 MHz RF transceiver for wireless sensor networks,” presented at the Proceedings of the IEEE 2004 Custom Integrated Circuits Conference, doi: 10.1109/cicc.2004.1358833.

This page intentionally left blank.

Scientific Productions

International Conferences

J. Nicot and T. Taris, “Remote RF Powering of Ambient Sensors,” presented at the 2016 IEEE International Conference on Electronics, Circuits and Systems (ICECS), Dec. 2016, doi: 10.1109/icecs.2016.7841313.

J. Nicot, L. Fadel, and T. Taris, “An RF-Powered IoT Node for Environment Sensoring,” presented at the 2019 IEEE Wireless Power Transfer Conference (WPTC), Jun. 2019, doi: 10.1109/wptc45513.2019.9055528.

International Journals

Waiting on Manuscript acceptance by Cambridge WPT Journal (see https://www.cambridge.org/core/journals/wireless-power-transfer)

This page intentionally left blank.